LA-UR-23-22856

Approved for public release; distribution is unlimited.

Title:	TERRAIN-INFLUENCED WINDS AND FIRE-FIRE INTERACTIONS IN WILDLAND FIRE SIMULATIONS
Author(s):	Robinson, David Joseph
Intended for:	Dissertation
Issued:	2023-04-18 (rev.1)

FLORIDA STATE UNIVERSITY

COLLEGE OF ARTS AND SCIENCES

TERRAIN-INFLUENCED WINDS AND FIRE-FIRE INTERACTIONS IN WILDLAND FIRE SIMULATIONS

By

DAVID ROBINSON

A Dissertation submitted to the
Geophysical Fluid Dynamics Institute
in partial fulfillment of the
requirements for the degree of
Doctor of Philosophy

2023

David Robinson defended this dissertation on April 10, 2023.
The members of the supervisory committee were:

Bryan Quaife
Committee Chair

Fred Huffer
University Representative

Rodman Linn
Committee Member

Kevin Speer
Committee Member

Neda Yaghoobian
Committee Member

The Graduate School has verified and approved the above-named committee members, and certifies that the dissertation has been approved in accordance with university requirements.

To my parents John & Barbara, and my partner Julia.

TABLE OF CONTENTS

List of Tables vi

List of Figures vii

List of Abbreviations xii

Abstract xiii

1 Introduction **1**

1.1 QUIC-URB Overview 1

1.2 QUIC-URB and FIRE-CA Coupling 4

1.2.1 Restrictions on Modified QUIC-URB in Operational Settings 7

1.3 Incorporating Terrain into QUIC-Fire 8

1.4 Modifications to the QUIC-URB SOR Algorithm 9

2 Development of a Terrain Following Wind Solver **12**

2.1 Terrain-Following Model Extension 12

2.2 Computational Method 16

2.3 Askervein Hill 20

2.4 Complex Terrain 24

2.5 Conclusions 26

3 Performance of QUIC-Fire using Terrain-Influenced Winds **28**

3.1 Introduction 28

3.2 QUIC-Fire Overview 29

3.3 Effect of Topography on Winds and Fire Spread 30

3.3.1 Terrain-Influenced Winds 30

3.3.2 Fire-CA Grid for Terrain Effects 31

3.3.3 Buoyant Plume Transport in Complex Terrain 33

3.4 Comparison of FIRETEC and QUIC-Fire on Ideal Terrain Configurations 33

3.4.1 Description of the Simulation Domains 35

3.5 Results and Discussion 38

3.5.1 Fire Spread Rates 38

3.5.2 Fire Spread Rates in Region 1 48

3.5.3 Fire Spread Rates in Region 2 . . . 48
3.5.4 Fire Spread Rates in Region 3 . . . 49
3.5.5 Lateral Fire Spread . . . 52
3.6 Conclusions . . . 54

4 Analysis of Saving Lagrange Multipliers **58**
4.1 Modified SOR Effects on Fire Phenomenology . . . 58
4.1.1 Head Fires . . . 58
4.1.2 Testing Fire-Fire Interaction . . . 59
4.1.3 Ring Fires . . . 63
4.2 Performance of SOR Change . . . 67
4.2.1 Relaxation of Error and Generated Wind Artifacts . . . 67
4.2.2 Investigating Boundary Effects and Convergence . . . 69
4.3 Conclusions . . . 76

5 Future Directions **78**

Bibliography . . . 82

Biographical Sketch . . . 87

LIST OF TABLES

1.1 Weights used in Equation (1.4) to enforce boundary conditions. 4

3.1 Description of the five topographies used in the simulations. Vectors in the images are near surface background winds generated from the terrain-following version of QUIC-URB. 39

3.2 Fire spread rates in selected regions of the computational domain for both FIRETEC and QUIC-Fire. Spread rate differences across Region 1 are characterized by slower rates from QUIC-Fire in the Hill12, Upcan12, and Ridge12 simulations. QUIC-Fire shows under-predicted spread rates across Region 2 and over-predicted rates across Region 3 when comparing with FIRETEC in non-flat cases. 46

3.3 Lateral spread rates measured from the extents of the initial ignition line edges for simulations ran by both FIRETEC and QUIC-Fire. 54

LIST OF FIGURES

1.1 Schematic of the staggered grid that is implemented in QUIC-URB [33]. This helps illustrate that the Euler-Lagrange equations (Equation 1.5) are centered on the cell faces. These velocities are then averaged across the cell to give cell centered velocities to be used in the FIRE-CA algorithm to evolve the fire. 3

1.2 Isosurfaces of the vertical velocities generated by the modified QUIC-URB plume model. The plume pictured is generated with a heat source of 1,000 kW located at ground level and a background wind of 3 m/s in the y-direction. 6

1.3 Schematic illustrating the indraft generated from a buoyant plume and the pulling effect it has on surrounding fires [37] 6

1.4 Wind fields of $\widetilde{u}$ and $\widetilde{v}$ velocities showing the indrafts generated from a single plume and 1,000 SOR iterations. There is no background wind in this case and the plume is generated with a 1,000 kW heat source located at (160 m, 160 m, 0 m). This is canonical fire phenomenology that is illustrated in Figure 1.3. 7

1.5 Schematics of some prescribed fire strategies and their orientations given the background wind [30]. The numbers shown are the order that each section is ignited. . . 8

2.1 An example of a terrain-following grid produced by transforming sigma coordinates back to Cartesian space. 13

2.2 A diagram of the sigma coordinate grid showing locations of cell-centered λ values and face-centered contravariant velocities. When calculating the adjustments to the initial velocities, partial derivatives are taken across and along the corresponding cell faces. 18

2.3 A zoomed in portion of the 6 km $\times$ 6 km Askervein Hill domain used for the simulation. The image encapsulates approximately a 4 km $\times$ 4 km section of the domain. The transects are labeled by name with sensor locations being represented by vertical gray cylinders. 20

2.4 A vector plot zoomed in over the larger hill of the Askervein domain. Locations of transect sensors are shown as gray circles, sensor measurement vectors are colored green, and 20% of the surface winds from the QUIC-URB simulation results are colored blue. For visibility all vectors are scaled by a factor of 12. 21

2.5 A comparison of the measured winds and the results from the terrain-following implementation of QUIC-URB over Askervein Hill along transects A and AA. These graphs show the distance along transect (distance of zero corresponds to the hilltop) vs. the relative speed-up from the reference upwind velocity. Transects A and AA are oriented roughly parallel to the recorded background wind direction meaning positive values on the transect are located on the leeward side of the hill. 22

2.6 A comparison of the measured winds and the results from the terrain-following implementation of QUIC-URB over Askervein Hill along transect B. The graph plots the distance along transect (distance of zero corresponds to the hilltop) vs. the relative speed-up from the reference upwind velocity. Transect B is oriented roughly perpendicular to the recorded background wind direction. 23

2.7 A comparison of the wind directions between sensor measurements and model results. The plots show the distance along the transect (distance of zero corresponds to the hilltop) vs. windward direction at the sensor location. Positive values on the transect are on the leeward side of the hill 23

2.8 The topography of a 6.7 km $\times$ 7.0 km section of the terrain surrounding the sensors of the EMRTC field experiment in the Socorro Mountains. Nine of the 18 sensors are labeled at their locations. Note that the L1 sensor, used for the background wind profile of the simulations, is located at the top of a plateau that is isolated from the steep surrounding terrain. 24

2.9 The topography at 11 m resolution of the 2.25 km $\times$ 2.25 km section of terrain used for the terrain-following QUIC-URB simulations. 25

2.10 Vector plots comparing measurements and simulations of the terrain-following implementation of QUIC-URB applied to winds in the Soccorro mountains at 12:30 PM and 7:40 PM local time. The background wind at 10 m and the scale for the model-computed blue vectors are illustrated in the grey inset. The red vectors represent sensor measurements, labeled by sensor number, and the green vectors are model results interpolated to the sensor locations. Both the red and green vectors are scaled up by a factor of three to make the comparison easier. 26

3.1 Diagram showing how the fuel grid, green lines, and QUIC-Fire grids, blue lines, align with each other. The vertical extent of each grid is denoted with a solid line and the lower cell tops denoted with dashed lines. The vertical resolution of the draped fuel grid stays constant whereas the terrain-following grid of the wind grid is compressed in the presence of terrain. The dashed black lines in the expanded window demonstrate the horizontal discretization that both grids typically share. 31

3.2 Schematic of the wind vector decomposition carried out for surface fuel cells. 32

3.3 Vertical contours of vertical velocities in FIRETEC and QUIC-Fire to compare buoyant plume trajectories with and without terrain. Plots (a) and (d) show FIRETEC simulations on flat terrain to show the impact of terrain (plots are scaled to match the other plots). As one can see in the center (FIRETEC) and the right (QUIC-Fire), the buoyant plumes, here identified with the updrafts, are bent upward by the hill. QUIC-Fire results underestimate the upward boundary of the plume, but capture the intensity of the updraft at the ground, where most of the fire activity is. The simulations use a constant heat source of 2000 kWm^{-1} across a single cell to generate the buoyant plumes. All lengths are in meters in the plots. 34

3.4 Top view of the computational domain showing domain extents, fuels, fireline position, and ambient wind direction for the simulations. 36

3.5 Snapshots of fire simulation states from FIRETEC (left) and QUIC-Fire (right). The top row (a) shows results from the Hill6 case and the bottom row (b) shows results from the Canyon6 case 150s after ignition. The FIRETEC snapshots are taken from [21]. Red isosurfaces in the left images indicate hot gases and red/orange in the right images are accumulated EPs in fuel cells that are landing in open air and generate buoyant updrafts. Dark, medium, and light green colors indicate locations of canopy fuel, tall grass, and depleted fuel in the left images whereas green, yellow and black indicate the same in the right images. White vectors represent winds near the top of the canopy fuel. 40

3.6 The same as Figure 3.5 but for the Upcan6 (top row (a)) and Ridge6 (bottom row (b)) cases. Results are shown at 150 s after ignition. 41

3.7 The same as Figure 3.5 but for the Hill12 (top row (a)) and Canyon12 (bottom row (b)) cases. Results are shown at 100 s after ignition. 42

3.8 The same as Figure 3.5 but for the Upcan12 (top row (a)) and Ridge12 (bottom row (b)) cases. Results are shown at 100 s after ignition. 43

3.9 The same as Figure 3.5 but for the Flat6 (top row (a)) at 150 s after ignition and the Flat12 (bottom row (b)) case at 100 s after ignition. 44

3.10 A comparison of fire propagation distances between FIRETEC (top, from [21]) and QUIC-Fire (bottom). 45

3.11 Distributions of downwind fire spread rates against centerline elevation (top) and centerline slope (bottom) for the 6 ms^{-1} (left) and 12 ms^{-1} (right) non-flat simulations. Pearson correlation r and p values are calculated and displayed in each corresponding plot. Correlation results show a strong positive correlation between rate of spread and elevation and a weak negative correlation between rate of spread and slope. 50

3.12 The fire lateral spread of FIRETEC and QUIC-Fire. The top two figures are taken from [21] and the figures below are generated using results from QUIC-Fire. Points on the FIRETEC plots are equispaced along the y-axis, i.e. points are only plotted if propagation distance is above a threshold, whereas points on the QUIC-Fire plots are equispaced in time. 51

3.13 Snapshots of fire simulation states of QUIC-Fire simulations showing near-surface wind-vectors for the (a) Hill12, (b) Canyon12, (c) Ridge12, (d) Upcan12, and (e) Flat12 cases. Camera positions are roughly in the same position for (a), (b), (c), and (d) above the Region 2 section and the camera position for (e) is slightly downwind to show wind vectors nearer to the head of the fire. These figures show the 2 m resolution winds in their entirety. Quivers are scaled to 45% of their actual length. 55

4.1 Snapshots of two simulations showing the development of a head fire for both versions of the SOR algorithm. The top row shows results from the original SOR algorithm and the bottom row shows results from the modified version. 59

4.2 Initial conditions of fire simulations described in Section 4.1.2 used for investigating differences in fire behavior driven by the different initial guesses of λ. 60

4.3 Snapshots of fuel density from test case (a) in Figure 4.4 at 150 seconds and 300 seconds into the simulations. The left column is the original algorithm and the right column is using the modified SOR algorithm. 61

4.4 Results for test case (b) with initial configuration shown in Figure . The top row shows of snapshots of fuel density from the original SOR algorithm and the bottom row showing snapshots from the modified version. It is important to notice that the third column are snapshots at different times showing the transition to a 'jump' fire occurs at different times. 62

4.5 Snapshots of fuel density from test case (c). The top row shows results from the original SOR version and the bottom row showing results from the modified version. 63

4.6 Snapshots of fuel density from test case (d). The top row shows results from the original algorithm and the bottom row shows results from the modified SOR algorithm. 63

4.7 Initial conditions for three different ring fire tests. The diameters for the rings are 100, 200, and 400 meters for (a), (b), and (c) respectively. The ignition spots in (a) and (b) are spaced 20 meters apart with a diameter of 4 meters. The ignition spots in ring (c) are spaced 45 meters apart and have a diameter of 6 meters. Notice the domain for (c) is 50 percent larger than (a) and (b). All ring fire simulations have a background wind speed of 0 ms^{-1}. 64

4.8 Snapshots of simulations using the initial conditions in Figure 4.7 ran with wind fields generated by the original SOR routine. The snapshots are oriented columnwise in order of (a), (b), and (c). Almost no fire acceleration is seen except for in the small ring fire, case (a), in the $t = 100s$ and $t = 200s$ snapshots. 65

4.9 Snapshots of simulations using the initial conditions in Figure 4.7 ran with wind fields generated by the modified SOR routine. For comparison the time of the snapshots are the same as those in Figure 4.8 and are oriented in the same columnwise manner. 66

4.10 Error isosurfaces from the simulation described in the beginning of Section 4.2.1. The blue surface is an isosurface of the plume model generated winds, showing the structure of the plumes. The orange, yellow, light green, and dark green surfaces are isosurfaces for wind speed error thresholds of 1E-1, 1E-2, 1E-3, and 1E-4 respectively. The snapshots (a)-(d) are taken 25, 80, 125, and 150 seconds into the simulation. The decay of the wind field generated from the first plume is evident by the similarity in the error surfaces between (a) and (d). 68

4.11 Snapshots of the second simulation described in Section 4.2.1 showing error isosurfaces. The blue surfaces are isosurfaces of the plume model generated vertical winds, showing the structure of the plumes. The opaque colored surfaces are isosurfaces for wind speed error thresholds calculated from the 1,000 iteration solution at each time step. Snapshot (c) shows the transition of shutting off the initial line of heat sources to the two heat sources at the points of the 'X' being turned on. 71

4.12 Isosurfaces of the vertical velocities generated by the modified QUIC-URB plume model. The plume pictured is generated with a heat source of 1,000 kW located at ground level and a background wind of 3 ms^{-1} in the y-direction. This is the simulation used to generate the error plots in Figure 4.14. 72

4.13 Graphs of the L_1 and L_{inf} errors for the single plume with no wind case. 73

4.14 Graphs of the L_1 and L_{inf} errors for the single plume with $v_0 = 3$ ms^{-1}. The top row plots are errors calculated using the entire domain defined by σ and the bottom row shows errors that are calculated using the bottom 14.0 meters of the domain (bottom 10 cells). 74

4.15 Shown are the initial ignition patterns for the tests described in Section 4.2.2. The spot fire ignition pattern uses a custom ignition pattern routine that is unable to produce the same initial ignition plot as the left side. Due to this the fuel density at 5 seconds into the simulation is shown to show the initial ignition pattern. 75

4.16 Graphs of the L_1 and L_{inf} errors for the head fire and spot fire tests with a background wind speed of 3ms^{-1}. The errors are calculated using the entire domain defined by σ with the top row showing errors from the head fire case and the bottom row showing results from the spot fires case. 76

5.1 Diagram from [33] showing how QUIC-URB determines whether street canyon parameterizations or isolated flow parameterizations should be injected around a building. 79

5.2 Diagram from [33] showing the wind field resulting from enforcing mass conservation after flow parameterizations have been injected into the background wind field. . . . 79

5.3 Diagram from [33] showing how different flow parameterizations are used together to generate complex flows around four buildings as seen from the top (a) and side (b). . 80

LIST OF ABBREVIATIONS

CFD	Computational Fluid Dynamics
EP	Energy Packet
LES	Large Eddy Simulation
SOR	Successive Over-Relaxation
TF	Terrain-following
WFDS	Wildland-Urban Interface Fire Dynamics Simulator

ABSTRACT

Ensemble-based approaches to prescribed fire planning cannot be supported by computational fluid dynamics based models like FIRETEC and the Wildland-Urban Interface Fire Dynamics Simulator (WFDS) because they are too computationally expensive and cannot leverage large eddy simulation approaches like CAWFE and WRF-SFIRE because they have too coarse of resolution. QUIC-Fire was developed to fill this gap but it cannot currently address complex terrain, that is typical for instance in the Western United States. This dissertation describes a variety of improvements made to QUIC-Fire and its various incorporated algorithms in an effort to make it a viable tool in simulating wildland and prescribed fires on terrain. The modifications made to QUIC-Fire are described in three chapters. The first chapter describes the extension of the diagnostic wind model QUIC-URB, the wind engine of QUIC-Fire, to a terrain-following coordinate system. The terrain-influenced winds it generates are analyzed and compared. In particular, this chapter presents the mathematical derivation of the wind solver leading to a linear system of equations that are solved through the successive over-relaxation method. The model is validated against a standard test used in previous works (the Askervein Hill) and against a new dataset from measurements in the Socorro Mountains, New Mexico. The terrain-following implementation captures the correct phenomenology for the isolated Askervein Hill, with a wind speed up at the top of the hill. The model agrees well with measurements on the upwind side of the peak, but overestimates speed-up on the downwind side of the hill. This is due to the inability of the model to generate flow separation and wake-eddy dynamics. On a common laptop, the divergence-free wind field is obtained in 6 s, making the solver appealing for coupled fire-atmosphere simulations. The Socorro Mountain is highly complex, with many cliff faces, peaks, and valleys. Although the model captures the magnitude and direction of inlet and outlet areas of the domain, it performs rather poorly in the valley region and in the regions near the steep cliffs. Hence, the model shows good agreement with data in areas of open sloped terrain but lacks in areas where flow separation and thermally driven effects may be present (neither effect is addressed in this work). In the second chapter the implementation of the terrain-following version of QUIC-URB into QUIC-Fire, and the necessary changes needed to include terrain are described. No changes to the underlying fire spread algorithm are made other than what is required to correctly account for the inclusion of terrain. Previously published FIRETEC results that use five different topographies that share the same centerline profile are

compared to simulation results from the modified QUIC-Fire that use the same topographies and fuels. QUIC-Fire results show overall similar behaviors in terms of how the topographies affect fire shapes and trends in spread rates. Due to the terrain-following version of QUIC-URB being unable to generate flow separations at the crest of hills, fire spread rates in these regions across all topographies are over-predicted when compared to FIRETEC. Lateral fire growth shows similar trends with FIRETEC between topographies but does not capture the increase in spread due to a diagonal interface between grassland and forested fuel region of the domain. These results suggest that there are three algorithms within QUIC-Fire that could use improvement: how flame tilt angle is accounted for, the incorporation of non-local drag effects, and the inclusion of the wake-eddy parameterizations that are used in QUIC-URB. Lastly, the third chapter describes a modification to the initial guess used for the calculation of the QUIC-URB mass-conserved wind solution during fire simulations. The modification is aimed at improving fire-fire interactions in QUIC-Fire simulations. The modification consists of using the solution from the previous timestep as the starting point for the calculation of the solution for the next timestep. Fire-fire interactions is greatly improved by the change but a new source of error is introduced. Due to how plumes are modelled in QUIC-Fire the new solution contains errors where gaps in the plume structure are present. However, these errors are mostly limited to the upper atmosphere, where they do not affect fire behavior at the surface, and their magnitude isn't significant enough to discount the amount of new fire phenomenology now captured in QUIC-Fire with the change.

CHAPTER 1

INTRODUCTION

QUIC-Fire is a wildland fire simulation tool designed to capture fire-atmosphere interactions which are necessary to accurately capture fire behavior in prescribed fire scenarios. QUIC-Fire achieves this coupling by linking together two solvers; QUIC-URB and FIRE-CA. QUIC-URB is a fast response 3D wind field solver that uses mass conservation constraints and empirical parameterizations to compute flow fields around buildings in urban settings [33]. FIRE-CA is a cellular automata (CA) based fire spread model that calculates heat release and fuel consumption over 3D vegetation. Heat release distributions and the evolving 3D vegetation structure is fed into the modified QUIC-URB model where the fire-influenced wind field and turbulence intensity are calculated and then fed into FIRE-CA. The combination of QUIC-URB and FIRE-CA creates the fire-atmosphere coupling in QUIC-Fire and the minimal computational cost and significant speed of these algorithms means QUIC-Fire is a fire simulation tool useful when users are limited to smaller computing resources. However, QUIC-URB was not designed for incorporate the effects of terrain into its wind field. Therefore, early versions of QUIC-Fire only simulated fires on flat terrain. QUIC-Fire has had successes with simulating fire on flat terrain so the natural progression is to incorporate terrain into the algorithm, greatly expanding the number of domains where QUIC-Fire is suitable. This dissertation work expands QUIC-Fire to incorporate terrain in both the generation of wind fields and the fire spread algorithm. Furthermore, by improving the initial guess to the solution for generating the wind field the interaction between separate bodies of fire is greatly improved.

1.1 QUIC-URB Overview

QUIC-URB is a diagnostic wind model that produces mass-consistent wind fields from multiple, heterogeneous wind measurements over domains with sizes ranging from 1 km to 100 km at horizontal resolutions typically varying from 1 m to 200 m [45]. QUIC-URB uses a Cartesian coordinate system based on Universal Transverse Mercator coordinates in which $\widetilde{x}$ and $\widetilde{y}$ are perpendicular and define the horizontal plane, while $\widetilde{z}$ is vertical and positive in the direction opposite to gravity. The QUIC-URB cells are rectangular prisms, although usually the cell size in the $\widetilde{x}$

and $\widetilde{y}$ directions are the same. In the $\widetilde{z}$ direction, a stretched grid with smaller cells close to the ground is usually employed to capture the wind speed gradients at the surface while avoiding an unnecessary computational burden at higher heights, where the wind speed does not change as much.

The original QUIC-URB formulation [42] aims to minimize the integral:

$$E(\widetilde{u},\widetilde{v},\widetilde{w},\lambda) = \int_V \left[\alpha_1^2\left(\widetilde{u}-\widetilde{u}_0\right)^2 + \alpha_1^2\left(\widetilde{v}-\widetilde{v}_0\right)^2 + \alpha_2^2\left(\widetilde{w}-\widetilde{w}_0\right)^2 + \lambda\left(\frac{\partial\widetilde{u}}{\partial\widetilde{x}} + \frac{\partial\widetilde{v}}{\partial\widetilde{y}} + \frac{\partial\widetilde{w}}{\partial\widetilde{z}}\right)\right] d\mathbf{x}, \tag{1.1}$$

where $\widetilde{u}_0$, $\widetilde{v}_0$, and $\widetilde{w}_0$ are the interpolated initial wind components in the $\widetilde{x}$, $\widetilde{y}$, and $\widetilde{z}$ directions, respectively; $\widetilde{u}$, $\widetilde{v}$, and $\widetilde{w}$ are the Cartesian adjusted velocities defining a mass-consistent flow field; α_1 and α_2 are the Gaussian precision moduli; and λ is a Lagrange multiplier. The precision moduli define how much of the wind adjustment should be directed to changing $\widetilde{u}$ and $\widetilde{v}$ vs. $\widetilde{w}$. Hence, if $\alpha_1/\alpha_2 > 1$, then $\widetilde{w}$ will change more than $\widetilde{u}$ and $\widetilde{v}$. In the original QUIC-URB formulation $\alpha_1 = \alpha_2$ since prescribed wake eddies around buildings involve modifying $\widetilde{u}$, $\widetilde{v}$, and $\widetilde{w}$ velocities. In practice, (1.1) expresses the concept that the desired adjusted wind field is mass-consistent (second term) while keeping the adjustments as small as possible.

The minimum of equation (1.1) is found by solving the Euler-Lagrange equations:

$$\nabla^2\lambda = -2\alpha_1^2\nabla\cdot\widetilde{\mathbf{u}}_0, \tag{1.2a}$$

$$\widetilde{u} = \widetilde{u}_0 + \frac{1}{2\alpha_1^2}\frac{\partial\lambda}{\partial\widetilde{x}}, \tag{1.2b}$$

$$\widetilde{v} = \widetilde{v}_0 + \frac{1}{2\alpha_1^2}\frac{\partial\lambda}{\partial\widetilde{y}}, \tag{1.2c}$$

$$\widetilde{w} = \widetilde{w}_0 + \frac{1}{2\alpha_2^2}\frac{\partial\lambda}{\partial\widetilde{z}}. \tag{1.2d}$$

Equations (1.2) is a system of partial differential equations for λ, $\widetilde{u}$, $\widetilde{v}$, and $\widetilde{w}$, and $\widetilde{\mathbf{u}}_0 = (\widetilde{u}_0, \widetilde{v}_0, \widetilde{w}_0)$. In QUIC-URB, a finite-difference method is used to solve equation (1.2) with first-order central differences. After discretizing, the result is a linear system that QUIC-URB solves with the successive over-relaxation (SOR) method. QUIC-URB uses the staggered grid shown in Figure 1.1 and the prescribed wind velocity as the 'observed' wind field at the cell faces. The algorithm then modifies this windfield through the SOR routine to arrive at the analyzed windfield $(\widetilde{u},\widetilde{v},\widetilde{w})$. The algorithm aims to minimize the variance of the difference between the observed windfield and analyzed wind field [41].

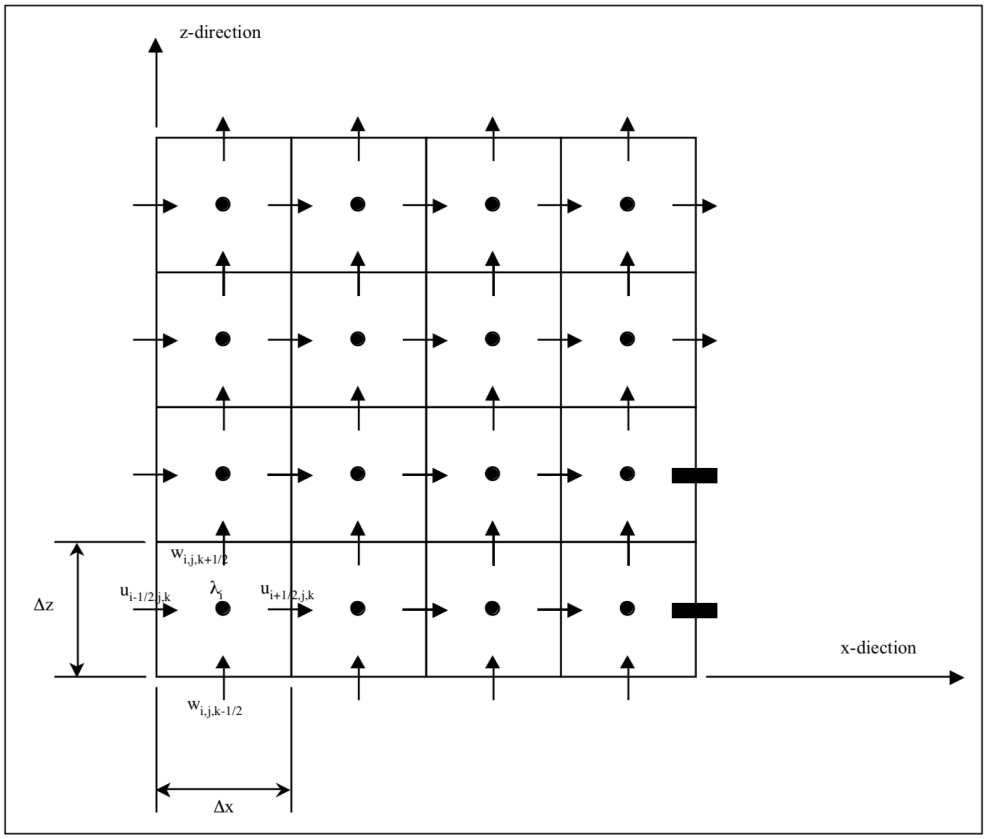

Figure 1.1: Schematic of the staggered grid that is implemented in QUIC-URB [33]. This helps illustrate that the Euler-Lagrange equations (Equation 1.5) are centered on the cell faces. These velocities are then averaged across the cell to give cell centered velocities to be used in the FIRE-CA algorithm to evolve the fire.

To minimize Equation 1.1 the code solves

$$\frac{\partial^2 \lambda}{\partial x^2} + \frac{\partial^2 \lambda}{\partial y^2} + \left(\frac{\alpha_1}{\alpha_2}\right)^2 \frac{\partial^2 \lambda}{\partial z^2} = R \tag{1.3}$$

for λ where R is a term that includes the divergence of the initial velocity field. With missing subscripts defaulting to i, j, and k, $R_{i,j,k}$ is discretized as

$$R_{i,j,k} = -2\alpha_1^2 \left(\frac{\partial \widetilde{u}_0}{\partial x} + \frac{\partial \widetilde{v}_0}{\partial y} + \frac{\partial \widetilde{w}_0}{\partial z}\right) \approx -2\alpha_1^2 \left(\frac{\widetilde{u}^0_{i+\frac{1}{2}} - \widetilde{u}^0_{i-\frac{1}{2}}}{\Delta x} + \frac{\widetilde{v}^0_{j+\frac{1}{2}} - \widetilde{v}^0_{j-\frac{1}{2}}}{\Delta y} + \frac{\widetilde{w}^0_{k+\frac{1}{2}} - \widetilde{w}^0_{k-\frac{1}{2}}}{\Delta z}\right).$$

Applying a second-order centered difference stencil to Equation (1.3) results in the discretization:

$$\frac{\lambda_{i+1} - 2\lambda + \lambda_{i-1}}{\Delta x^2} + \frac{\lambda_{j+1} - 2\lambda + \lambda_{j-1}}{\Delta y^2} + \left(\frac{\alpha_1}{\alpha_2}\right)^2 \frac{\lambda_{k+1} - 2\lambda + \lambda_{k-1}}{\Delta z^2} = R_{i,j,k}$$

where, for brevity, only shifts in indices are listed in subscripts (i.e. $\lambda_{i+1} = \lambda_{i+1,j,k}$).

Table 1.1: Weights used in Equation (1.4) to enforce boundary conditions.

Cell Type	e	f	g	h	m	n	o	p	q
Wall Below	1	1	1	1	1	0	1	1	0.5
Wall Above	1	1	1	1	0	1	1	1	0.5
Wall to Right	0	1	1	1	1	1	0.5	1	1
Wall to Left	1	0	1	1	1	1	0.5	1	1
Wall Behind	1	1	0	1	1	1	1	0.5	1
Wall in Front	1	1	1	0	1	1	1	0.5	1
Below & in Front	1	1	0	1	1	0	1	0.5	0.5
Below & to Left	1	0	1	1	1	0	0.5	1	0.5
Below & to Right	0	1	1	1	1	0	0.5	1	0.5
Below & Behind	1	1	1	0	1	0	1	0.5	0.5

The velocity field is on a staggered grid and the Lagrange multipliers are cell-centered as seen in Figure 1.1. Substituting the discretizations into Equation (1.3) and solving for $\lambda_{i,j,k}$ we arrive at

$$\lambda_{i,j,k} = \frac{-\left(\Delta x^2 R_{i,j,k}\right) + \left(e\lambda_{i+1} + f\lambda_{i-1} + A\left(g\lambda_{j+1} + h\lambda_{j-1}\right) + B\left(m\lambda_{k+1} + n\lambda_{k-1}\right)\right)}{2\left(o + Ap + Bq\right)}$$

where $A = \frac{\Delta x^2}{\Delta y^2}$, $B = \eta\frac{\Delta x^2}{\Delta z^2}$, and $\eta = \left(\frac{\alpha_1}{\alpha_2}\right)^2$. Lowercase letter coefficients are for enforcing boundary conditions and can be referenced in Table 1.1. This equation can be put into SOR form:

$$\lambda_{i,j,k}^{\mu+1} = \omega\left[\frac{-\left(\Delta x^2 R_{i,j,k}\right) + \left(e\lambda_{i+1}^{\mu} + f\lambda_{i-1}^{\mu} + A\left(g\lambda_{j+1}^{\mu} + h\lambda_{j-1}^{\mu}\right) + B\left(m\lambda_{k+1}^{\mu} + n\lambda_{k-1}^{\mu}\right)\right)}{2\left(o + Ap + Bq\right)}\right] + \left(1-\omega\right)\lambda_{i,j,k}^{\mu} \quad (1.4)$$

where μ is the current iteration step and the SOR acceleration parameter used is $\omega = 1.78$ which was chosen based on recommendations from [35]. The Lagrange multipliers are initialized to zero and once sufficient iterations are executed, achieving convergence, the analyzed velocity field is calculated using partial derivatives of λ in Equations (1.5),

$$\widetilde{u} = \widetilde{u}_0 + \frac{1}{2\alpha_1^2}\frac{\partial\lambda}{\partial\widetilde{x}}, \qquad \widetilde{v} = \widetilde{v}_0 + \frac{1}{2\alpha_1^2}\frac{\partial\lambda}{\partial\widetilde{y}}, \qquad \widetilde{w} = \widetilde{w}_0 + \frac{1}{2\alpha_2^2}\frac{\partial\lambda}{\partial\widetilde{z}}. \quad (1.5)$$

1.2 QUIC-URB and FIRE-CA Coupling

The QUIC-Fire code combines the QUIC-URB mass-conserving wind model with the fire spread model FIRE-CA to produce a fire-wind coupled fire spread model. The QUIC-URB model uses

a user-specified wind background profile that follows either a power-law, a log-law, or a set of measurements at multiple heights to generate an initial background wind field, $(\widetilde{u}_0, \widetilde{v}_0, \widetilde{w}_0)$. In the QUIC-Fire code this background wind is modified by including aerodynamic drag effects based on the 3D fuel field supplied by the user. As combustion occurs and fuel is consumed the fuel drag effect is reduced as fuel mass is reduced. The wind strength of a cell approaches the initial background wind strength as the fuel of a cell is reduced to zero.

The combustion of fuel also produces energy release that drives two processes captured in the code: the evaporation of moisture in fuels and the generation of buoyant updrafts. The buoyancy-driven flows are modeled by defining plume trajectories parameterized with Briggs theory [13] wherever energy is released into the atmosphere. Each time step these hot air plumes travel upward, advect with background wind, and expand as they mix with cooler air. The structure of a single plume with a background wind is shown in Figure 1.2. These plumes inject vertical velocities into the wind field modifying the background $\widetilde{w}_0$ field. These vertical velocities generate the initial divergence in the wind field which leads to indrafts when the mass-conservation is enforced with the SOR solver, driving the divergence to zero. The Gaussian precision moduli (α_1 and α_2) weight trusted observations, limiting the change from their original values. In other words, an initial value in the wind field that we desire to be conserved should have a greater α value assigned with respect to other winds in the field. In QUIC-Fire the only prescribed/observed values are the vertical velocities from the buoyant plumes. To preserve the strength of the plumes it is suggested in [27] that $\alpha_1 = 1$ everywhere, $\alpha_2 = 10$ wherever a plume is present, and $\alpha_2 = 1$ everywhere else. These values of α_1 and α_2 preserve the vertical velocity structure generated through the plume model while also allowing the horizontal velocities to adjust; this is made obvious from Equations (1.5). The resulting effect of conserving the strength of the buoyant-updrafts and the scheme aiming to satisfy mass conservation with the analyzed wind field is that indrafts are generated in the horizontal directions. These induced indrafts (Figure 1.4) satisfy the conservation of mass constraint and are canonical fire phenomenology observed in prescribed fires (Figure 1.3) [37, 30, 3].

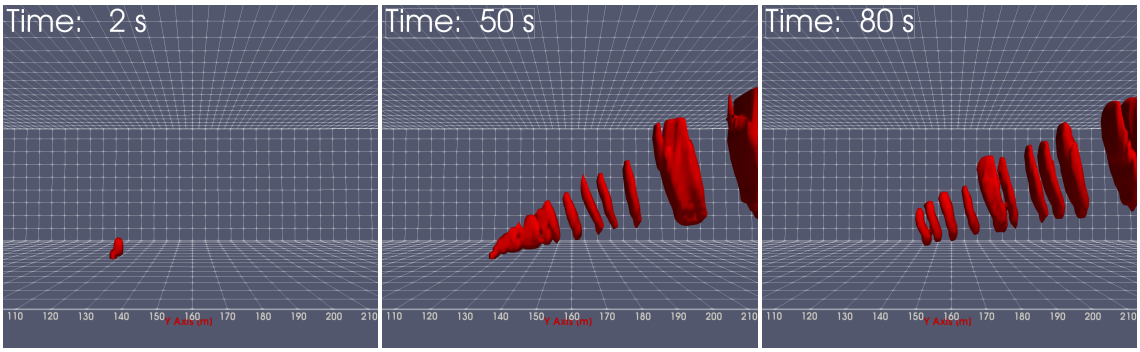

Figure 1.2: Isosurfaces of the vertical velocities generated by the modified QUIC-URB plume model. The plume pictured is generated with a heat source of 1,000 kW located at ground level and a background wind of 3 m/s in the y-direction.

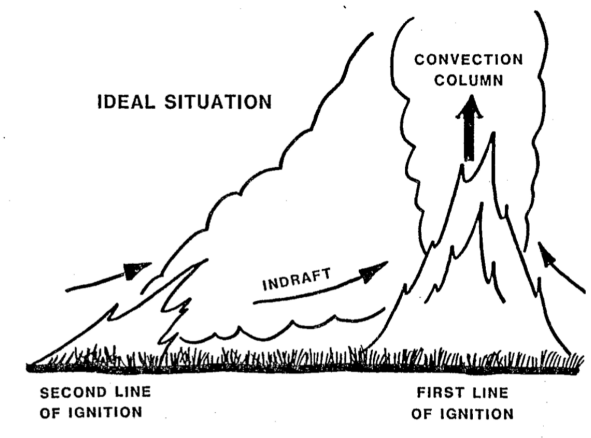

Figure 1.3: Schematic illustrating the indraft generated from a buoyant plume and the pulling effect it has on surrounding fires [37] .

A single time step for QUIC-Fire consists of:

1. The modified QUIC-URB model generates new buoyant plumes based on heat intensity from combusting cells and evolves any already existing buoyant plumes. This step creates the 'observed' background wind field, $(\widetilde{u}_0, \widetilde{v}_0, \widetilde{w}_0)$, on a staggered grid (Figure 1.1).

2. The QUIC-URB SOR routine takes the observed wind field and generates an 'analyzed' wind field. This analyzed wind field is produced by doing SOR iterations on the observed wind field that adjust the wind to satisfy conservation of mass while preserving the plume structures generated from the first step. This analyzed wind field is averaged across cells to generate cell-centered wind values.

3. Cell-centered wind values are then used by the FIRE-CA model to update the evolution of the fire. New ignitions and heat intensities are calculated which will be used by the modified QUIC-URB routine to determine the updated wind field.

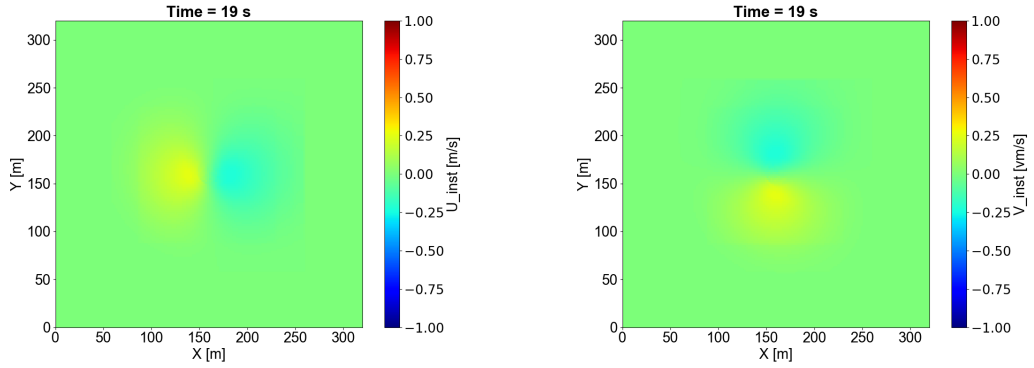

Figure 1.4: Wind fields of $\widetilde{u}$ and $\widetilde{v}$ velocities showing the indrafts generated from a single plume and 1,000 SOR iterations. There is no background wind in this case and the plume is generated with a 1,000 kW heat source located at (160 m, 160 m, 0 m). This is canonical fire phenomenology that is illustrated in Figure 1.3.

1.2.1 Restrictions on Modified QUIC-URB in Operational Settings

Computation restrictions are placed on the modified QUIC-URB algorithm and the QUIC-Fire code for it to be viable in operational settings. QUIC-Fire aims to produce results in sub-realtime to be useful in prescribed fire forecasting. QUIC-URB was originally designed to produce a steady state solution for urban environments for emergency response. In typical use the windfield for a transport model would be updated about every 30 minutes. In QUIC-Fire the evolution of buoyant plumes means the windfield must be updated with each update to the fire to capture the wind-fire coupling. The typical time step size to reliably capture the correct fire behavior in FIRE-CA is on the order of seconds. The sub-realtime goal puts a limit on the computational cost of the algorithm and due to this requirement the SOR portion of the QUIC-URB algorithm is restricted to 10 iterations per timestep. This limitation also puts direct limitations on the results from the modified QUIC-URB algorithm. This will be discussed in a later section.

For efficiency the domain QUIC-URB solves over is dynamic and changes depending on the location of the plumes. A buffer is set, $\sigma = n_{iter} + 1$, where n_{iter} is the number of iterations the SOR solver will complete before calculating the updated velocity field. For example, if the

maximum extents of the plumes (in terms of indices) in the x-direction are i_{min} and i_{max} then the start and ending indices for the SOR solver would be $i_{start} = i_{min} - \sigma$ and $i_{end} = i_{max} + \sigma$.

Secondly, in specific scenarios/projects there is a restriction on memory usage by the code of 16GB. This requirement results in great care taken in the memory requirements of algorithms employed in the code. The FIRE-CA algorithm performs optimally at a resolution of approximately 2 meters, meaning that for domains on the order of 1 km the number of cells to track is on the order of 10^6 given around 20 vertical cells. Given this large number of cells single precision is used in lieu of double precision floats and still the memory restriction is a regular obstacle in making improvements to the code.

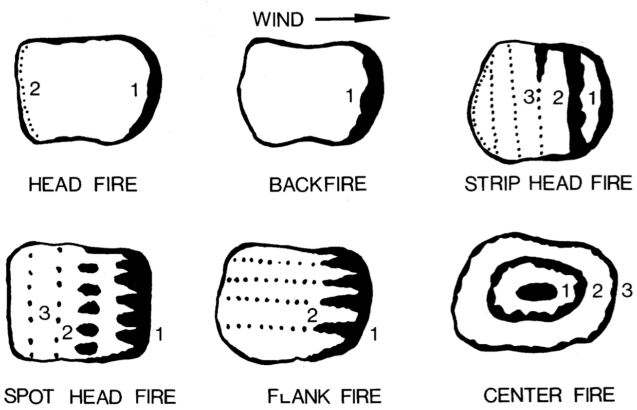

Figure 1.5: Schematics of some prescribed fire strategies and their orientations given the background wind [30]. The numbers shown are the order that each section is ignited.

1.3 Incorporating Terrain into QUIC-Fire

QUIC-Fire has been proven to capture fire behavior in many prescribed fire scenarios, however, these cases that have been explored were on landscapes with no significant terrain. QUIC-Fire was originally developed for simulating fire on flat terrain meaning that QUIC-Fire is not suitable for a great number of domains that contain significant topographical features. Mountainous terrain is well-known to significantly affect the propagation of evolving wildland fires [25, 40]. Terrain not only affects fire propagation by modifying heat transfer patterns due to varying topography, but also the two-way feedback it has with the motion of surrounding air. Wind-fire interaction is a major contributor to emergent fire behavior and thus an important phenomena to capture to correctly predict the behavior of wildland fires [24]. Topography changes these feedbacks through

mechanisms occurring at a wide range of length and time scales [38]. Furthermore, transport and dispersion of smoke plumes is of growing concern, especially in prescribed fire planning and execution [17], but the trajectory of plume movement is also affected by terrain. Accounting for terrain-induced effects on winds, and thus fire and smoke behavior, is an important piece of building a coupled fire-atmosphere model with sound predictive capabilities.

One approach to capturing the dynamic and heterogeneous influences of terrain on winds is solving the full Navier-Stokes equations to resolve the flow at fireline scales which is done in FIRETEC [24] and the Wildland-Urban Interface Fire Dynamics Simulator (WFDS) [31] models or larger scales using Large Eddy Simulation (LES) tools such as in CAWFE [10], WRF-SFIRE [28], or WRF-Fire [11]. Models like FIRETEC and WFDS are too computationally intensive for a real-time forecasting model. The lower-resolution LES-based tools use simplified fire spread models and vegetation representation that limit their generality and applicability for lower intensity fire scenarios, such as prescribed fires, where fine-scale processes and three-dimensional fuels structure greatly influence fire propagation. The development of QUIC-Fire [27] was intended to provide an alternative to these computational fluid dynamics (CFD)-based tools that would be much less computationally expensive than the FIRETEC/WFDS class of models and yet represent some of the processes and three-dimensional structure of the fuel at meter scales.

1.4 Modifications to the QUIC-URB SOR Algorithm

There is a direct consequence of limiting the modified QUIC-URB algorithm SOR subroutine to 10 iterations and the Lagrange multipliers being initialized as zero — the maximum distance the edge of a plume, the last cell with non-zero divergence, can affect is limited to $10\Delta x$ meters. For many cases this means that the induced wind field only has an extent of around 20 meters. This is adequate for single small scale fire as the atmosphere outside of 20 meters would not need resolving to inform FIRE-CA. However, fire-fire interactions play a very important role in prescribed fire through their collective fire-atmosphere interactions [15, 30]. Fire-atmosphere effects have been observed to extend much further than 20 meters in intense fire cases [3, 49, 54].

To improve the successive over-relaxation (SOR) algorithms region of influence while not increasing the iteration count the strategy is to improve the initial guess for each time step from $\lambda = 0$. It must be kept in mind that any initial guess algorithm would need to make minimal computational impact on the algorithm and memory footprint. The CA nature of the code results

in a highly variable source term, $R_{i.j.k}$, for the SOR solver. Constructing an initial guess from $R_{i,j,k}$ would have to include a non-local operation due to the high variability and the dependency of the final windfield on the geometry of the fireline. Due to fires not being tracked as evolving objects in FIRE-CA it would be extremely costly to separate currently burning cells into individual fire shapes and characterize their geometry. There is a substantial amount of literature on producing initial guesses from previous solutions in time dependent problems [29, 56]. The common quality these algorithms share is they use snapshots of previous solutions to construct an initial guess. In [29] low order approximations of the solution are calculated by using the highest weighted eigenvectors of a covariance matrix produced by the singular value decomposition of a solution snapshot matrix. In [56] a parallel process is constructed where multiple time slices are calculated in parallel. At each iteration the iterative solution is passed on to the processor working on the next time slice to be combined to accelerate convergence. This process would perform poorly for QUIC-Fire due to the fires evolution not being calculated in an iterative process and would not be captured. Furthermore, both of these methods have a large memory footprint given that multiple copies of the solution matrix have to be stored and worked on.

A first step in trying to improve the influence region situation is to simply use the previous solution matrix, λ_{prev}, as the initial guess for the next time step. This decision is motivated by the fact that the active burning region does not grow by typically more than 3-4 cells given a time step of 1s and $\Delta x = 2$ m. Also, some fireline geometries, i.e. headfires, conserve their shape if ambient conditions stay constant. This translation of shape means that slight adjustments to the Lagrange multipliers are needed between time steps when compared to starting from $\lambda = 0$. By not resetting the λ matrix the indrafts developed from plumes extend much farther and are able to interact with other developing fires that are greater than 10 indices away. Another effect to be expected from this change is an implicit temporal aspect to the solutions. If we assume $\Delta t = 1\,s$ and we have a single stationary plume contained in a single cell. If the wind field was analyzed at 5 seconds in we would see that at 50 indices away we would have effects driven by the plume at $t = 1\,s$, 40 indices away a mix of effects from the plume at $t = 1\,s$ and $t = 2\,s$, and so on and so forth. These effects also propagate back towards the plume so after some time the wind field will contain some residual effects from the plume at earlier times. I liken this to a synthetic momentum that is introduced from this change as given a certain distance from a plume there is an amount of time for which it will take to 'feel' the induced indraft and an amount of time for the indraft to decay once the

plume has dissipated. This results in a more physical solution as an atmosphere does not change instantaneously due to a source of energy as compared to the solution of the elliptic problem (1.3).

In Chapter 2 the transformation of the QUIC-URB algorithm to a terrain-following (TF) coordinate system is described with analysis of results provided. Chapter 3 describes the incorporation of the TF version of QUIC-URB into QUIC-Fire and results are compared to previously published results produced by FIRETEC. In Chapter 4 concerns for possible pitfalls and performance resulting from using the previous λ matrix as an initial guess are discussed and tested.

CHAPTER 2

DEVELOPMENT OF A TERRAIN FOLLOWING WIND SOLVER

This chapter outlines steps to extend the existing diagnostic wind model, QUIC-URB, to a terrain-following coordinate system for use with the existing fire model, QUIC-Fire, and its contents are published in the Environmental Modelling & Software journal. The derivation and implementation of the wind solver which uses the successive over-relaxation method is described. High resolution, 11–23 m, validation studies using wind measurements over two areas of terrain, a section of the Socorro Mountains and Askervein Hill, demonstrate both successes and shortcomings of the model. The model shows good agreement with data in areas of open sloped terrain but lacks in areas where flow separation and thermally driven effects may be present. Future work that implements parameterizations of wake-eddys, similar to QUIC-URBs building parameterizations, should improve results in some of these areas.

In the following the complex-terrain model formulation (section 2.1), how to solve the resulting differential equation (section 2.2), and two real-world test cases of the model (sections 2.3 and 2.4).

2.1 Terrain-Following Model Extension

To account for the effects of terrain-generated winds, terrain-following (TF) coordinates are adopted, denoted with (x, y, z) and defined as:

$$x = \widetilde{x}, \tag{2.1}$$

$$y = \widetilde{y}, \tag{2.2}$$

$$z = H\frac{\widetilde{z} - h(\widetilde{x},\widetilde{y})}{H - h(\widetilde{x},\widetilde{y})}, \tag{2.3}$$

where H is the domain height at the point of lowest elevation and $h\left(\widetilde{x},\widetilde{y}\right)$ is the terrain elevation at $(\widetilde{x},\widetilde{y})$. Therefore, $z = 0$ corresponds to the surface elevation, $\widetilde{z} = h\left(\widetilde{x},\widetilde{y}\right)$.

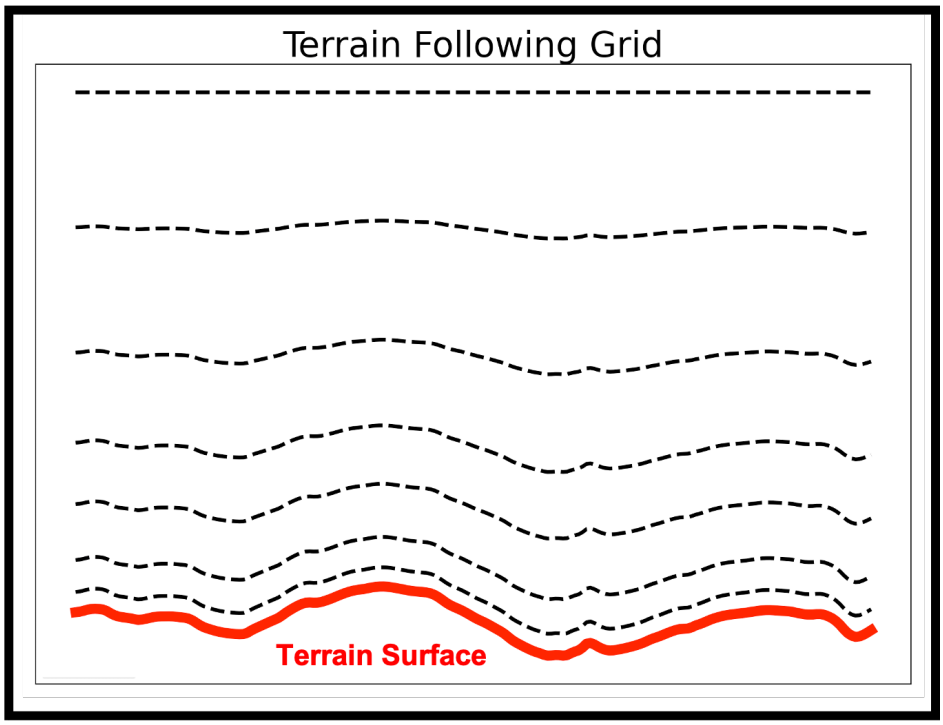

Figure 2.1: An example of a terrain-following grid produced by transforming sigma coordinates back to Cartesian space.

Solving (1.2) in TF coordinates to minimize (1.1) requires expressing the divergence and velocities in contravariant form [32]. This requires using both the covariant and contravariant metric tensors for differentiation and transformations. The covariant basis is calculated by taking the derivative of the original coordinates with respect to the new coordinates,

$$\mathbf{e}_i = \sum_j \frac{\partial \widetilde{x}_j}{\partial x_i} \widetilde{\mathbf{e}}_j, \tag{2.4}$$

and the contravariant basis is calculated by taking the derivative of the new coordinates with respect to the original coordinates,

$$\mathbf{e}^i = \sum_j \frac{\partial x^i}{\partial \widetilde{x}_j} \widetilde{\mathbf{e}}_j. \tag{2.5}$$

Note that superscripts and subscripts correspond to contravariant and covariant quantities, respectively. This results in the contravariant basis

$$\boldsymbol{e}^1 = \vec{i},\ \boldsymbol{e}^2 = \vec{j},\ \text{and}$$
$$\boldsymbol{e}^3 = h_x \frac{z-H}{H-h}\vec{i} + h_y \frac{z-H}{H-h}\vec{j} + \frac{H}{H-h}\vec{k}.^1 \tag{2.6}$$

[1]Subscripts including letters correspond to partial derivatives of the respective direction (i.e., $h_x = \partial h/\partial x$).

It is important to note that under extreme slope values the contravariant basis poorly spans the space at the surface, i.e., $\boldsymbol{e}^3 \times \boldsymbol{e}^1 \approx \mathbf{0}$ if $|h_x| \gg 0$. In some cases it may be necessary to smooth terrain maps to ensure a solution is attainable. The covariant and contravariant metric tensors can be calculated simply by

$$G_{ij} = \boldsymbol{e}_i \cdot \boldsymbol{e}_j \quad \text{and} \quad G^{ij} = \boldsymbol{e}^i \cdot \boldsymbol{e}^j, \tag{2.7}$$

resulting in the two 3×3 matrices

$$G_{ij} = e_i \cdot e_j = \begin{bmatrix} 1 + h_x^2 \left(\frac{H-z}{H}\right)^2 & h_x h_y \left(\frac{H-z}{H}\right)^2 & h_x \left(\frac{H-z}{H}\right)\left(\frac{H-h}{H}\right) \\ h_x h_y \left(\frac{H-z}{H}\right)^2 & 1 + h_y^2 \left(\frac{H-z}{H}\right)^2 & h_y \left(\frac{H-z}{H}\right)\left(\frac{H-h}{H}\right) \\ h_x \left(\frac{H-z}{H}\right)\left(\frac{H-h}{H}\right) & h_y \left(\frac{H-z}{H}\right)\left(\frac{H-h}{H}\right) & \left(\frac{H-h}{H}\right)^2 \end{bmatrix} \tag{2.8}$$

and

$$G^{ij} = e^i \cdot e^j = \begin{bmatrix} 1 & 0 & h_x \left(\frac{z-H}{H-h}\right) \\ 0 & 1 & h_y \left(\frac{z-H}{H-h}\right) \\ h_x \left(\frac{z-H}{H-h}\right) & h_y \left(\frac{z-H}{H-h}\right) & \left(h_x^2 + h_y^2\right)\left(\frac{z-H}{H-h}\right)^2 + \left(\frac{H}{H-h}\right)^2 \end{bmatrix}. \tag{2.9}$$

Both metric tensors share the same determinant meaning they have the same normalization factor

$$\sqrt{|\mathbf{G}|} = \frac{H-h}{H}. \tag{2.10}$$

The contravariant velocities are

$$U^i = \left(\widetilde{u}\vec{i} + \widetilde{v}\vec{j} + \widetilde{w}\vec{k}\right) \cdot \boldsymbol{e}^i, \tag{2.11}$$

resulting in

$$U^1 = \widetilde{u},\ U^2 = \widetilde{v},$$

and

$$U^3 = \widetilde{u} h_x \left(\frac{z-H}{H-h}\right) + \widetilde{v} h_y \left(\frac{z-H}{H-h}\right) + \widetilde{w} \left(\frac{H}{H-h}\right). \tag{2.12}$$

With a covariant metric tensor $\mathbf{G}_{ij}$ and a contravariant velocity field U^i, we calculate the divergence of U^i to be

$$\nabla_i U^i = \frac{1}{\sqrt{|\mathbf{G}|}} \sum_i \frac{\partial}{\partial X^i} \left(\sqrt{|\mathbf{G}|} U^i\right), \tag{2.13}$$

where $X^i = (x, y, z)$. This results in the divergence of the contravariant velocities having the form

$$\nabla \cdot \mathbf{U} = \frac{\partial U^1}{\partial x} + \frac{\partial U^2}{\partial y} + \frac{\partial U^3}{\partial z} - \left(\frac{1}{H-h}\right)\left(U^1 h_x + U^2 h_y\right). \tag{2.14}$$

The contravariant velocities are transformed via $U^i = \widetilde{\mathbf{U}} \cdot \mathbf{e}^i$ where $\mathbf{e}^i$ are the contravariant basis. Using the transformations of (2.14) and (2.12) we transform (1.1) into contravariant terms

to derive the transformed Euler-Lagrange equations. Transforming (1.1) results in

$$E(U^1,U^2,U^3,\lambda) = \int_V \Bigg[\alpha_1^2\left(U^1-U_0^1\right)^2 + \alpha_1^2\left(U^2-U_0^2\right)^2 + \alpha_2^2\Bigg\{\left(U^3-U_0^3\right)\left(\frac{H-h}{H}\right) + \Big[\left(U^1-U_0^1\right)h_x + \left(U^2-U_0^2\right)h_y\Big]\left(\frac{H-z}{H}\right)\Bigg\}^2 + \lambda\left(\frac{\partial U^1}{\partial x} + \frac{\partial U^2}{\partial y} + \frac{\partial U^3}{\partial z} - \left(\frac{1}{H-h}\right)\left(U^1h_x + U^2h_y\right)\right)\Bigg]d\mathbf{x}, \tag{2.15}$$

which can be written as

$$E(U^1,U^2,U^3,\lambda) = \int_V L\left(U^1,U^2,U^3,\frac{\partial U^1}{\partial x},\frac{\partial U^2}{\partial y},\frac{\partial U^3}{\partial z},\lambda\right)d\mathbf{x}.$$

When (2.15) is at its minimum energy, then

$$\frac{\partial L}{\partial f} - \sum_{j=1}^{3}\frac{\partial}{\partial X^j}\left(\frac{\partial L}{\partial f_j'}\right) = 0 \quad \text{and} \quad f_j' = \frac{\partial f}{\partial X^j},$$

where $f = \left(U^1,U^2,U^3,\frac{\partial U^1}{\partial x},\frac{\partial U^2}{\partial y},\frac{\partial U^3}{\partial z},\lambda\right)$ is any of the dependent variables. The result is seven equations that can be reduced to four written as

$$U^1 - U_0^1 = \frac{1}{2\alpha_1^2}\left[\lambda_x - \lambda_z\left(\frac{H-z}{H-h}\right)h_x\right], \tag{2.16}$$

$$U^2 - U_0^2 = \frac{1}{2\alpha_1^2}\left[\lambda_y - \lambda_z\left(\frac{H-z}{H-h}\right)h_y\right], \tag{2.17}$$

$$U^3 - U_0^3 = \frac{1}{2\alpha_2^2}\lambda_z\left(\frac{H}{H-h}\right)^2 - \frac{1}{2\alpha_1^2}\left(\frac{H-z}{H-h}\right)\left[h_x\lambda_x + h_y\lambda_y - \lambda_z\left(\frac{H-z}{H-h}\right)\left(h_x^2+h_y^2\right)\right], \tag{2.18}$$

and the continuity equation

$$U_{0,x}^1 + U_{0,y}^2 + U_{0,z}^3 - \left(\frac{1}{H-h}\right)\left(U^1h_x + U^2h_y\right) = 0. \tag{2.19}$$

Equations (2.16), (2.17), and (2.18) are used to calculate the adjusted velocities once λ is determined. By differentiating (2.16), (2.17), and (2.18), substituting the expressions into (2.19), and rearranging we obtain

$$\lambda_{xx} + \lambda_{yy} + \left[\left(\frac{z-H}{H-h}\right)^2\left(h_x^2+h_y^2\right) + \eta\left(\frac{H}{H-h}\right)^2\right]\lambda_{zz} + 2\left(\frac{z-H}{H-h}\right)\left[h_x\lambda_{xz} + h_y\lambda_{yz}\right] + \left(\frac{z-H}{H-h}\right)\left[h_{xx} + h_{yy} + \frac{2}{H-h}\left(h_x^2+h_y^2\right)\right]\lambda_z = -2\alpha_1^2\nabla\cdot\mathbf{U}_0, \tag{2.20}$$

where $\eta = \alpha_1^2/\alpha_2^2$.

The Laplacian of λ is

$$\nabla_i \nabla^i \lambda = \frac{1}{\sqrt{|\mathbf{G}|}} \sum_i \frac{\partial}{\partial X^i} \left(\sum_j \sqrt{|\mathbf{G}|} G^{ij} \frac{\partial \lambda}{\partial X^j} \right)$$

resulting in

$$\begin{aligned} \nabla_i \nabla^i \lambda = \lambda_{xx} + \lambda_{yy} + \left[\left(\frac{z-H}{H-h} \right)^2 \left(h_x^2 + h_y^2 \right) + \left(\frac{H}{H-h} \right)^2 \right] \lambda_{zz} \\ + 2 \left(\frac{z-H}{H-h} \right) \left[h_x \lambda_{xz} + h_y \lambda_{yz} \right] + \left(\frac{z-H}{H-h} \right) \left[h_{xx} + h_{yy} + \frac{2}{H-h} \left(h_x^2 + h_y^2 \right) \right] \lambda_z \end{aligned} \tag{2.21}$$

which shows we have recovered the contravariant form of (1.2) in (2.20) but with the Gaussian precision moduli incorporated: specifically in the form $\nabla^2 \lambda = -2\alpha_1^2 \nabla \cdot \mathbf{U}_0$ which is the general form of the equation solved in [42]. Open boundary conditions, corresponding to $\lambda = 0$, are implemented on the x, y, and top z boundaries. On the surface a no flux of the wind velocity condition is enforced. This boundary condition is satisfied by imposing $U^3_{z=0} = 0$ and enforcing that $U^3 - U^3_0 = 0$ at $z = 0$ in equation (2.18). This results in the Neumann boundary condition

$$\lambda_z = \frac{h_x \lambda_x + h_y \lambda_y}{\left(\frac{H}{H-h} \right) \left(\eta + h_x^2 + h_y^2 \right)} \tag{2.22}$$

for the terrain surface.

2.2 Computational Method

We solve (2.20) with the Successive Over-Relaxation (SOR) method. The discretization of the domain is the same as the original QUIC-URB [33] grid where the velocities are face-centered and λ is cell-centered, except that it is discretized in sigma-coordinate space. The sigma-coordinate space is a rectilinear grid that is uniform in x and y with vertically-stacked horizontally-uniform layers of varying thickness (typically growing with height) (see Figure 2.2). By choosing a maximum domain height H and discretizing the vertical grid at the same level for all (x, y) positions, a terrain following grid is produced (Figure 2.1) when z is transformed back to Cartesian space by solving (2.3) for $\widetilde{z}$. The terrain following grid conforms to the topography near the surface and flattens to a horizontal plane at $z = H$.

Discretizing the derivatives in (2.20) using central difference stencils produces a sparse linear system that is solved using SOR. An illustration of the discretization points in the sigma-coordinate space for the stencils is in Figure 2.2. Single derivatives in the horizontal direction are discretized as

$$\lambda_x \Big|_{i,j,k} \approx \frac{\lambda_{i+1,j,k} - \lambda_{i-1,j,k}}{2\Delta x},$$

second derivatives are discretized as

$$\lambda_{xx} \Big|_{i,j,k} \approx \frac{\lambda_{i+1,j,k} - 2\lambda_{i,j,k} + \lambda_{i-1,j,k}}{\Delta x^2},$$

and cross derivatives are discretized as

$$\lambda_{xz} \Big|_{i,j,k} = \frac{\partial}{\partial z}\left(\frac{\partial \lambda}{\partial x}\right)\Bigg|_{i,j,k} \approx \frac{1}{\Delta z_k}\left(\frac{\partial \lambda}{\partial x}\Bigg|_{i,j,k+0.5} - \frac{\partial \lambda}{\partial x}\Bigg|_{i,j,k-0.5}\right).$$

When calculating partial derivatives of λ in the x and y directions at horizontally oriented cell walls, $k \pm 0.5$, weighted averages based on cell height are used;

$$\frac{\partial \lambda}{\partial x}\Bigg|_{i,j,k-0.5} \approx \frac{1}{\Delta z_{m,k-1}}\Big[(z_{m,k} - z_k)\,\lambda_x|_{i,j,k} + (z_k - z_{m,k-1})\,\lambda_x|_{i,j,k-1}\Big].$$

For derivatives in the vertical direction, non-uniform cell heights must be taken into account since grid cells typically have increasing vertical size with increasing z. The non-uniformity is accounted for by taking the average of derivatives

$$\frac{\partial \lambda}{\partial z}\Bigg|_{i,j,k} \approx \frac{1}{2}\left(\frac{\partial \lambda}{\partial z}\Bigg|_{i,j,k+0.5} + \frac{\partial \lambda}{\partial z}\Bigg|_{i,j,k-0.5}\right), \tag{2.23}$$

calculated across the top

$$\frac{\partial \lambda}{\partial z}\Bigg|_{i,j,k+0.5} \approx \frac{\lambda_{i,j,k+1} - \lambda_{i,j,k}}{z_{m,k+1} - z_{m,k}},$$

and bottom of the cell

$$\frac{\partial \lambda}{\partial z}\Bigg|_{i,j,k-0.5} \approx \frac{\lambda_{i,j,k} - \lambda_{i,j,k-1}}{z_{m,k} - z_{m,k-1}},$$

where z_m are cell-center heights for the corresponding cells.

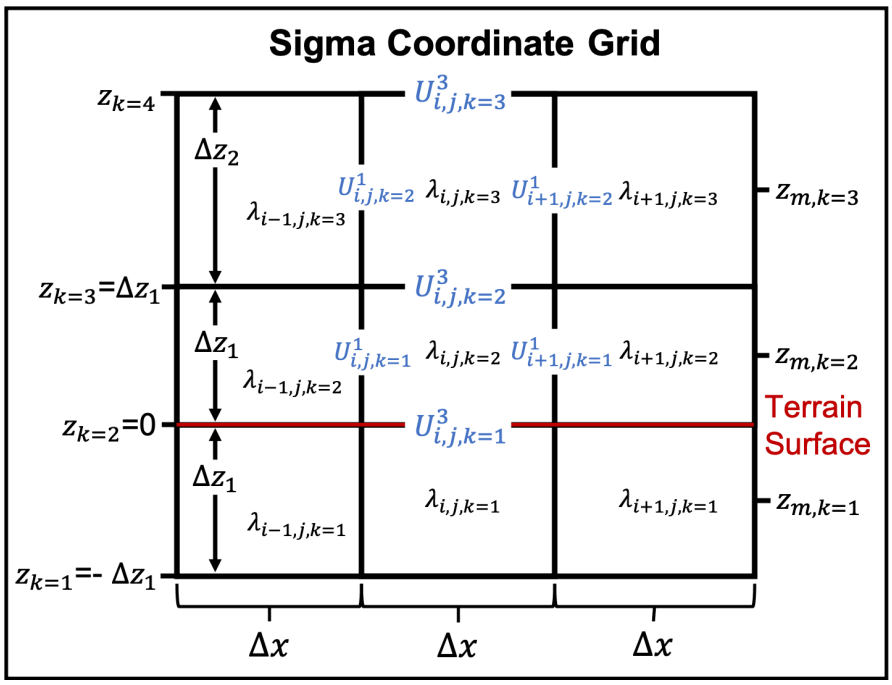

Figure 2.2: A diagram of the sigma coordinate grid showing locations of cell-centered λ values and face-centered contravariant velocities. When calculating the adjustments to the initial velocities, partial derivatives are taken across and along the corresponding cell faces.

The terrain-surface boundary condition, equation (2.22), must be satisfied for all bottom layer cells for $\lambda_z\,\big|_{k-0.5}$ terms. Partial derivatives in the x and y directions are evaluated at the $z = 0$ surface as

$$\left.\frac{\partial \lambda}{\partial x}\right|_{i,j,k-0.5} \approx \frac{1}{4\Delta x}(\lambda_{i+1,j,k=2} - \lambda_{i-1,j,k=2} + \lambda_{i+1,j,k=1} - \lambda_{i-1,j,k=1}),$$

which has a simple form due to both the surface cell and the under-surface cell having an equal vertical cell height of Δz_1. To enforce the boundary condition, λ values below the terrain surface are chosen so that (2.22) is satisfied. To do this we enforce that there is no adjustment to $U^3_0 = 0$ at the surface using the discretized form of equation (2.18), setting $U^3 - U^3_0 = 0$, and solving for $\lambda_{i,j,k-1}$. This results in

$$\lambda_{k=1} = \lambda_{k=2} - \frac{\Delta z_{m,k=1}}{\left(h_x^2 + h_y^2 + \eta\right)\left(\frac{H}{H-h}\right)}\left[\frac{h_x}{4\Delta x}\left(\lambda_{i+1,k=2} - \lambda_{i-1,k=2} + \lambda_{i+1,k=1} - \lambda_{i-1,k=1}\right)\right.$$
$$\left. + \frac{h_y}{4\Delta y}\left(\lambda_{j+1,k=2} - \lambda_{j-1,k=2} + \lambda_{j+1,k=1} - \lambda_{j-1,k=1}\right)\right].^{2} \quad (2.24)$$

[2]Missing i, j, k indices represent no shift in reference location (i.e., $\lambda_{k=2} = \lambda_{i,j,k=2}$).

By substituting the corresponding derivative expressions into (2.20), $\lambda_{i,j,k}$ satisfies the linear system

$$\lambda'_{i,j,k} = \frac{\sum_{i^*=i-1}^{i+1}\sum_{j^*=j-1}^{j+1}\sum_{k^*=k-1}^{k+1} C_{i^*,j^*,k^*}\lambda_{i^*,j^*,k^*}}{D_{i,j,k}} - \frac{2\alpha_1^2\left(\nabla\cdot\mathbf{U}_0\right)_{i,j,k}}{D_{i,j,k}} \quad \text{for } (i^*,j^*,k^*) \neq (i,j,k), \quad (2.25)$$

where C_{i^*,j^*,k^*} and $D_{i,j,k}$ are the combined coefficients multiplying the corresponding $\lambda_{i,j,k}$ and λ_{i^*,j^*,k^*} terms from the discretized form of (2.20). Equation (2.25) is solved using the SOR method which takes the form

$$\lambda_{i,j,k}^{(\ell+1)} = (1-\omega)\lambda_{i,j,k}^{(\ell)} + \omega\lambda'_{i,j,k}, \quad (2.26)$$

where ω is the relaxation parameter and $\lambda'_{i,j,k}$ incorporates λ values from both iteration ℓ and $\ell+1$. Equation (2.26) is iterated for all λ within the cells until convergence is reached. We consider convergence reached when the average change in λ reaches less than 0.1% of the first initial iteration:

$$\frac{\epsilon^{(\ell)}}{\epsilon^1} \leq 0.001,$$

where ϵ is defined as

$$\epsilon^{(\ell)} = \frac{\sum_{i,j,k}\left|\lambda_{i,j,k}^{(\ell)} - \lambda_{i,j,k}^{(\ell-1)}\right|}{n_{\text{cells}}},$$

and n_{cells} is the number of cells used in the domain.

An inputted background wind speed, direction, and height recorded (usually 10 m) is used to initialize the wind field as either a power law or log vertical profile. The profile is fit to match the speed at the height input. The vertical profile is then set for all cells in the domain. Motivated by [36], the vertical contravariant velocities above the surface are

$$w_0 = -\frac{H-z}{H-h}\left(h_x u_0 + h_y v_0\right). \quad (2.27)$$

This equates to $\widetilde{w} = 0$ which generates initial divergence in the field in the presence of terrain. With $\widetilde{w} = 0$ everywhere in the domain it forces the solver to adjust for the no flow boundary condition at the surface. The other reasonable initial vertical component is $U^3 = 0$ everywhere. This results in the initial wind field being aligned with the terrain following grid everywhere, already satisfying the surface boundary condition, and minimal initial divergence being present ($\partial U^3/\partial z = 0$). This leads to a weak topographical influence seen in the resulting wind field and is not the preferred initial guess.

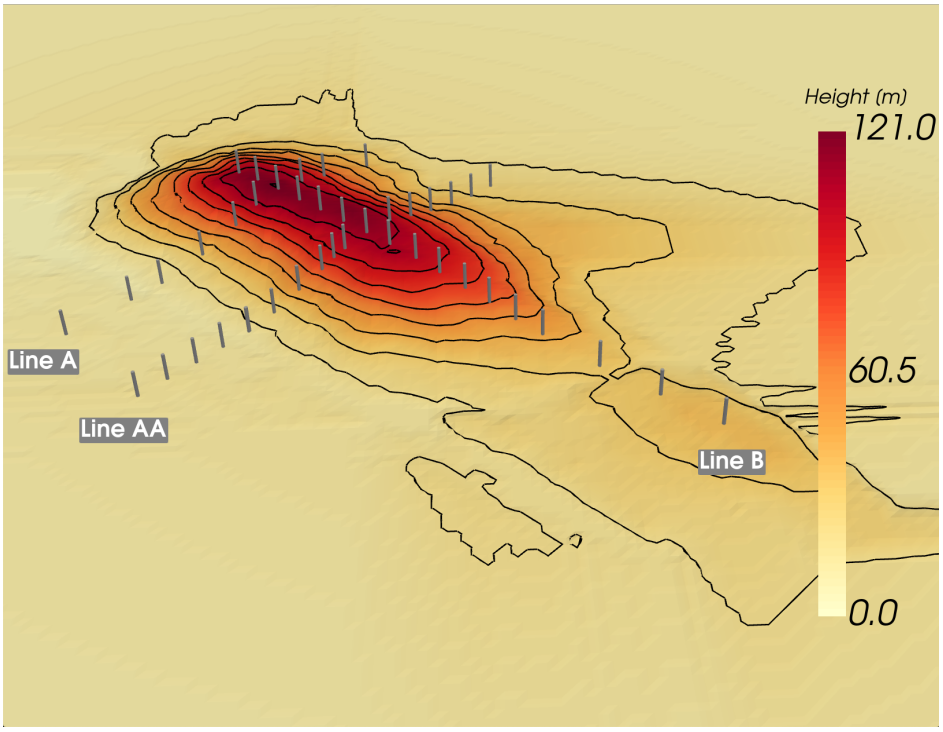

Figure 2.3: A zoomed in portion of the 6 km × 6 km Askervein Hill domain used for the simulation. The image encapsulates approximately a 4 km × 4 km section of the domain. The transects are labeled by name with sensor locations being represented by vertical gray cylinders.

2.3 Askervein Hill

We test our methods on the real world terrain feature, Askervein Hill (57°11.313 N, 7° 22.360 W) [46]. Its simple geometry and isolation from surrounding terrain means that the missing physical dynamics in QUIC-URB, i.e., buoyancy and momentum effects, should not be a dominant factor in wind-field measurements. The simulation uses a similar setup as outlined in [16, 52]. A comparison is made to measured data by using wind measurements during slightly stable atmospheric conditions (Richardson numbers between -0.0110 and -0.0074) along three transects at a height of 10 m that are provided in the MF03-D and TU03B datasets [46]. Sensor locations are illustrated in Figure 2.3. Topography with 23 m horizontal resolution from [53] is used for the surface.

The 6 km × 6 km domain is discretized into 257 × 257 horizontal cells. A vertical extent of 760 m is discretized by a stretched grid of 18 cells growing in height with increasing z. Cell heights range in height from 10 m at the surface to 100.5 m at the top cell. A reference velocity of 8.9 ms^{-1}, 210° from North, measured at a location 3 km upstream, is used to set a power law vertical wind

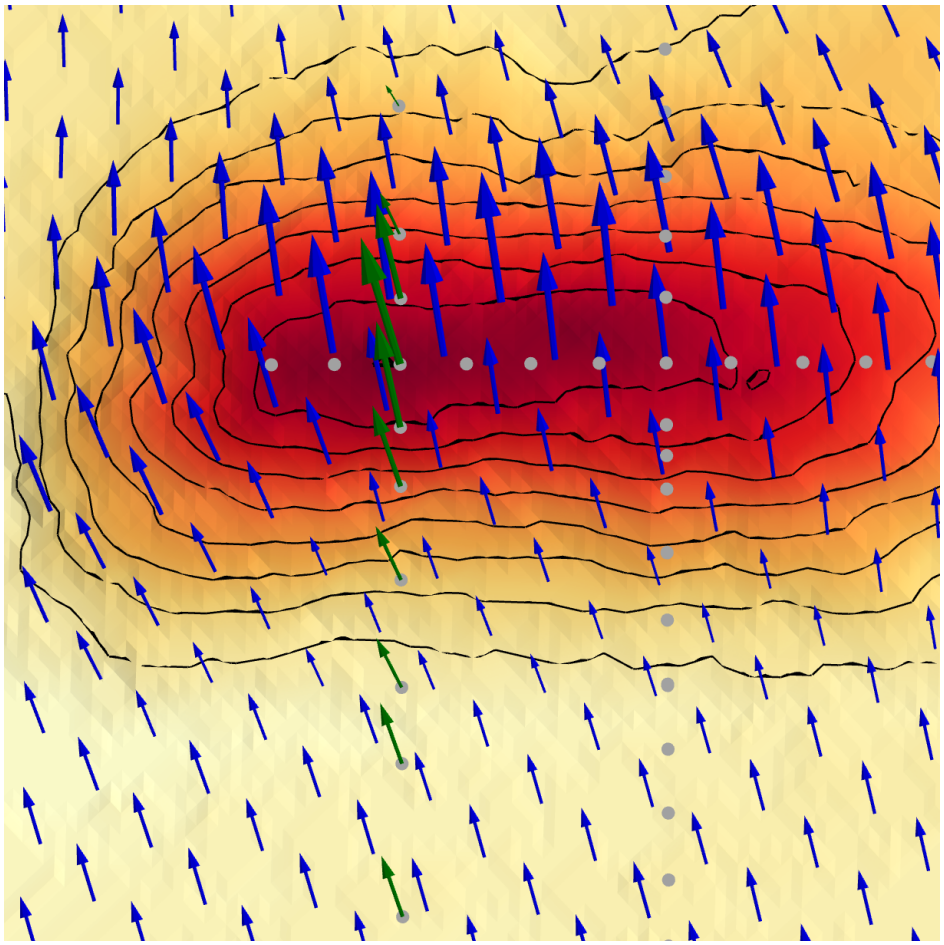

Figure 2.4: A vector plot zoomed in over the larger hill of the Askervein domain. Locations of transect sensors are shown as gray circles, sensor measurement vectors are colored green, and 20% of the surface winds from the QUIC-URB simulation results are colored blue. For visibility all vectors are scaled by a factor of 12.

profile to match the profile data described in [16]. Equation (2.27) is used to set the contravariant vertical velocities so there is no vertical component in Cartesian space above the surface. Using the most aggressive relaxation parameter that achieved convergence, $\omega = 1.9$, 349 iterations are executed on a laptop using 8 threads with OpenMP producing the analyzed wind-field in a total of 6 seconds. A zoomed image of results showing near surface wind vectors can be seen in Figure 2.4.

The wind speeds from the model results, shown in Figures 2.5, 2.6, and 2.7, are linearly interpolated to 10 m above the surface for the comparison at the sensor locations. The QUIC-URB model-computed relative speed up vs. distance near and along the hilltop (Transect B) agrees well with measurements, while the relative speed up vs. distance along Transects A and AA show that

the model agreed well with measurements on the upwind side of the peak, but overestimated speed-up on the downwind side of the hill. The inability of the model to generate flow separation and wake-eddy dynamics is most likely why wind speeds are not retarded sufficiently on the lee side of the hill. Transect A also contains wind direction measurements that are used to compare with QUIC-URB model output. Simulation results show an average direction error of 6.80° with the largest deviation of 17.7° occurring on the leeward side of the hill, in alignment with the poorer wind speed results in the same location. The explanation for the differences on the downwind side of the hill is further supported by [16] where it is shown that including momentum conservation to a mass-conserving model improves the leeward side over-prediction.

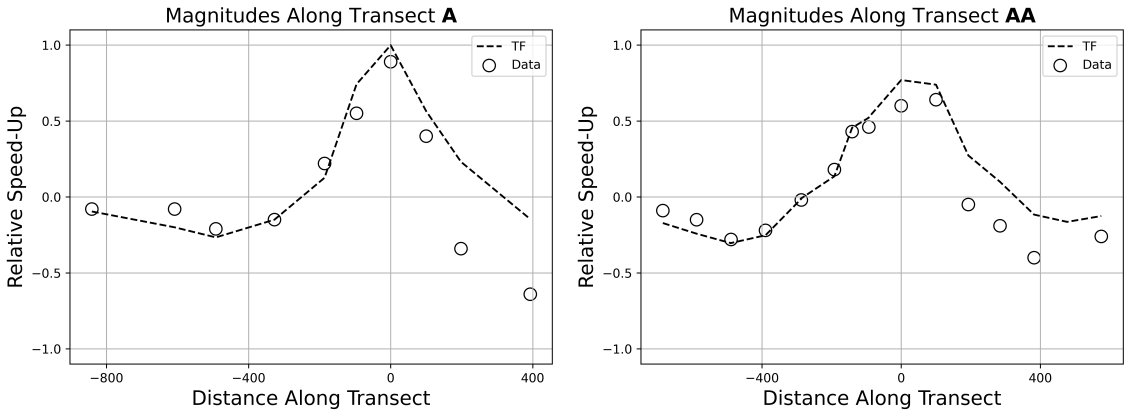

Figure 2.5: A comparison of the measured winds and the results from the terrain-following implementation of QUIC-URB over Askervein Hill along transects A and AA. These graphs show the distance along transect (distance of zero corresponds to the hilltop) vs. the relative speed-up from the reference upwind velocity. Transects A and AA are oriented roughly parallel to the recorded background wind direction meaning positive values on the transect are located on the leeward side of the hill.

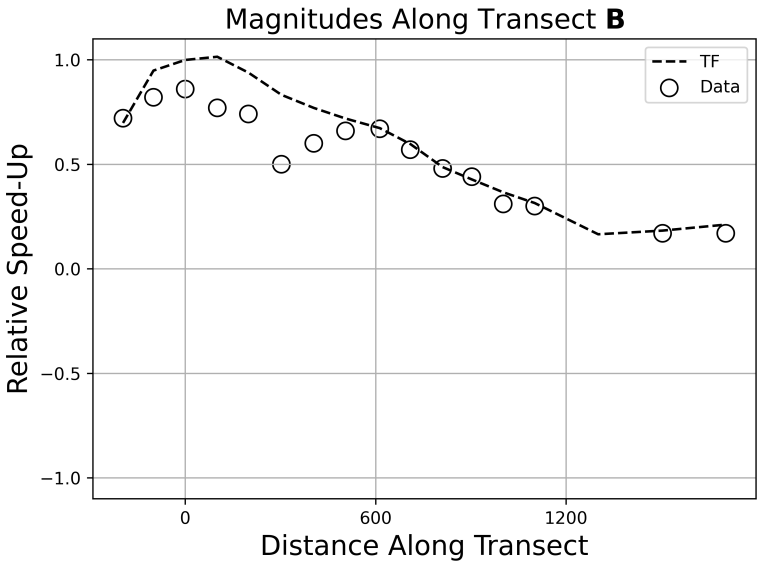

Figure 2.6: A comparison of the measured winds and the results from the terrain-following implementation of QUIC-URB over Askervein Hill along transect B. The graph plots the distance along transect (distance of zero corresponds to the hilltop) vs. the relative speed-up from the reference upwind velocity. Transect B is oriented roughly perpendicular to the recorded background wind direction.

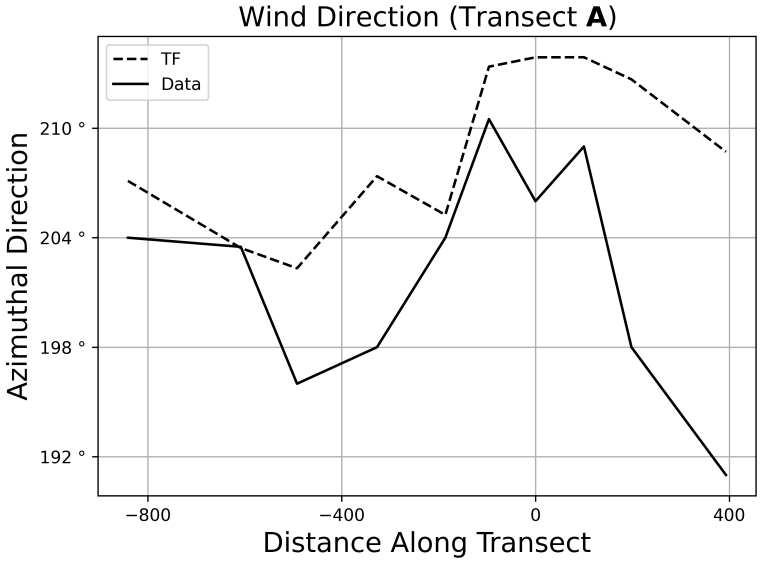

Figure 2.7: A comparison of the wind directions between sensor measurements and model results. The plots show the distance along the transect (distance of zero corresponds to the hilltop) vs. windward direction at the sensor location. Positive values on the transect are on the leeward side of the hill

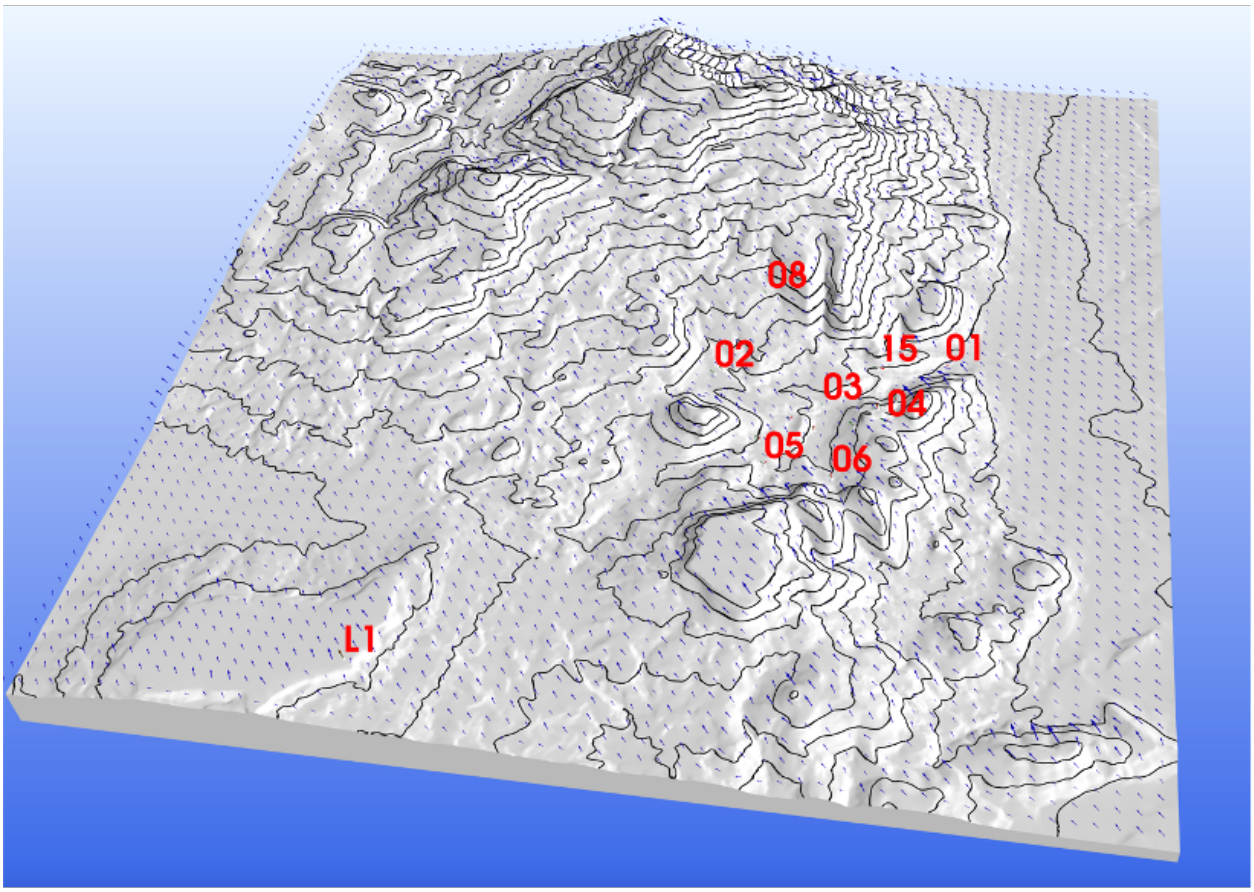

Figure 2.8: The topography of a 6.7 km × 7.0 km section of the terrain surrounding the sensors of the EMRTC field experiment in the Socorro Mountains. Nine of the 18 sensors are labeled at their locations. Note that the L1 sensor, used for the background wind profile of the simulations, is located at the top of a plateau that is isolated from the steep surrounding terrain.

2.4 Complex Terrain

Measurements from a 2019 field experiment at the Energetic Materials Research and Testing Center (EMRTC) in Socorro, NM are used to evaluate the performance of the TF algorithm in a highly complex terrain [6]. The experiment recorded wind speeds and directions over a few weeks in October and November 2019 from 16 sonic anemometers and vertical profiles from two Lidars. Four days of the data are taken where ten minute averages are calculated from the 1 Hz data to reduce turbulent signals for comparison with model output. The terrain surrounding the measurement sites of the experiment is highly complex with many cliff faces, peaks, and valleys that can be seen in Figure 2.8. Measurements from one of the Lidar units, labeled as L1 in Figure

2.8, are used to generate the initial wind field for the simulations by fitting a logarithmic profile to the 10 m measurement. The vertical component of the initial velocity field is set to zero using equation (2.27). The domain for each simulation is 2.25 km $\times$ 2.25 km $\times$ 1 km discretized into $205 \times 205 \times 38$ cells that grow in height with increasing z. The horizontal extents of the domain encompass the sensor sites, higher elevation terrain, and a portion of the low-lying flat section to the East (Figure 2.9).

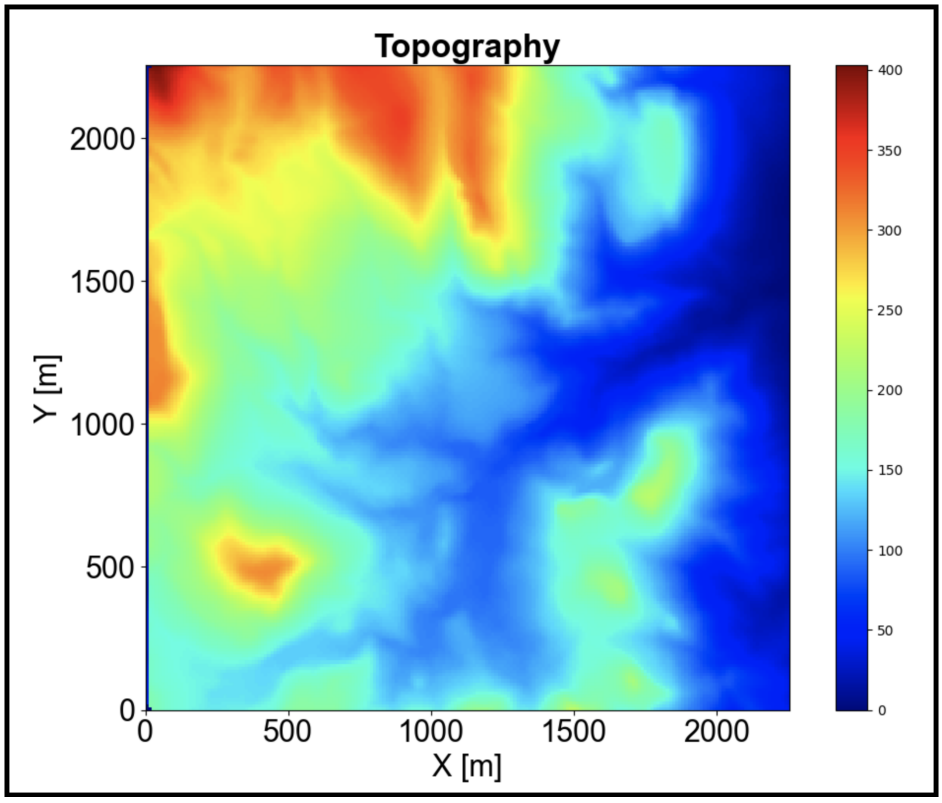

Figure 2.9: The topography at 11 m resolution of the 2.25 km $\times$ 2.25 km section of terrain used for the terrain-following QUIC-URB simulations.

Performance of the model in mountainous terrain is worse when compared to the results seen from the Askervein domain. Results from mid-day and evening measurements, shown in Figure 2.10, highlight areas where the models prediction capabilities are lacking. Although the model captures the magnitude and direction of inlet and outlet areas of the domain (sensors 01, 02, 07, 08, and 15), it performs rather poorly in the valley region (sensors 03, 10, and L2) and in the regions near the steep cliffs (sensors 05, 06, 11, 14, 16, and 17). The poor performance in the cliff regions is due to the models lack of momentum conservation causing an inability to generate the wake regions on the

leeward side of the steep terrain. Also, the current lack of slope-induced thermodynamically-driven flows contributes to poor results in these regions although a version of the solver that includes slope-induced flows is currently being developed. Furthermore, the model does not accurately capture the flow in the valley region because the model is unable to emulate boundary layer dynamics and thermodynamics near the surface. Nonetheless, from a qualitative standpoint the model generates reasonable wind fields especially using only a single wind profile for input.

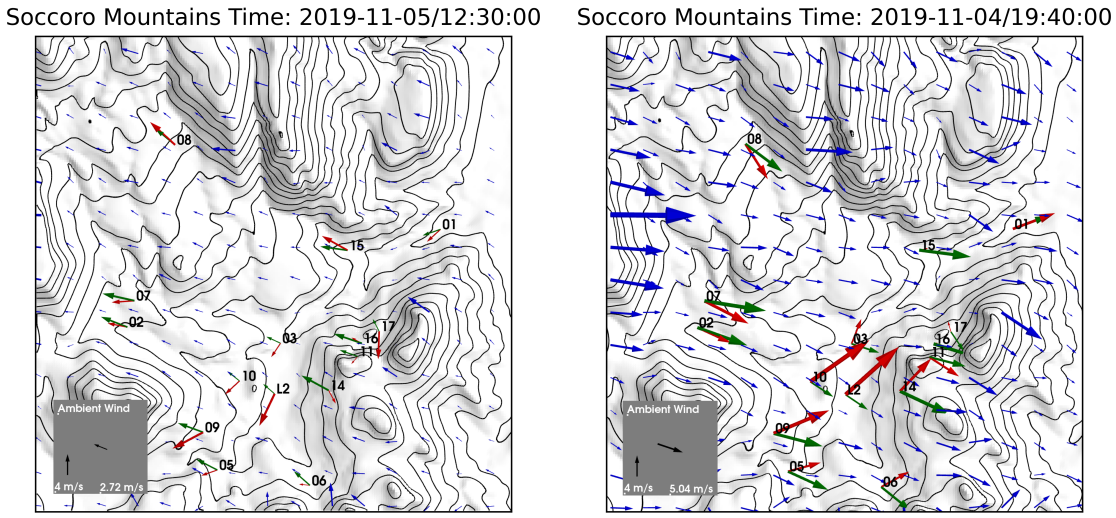

Figure 2.10: Vector plots comparing measurements and simulations of the terrain-following implementation of QUIC-URB applied to winds in the Soccorro mountains at 12:30 PM and 7:40 PM local time. The background wind at 10 m and the scale for the model-computed blue vectors are illustrated in the grey inset. The red vectors represent sensor measurements, labeled by sensor number, and the green vectors are model results interpolated to the sensor locations. Both the red and green vectors are scaled up by a factor of three to make the comparison easier.

2.5 Conclusions

This section discusses the mathematical formulation of a diagnostic wind model for flow over complex terrain using TF coordinates. The model shows strong performance in the Askervein case, capturing the general profile recorded by sensors. In a complex terrain environment the model struggles to capture flow dynamics near cliffs and in areas occluded by surrounding terrain. To help performance around cliffs, future work includes extending the wake-eddy parameterizations used in QUIC-URB for urban environments [33] to the TF coordinate system. Additional work is needed to capture flow dynamics that occur from thermodynamic effects and boundary layers although

a version is currently being developed that includes slope-induced flows. Boundary layers might be incorporated by partitioning the domain into separate regions with new boundary conditions at their interfaces. Despite these shortcomings of the model, the solver will be useful to integrate into QUIC-Fire and to incorporate important terrain effects into a fine scale fire model. With knowledge of TF QUIC-URB's over-prediction of winds, fire simulation results will have to be interpreted carefully in complex terrain regions before more complex methods are integrated into the wind solver.

CHAPTER 3

PERFORMANCE OF QUIC-FIRE USING TERRAIN-INFLUENCED WINDS

3.1 Introduction

This chapter discusses a first step in the extension of QUIC-Fire to enable its use for simulating wildland fire activity in complex terrain, leveraging the complex terrain version of QUIC-URB. The contents of this chapter are submitted to the Environmental Modelling Software journal for publication. The discussion will cover the 1) coupling of a TF version of QUIC-URB to FIRE-CA and 2) the implications of using terrain-influenced winds to drive upslope wildland fire spread with the preexisting fire spread algorithm in QUIC-Fire. The changes to FIRE-CA are limited only to what is necessary to correctly include the complex terrain version of QUIC-URB. This is a first step in accounting for the effects terrain has on a propagating fire. Since this study avoids changes to the FIRE-CA model, the effects of resolved terrain-driven winds on fire behavior is isolated and this driver of changing fire behavior between QUIC-Fire versions may be studied. This also allows for the identification of dynamics that the model is not capturing to focus ongoing model refinement efforts. A description of the extent of the new capabilities and modifications required to integrate the TF version of QUIC-URB is provided. Also, some of the shortcomings of this extension as it is currently formulated is discussed. A demonstration of some of the current capabilities through comparison against published simulations using HIGRAD/FIRETEC is provided. Making comparisons with real-world data would be preferred but the availability of fuel, wind, and fire propagation data at scales and resolutions relevant for QUIC-Fire to recreate a fire experiment is non existent. Efforts have been made to recreate fire behavior from burn experiments that were designed for use as a validation data set [22, 26]. These efforts ultimately found that recreation required characterization of winds at multiple scales, which QUIC-Fire is not inherently sensitive to, and a non trivial combination of wind measurements to achieve the best results. The complex variability of winds in most real-world fire scenarios and the sensitivity of most fire spread models to wind velocities makes it a near impossible effort to recreate a spread pattern without adjustments made to input data effectively becoming a parameter fitting exercise. Results from [22] illustrated that slight

changes in ignition times and wind sampling techniques resulted in drastically different simulation spread results. Keep in mind these experiments were conducted in domains with negligible terrain meaning complex effects from surrounding terrain or the terrain itself were not considered and would add further difficulty in efforts to compare spread rates with real-world data containing significant terrain. In the following, when referring to QUIC-Fire, this refers to the new version with the TF winds and the modified fire spreading algorithms to account for terrain. The results from QUIC-Fire reported in this chapter on average are computed in about half of the real-time simulated.

3.2 QUIC-Fire Overview

QUIC-Fire was specifically designed to be able to simulate a wide range of wildland fire scenarios, including prescribed fire, without requiring extensive computational resources while still capturing the coupled fire-atmosphere interactions necessary for accurately predicting fire behavior. QUIC-Fire achieves this coupling by linking the fast-running QUIC-URB wind field solver to the FIRE-CA fire spread algorithm. QUIC-URB was adapted to incorporate buoyant updrafts generated from the energy release of combusting fuel, which is calculated by FIRE-CA. By enforcing mass-consistency on a background wind field perturbed by these buoyant updrafts, QUIC-URB generates indrafts close to the fireline, thus allowing the FIRE-CA algorithm to account for buoyancy-induced entrainment. This two-way coupling forms the basis of the fire spread dynamics captured by the QUIC-Fire model.

It is important to highlight the differences in methodologies between QUIC-Fire and a full physics model like FIRETEC. FIRETEC resolves wind flow directly at fireline scales by solving the Navier-Stokes equations and models the combustion of fuels by tracking temperature and chemistry of an evolving fire. QUIC-Fire models the propagation of fire by discretizing the amount of energy released by combusting fuel into Energy Packets (EPs). The generated EPs are transported based on local fire-modified winds, fire intensity approximations, and stochastic modifications via turbulence approximations that are based on calculated wind shear around each cell. The EPs can contribute to the drying of fuel, the combustion of dried fuel, and, if they do not land on fuel, the generation of buoyant updrafts. The regions of dried, burning, and depleted fuels within each cell are tracked and oxygen availability is approximated based on local conditions. The details of the coupling and explicit equations of QUIC-Fire can be found in [20]. Both QUIC-Fire and FIRETEC

are full 3D simulations that are sensitive to both vertical and horizontal fuel heterogeneity. The 3D fuel grid allows for these models to track when a fire transitions from surface fire to a crown fire and the mechanisms for which that happens, whether it be due to ladder fuels or high surface loading.

3.3 Effect of Topography on Winds and Fire Spread

Changes implemented to the FIRE-CA algorithm are limited to those required to correctly incorporate the wind fields generated by TF version of QUIC-URB. This allows me to investigate how terrain-influenced winds change the fire behavior of the FIRE-CA algorithm. This involves implementing the Successive Over-Relaxation (SOR) solver to work on a TF grid, choosing a fuel grid geometry, and accounting for terrain-induced flow on the transport of the buoyant updrafts.

3.3.1 Terrain-Influenced Winds

The first step is to generate terrain-influenced background winds, which is a crucial component to predict fire behavior on a landscape characterized by topographical features. Terrain can cause complex three-dimensional patterns including channeling in canyons and valleys and flow blocking or diverting [38, 50], which can have nonlocal influences on wind fields. These terrain-induced wind patterns have been shown to drive drastic changes in fire behavior that terrain slope cannot account for alone [9, 40]. To incorporate terrain-induced winds while also retaining the low-computational cost of QUIC-Fire, the original Cartesian grid of QUIC-URB is modified into a TF coordinate system to capture the wind gradients close to the ground with a fine grid resolution (meter scale) and allow for grid stretching as one moves higher in the atmosphere where less pronounced changes in wind speed and direction are expected. A detailed description of that effort can be found in [34]. In its current state, it does not contain momentum effects (e.g. separations) or thermodynamically driven effects (e.g. drainage flows), but, future work is planned to address these shortcomings. In [34], it can be seen that this effort allowed capturing terrain-induced effects like wind speed-up over terrain features and stagnation points at the base of large features. Hence, it can be useful to analyze fire spread over varying terrain configurations and wind conditions where separations and drainage flows are not expected to be significant factors.

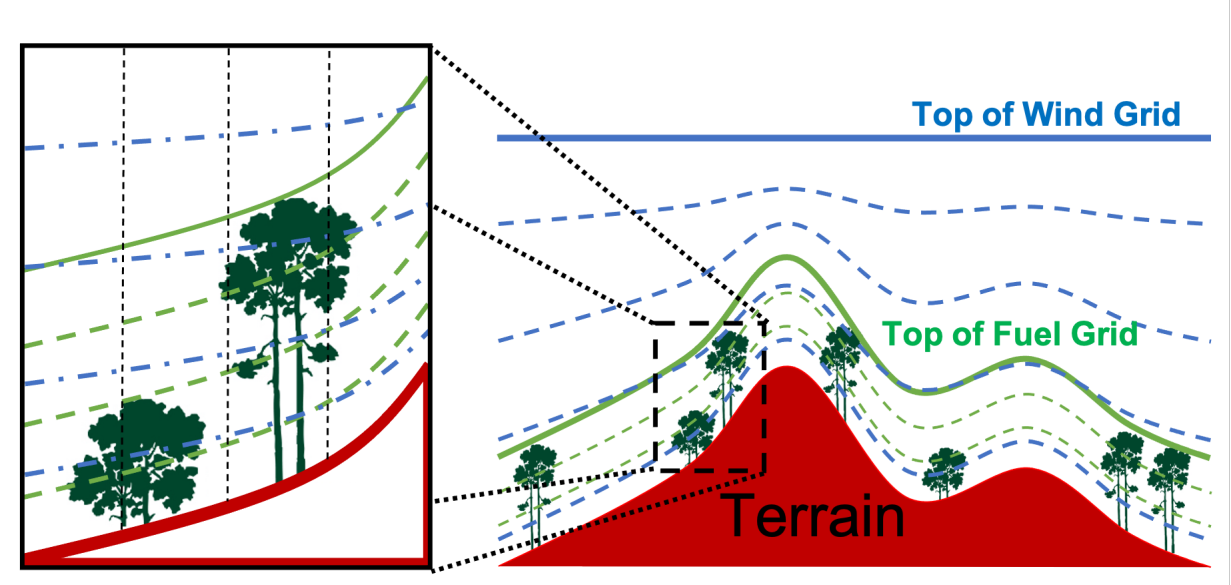

Figure 3.1: Diagram showing how the fuel grid, green lines, and QUIC-Fire grids, blue lines, align with each other. The vertical extent of each grid is denoted with a solid line and the lower cell tops denoted with dashed lines. The vertical resolution of the draped fuel grid stays constant whereas the terrain-following grid of the wind grid is compressed in the presence of terrain. The dashed black lines in the expanded window demonstrate the horizontal discretization that both grids typically share.

3.3.2 Fire-CA Grid for Terrain Effects

While wind gradients tend to become more smooth as one moves upwards in the atmosphere, allowing for a TF stretched grid, the three-dimensional fuel structure and its gradients remain important from the surface to the top of the canopy. I therefore used a draped grid to capture the fuel vertical structure in which the height of cells in the fuel grid do not change size with the varying elevation of topography. The draped fuel grid has the advantage of simplifying the computation of the fate and transport of energy in FIRE-CA and generation of 3D fuels inputs as fuel voxels can be generated while only considering height above ground. Unfortunately, a consequence of this choice is that a non-trivial interpolation needs to be carried out between the TF wind grid and the draped fuel grid each timestep as the deformation of the wind grid depends on the terrain height at each cell position (see Figure 3.1). This is necessary as the FIRE-CA algorithm requires the local wind speed in each cell to calculate fire spread.

Energy that is released by the combustion process in QUIC-Fire is carried either upward by strong updrafts or parallel to the surface based on the local fire-influenced wind fields. At the

terrain surface to separate the proportion of EPs that are carried vertically by updrafts versus being transported parallel to the surface the local wind velocity $\vec{v} = \langle u, v, w \rangle$ is transformed. A component parallel to the local slope $\vec{v}_{||}$ and a perpendicular component $\vec{v}_{\perp}$ are calculated from $\vec{v}$ such that $\vec{v}_{||} \cdot \vec{v}_{\perp} = 0$. The vectors $\vec{v}_{||}$ and $\vec{v}_{\perp}$ are then projected onto the local slope vectors in the x and y directions, respectively, resulting in the surface winds

$$v_{h_x} = \frac{u + h_x w}{\sqrt{1 + h_x^2}}, \tag{3.1}$$

$$v_{h_y} = \frac{v + h_y w}{\sqrt{1 + h_y^2}}, \tag{3.2}$$

$$v_{\perp} = \frac{w - h_x u - h_y v}{\sqrt{1 + h_x^2 + h_y^2}}, \tag{3.3}$$

where h_x and h_y are local terrain derivatives in the x and y direction, respectively. The ratio of $||\vec{v}_{\perp}||$ over $||\vec{v}_{||}||$ determines the chance that an EP will separate from the surface and travel upward into to fuel cells higher up. A schematic of this decomposition can be seen in Figure 3.2. These decomposed winds also define the length scale that the EPs travel. Another adjustment to account for the draped grid and horizontally launched EPs is to multiply the resulting EP travel distance from the Fire-CA algorithm by $|\cos(\theta)|$, where θ is the local elevation angle of the fuel cell in the direction the EP is travelling. This is done as distances traveled in the fuel grid are not calculated by integrating along the terrain surface.

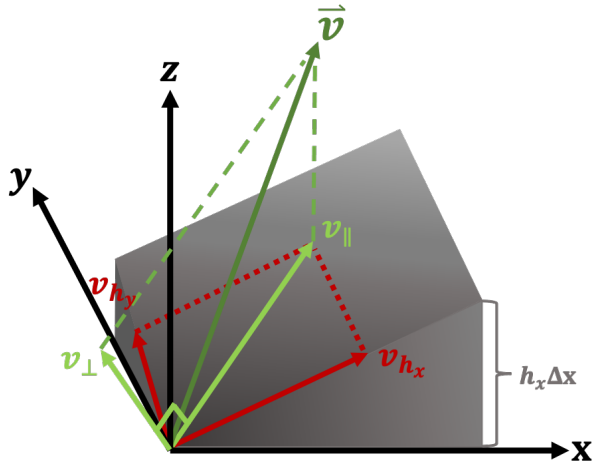

Figure 3.2: Schematic of the wind vector decomposition carried out for surface fuel cells.

3.3.3 Buoyant Plume Transport in Complex Terrain

The buoyant plume model in the original QUIC-Fire considered only flat terrain. The horizontal motion of the plumes in the model is governed by background wind whereas the vertical loft and lateral expansion are parameterized with the Briggs theory [12]. The implementation of this is done by recalculating the plume radius and centerline updraft at each point on the trajectory. However, this model is derived for a plume traveling over a flat surface and vertical background wind is not considered.

The QUIC-Fire plume rise scheme is modified to account for the topographically influenced background winds where plumes are now advected vertically with the background winds vertical component in addition to following the Briggs trajectory. This is motivated by simulations carried out with FIRETEC. To analyze the buoyancy-induced flow without the complications of a moving fire the fuel combustion routines in FIRETEC are disabled and a constant heat source of 2000 kWm^{-1} is placed across a single cell. The constant heat source raises the temperature of the surrounding air and generates a buoyant plume and emulates a cell emitting constant heat (or releasing constant EPs to the atmosphere). Two FIRETEC simulations, one with flat terrain and another with a prominent hill, with the same logarithmic wind profile for initialization are used to compare the influence of a downwind obstruction on plume trajectories. QUIC-Fire is also modified in the same way with the same heat source in a single cell. Figure 3.3 shows results from these simulations and results. In Figure 3.3 comparisons between FIRETEC simulations, (a)→(b) and (d)→(e), illustrate that the plumes are transported vertically with the background wind field when comparing trajectories between plumes. When comparing (b)→(c) and (e)→(f) the modification of advecting plume segments vertically with the background wind in QUIC-Fire results in similar plume profiles as the full CFD code FIRETEC. QUIC-Fire results underestimate the upward boundary of the plume, but capture the intensity of the updraft at the ground, where most of the fire activity is.

3.4 Comparison of FIRETEC and QUIC-Fire on Ideal Terrain Configurations

Due to the complexity of measuring all of the variables involved in a propagating fire front (3D fuel loads, local wind conditions, fuel moisture, temporal evolution of fire intensity, heat released to the atmosphere), it is difficult to adequately characterize real-world fire scenarios to fully understand

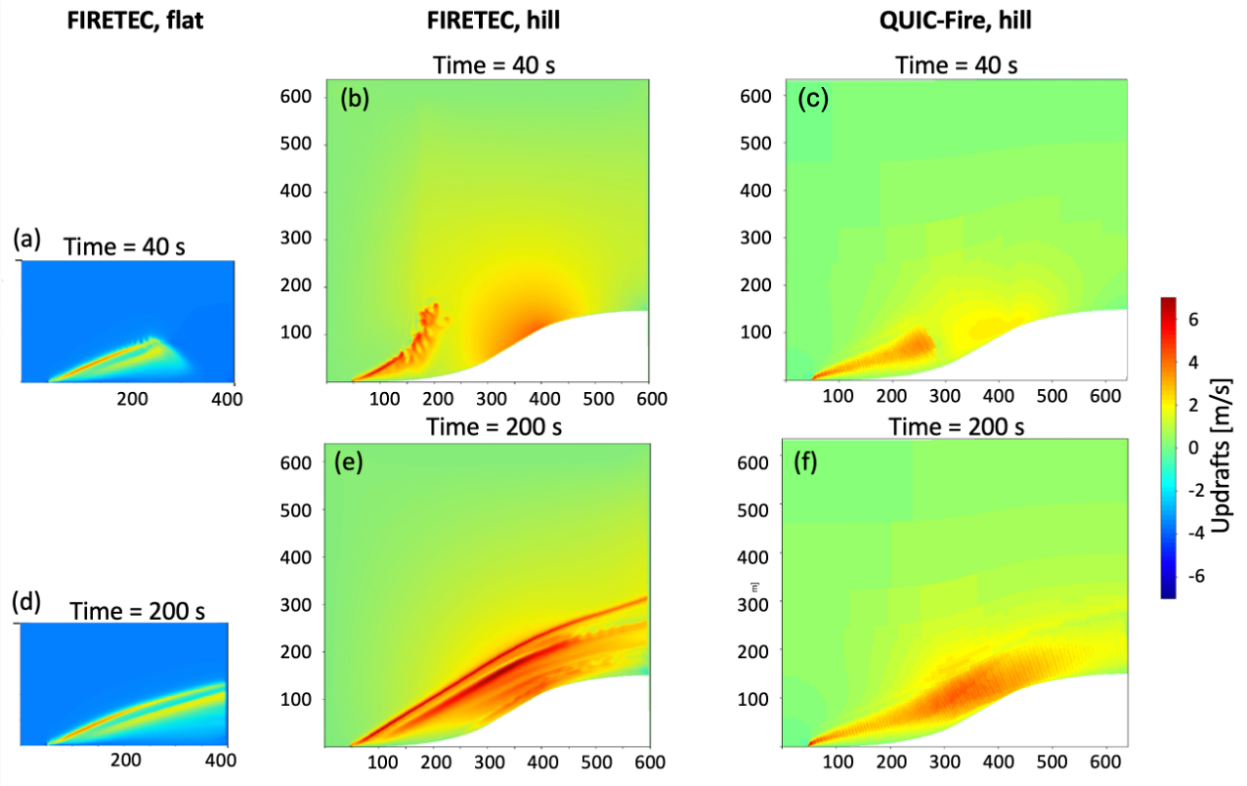

Figure 3.3: Vertical contours of vertical velocities in FIRETEC and QUIC-Fire to compare buoyant plume trajectories with and without terrain. Plots (a) and (d) show FIRETEC simulations on flat terrain to show the impact of terrain (plots are scaled to match the other plots). As one can see in the center (FIRETEC) and the right (QUIC-Fire), the buoyant plumes, here identified with the updrafts, are bent upward by the hill. QUIC-Fire results underestimate the upward boundary of the plume, but capture the intensity of the updraft at the ground, where most of the fire activity is. The simulations use a constant heat source of 2000 kWm^{-1} across a single cell to generate the buoyant plumes. All lengths are in meters in the plots.

the abilities of a coupled fire-atmosphere fire model like QUIC-Fire to capture the influences of topography on fire spread. One alternative is to examine the fire behavior predicted by QUIC-Fire to published topographically-influenced fire scenarios that have been simulated using higher fidelity models. Thus, to test how responsive the current version of QUIC-Fire is to multiple idealized topographies and winds, ten simulations are carried out to compare to FIRETEC simulations described in [21].

3.4.1 Description of the Simulation Domains

The extent of the domain in the simulations is 640 m×320 m×700 m with a horizontal grid spacing of 2 m in x and y. The QUIC-URB grid is a stretched vertical grid with a spacing of 1 m near the ground, growing linearly to 3 m until the top of the canopy, and increasing exponentially to 200 m at the top of the domain. The fuels grid vertical resolution is 1 m over the entire horizontal extent of the domain and defined from the ground to the top of the canopy. The statistical properties of the tree distributions are the same as in previous FIRETEC-based study [21], meaning the placement of the individual trees is not the same in the two sets of simulations but the overall forest fuel distribution is captured. The fuel setup consists of one region of homogeneous grass, 0.7 m tall, with a fuel load of 0.7 kg m^{-2}, and another region where the vegetation resembles a Ponderosa pine forest with inhomogenous grass and litter surface fuels. These two regions transition across a line tilted at 45° to the ambient wind (Figure 3.4). The fuel bed is generated using the same methodology used in [21] and described in [23]. The pine forest section uses over 8,000 Ponderosa pine trees where "...the discrete fuel elements used to model trees are based on data collected by the USDA Forest Service Rocky Mountain Research Station and Northern Arizona University as part of the Joint Fire Sciences Program, Fire and Fire Surrogate Treatment Project. The canopy bulk density over the forested area is 0.12 kgm^{-3}, with an average tree height of 13.8 m (minimum of 7.3 m, maximum of 19.9 m) and an average height to live crown of 8.7 m (minimum of 3.9 m, maximum of 13.4 m). The moisture fraction of the grass fuel bed is 0.05 (kg water mass/kg dry fuel mass) and the canopy moisture fraction is 0.80 of the dry fuel mass." [21]

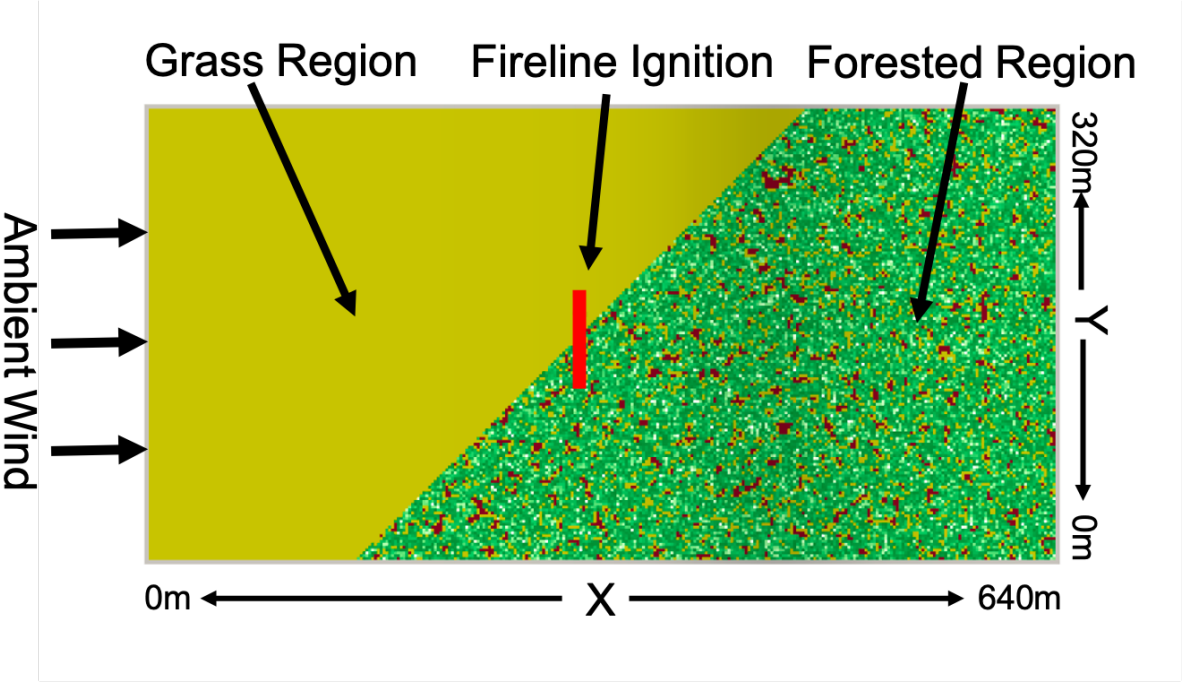

Figure 3.4: Top view of the computational domain showing domain extents, fuels, fireline position, and ambient wind direction for the simulations.

A 60-m long and 8-m wide fireline is ignited instantaneously 300 m from the upstream domain boundary such that it is split length-wise at the interface between the forested and un-forested fuel regions. The wind is oriented in the direction of the positive x-axis so that the fire will be blown into the forested area. The background wind flow for the QUIC-Fire runs are generated via the process described in [34] where a background logarithmic profile is set throughout the domain and mass-conservation is enforced to account for terrain effects.

The topographies used consist of a flat topography that will be referred to as the 'Flat' case; the remaining topographies are all unique but share a common centerline downwind of the ignition line along the y=160 m transect (Table 3.1). These topographies sharea common centerline and the same elevation gradient along the center allowing me to study the effects of variations in the topography in the lateral and upwind directions. The four non-flat topographies share the same base topography elevation (*base*) which provides the shared centerline profile,

$$base = 55 + 40 \tan^{-1}\left(\frac{(x - 300) - 140}{60}\right),$$

where x is downwind direction and it propagates to all crosswind coordinates. This topography is labeled as 'Hill' in Table 3.1. The change in elevation from the ignition line (x=320 m) and outlet of the domain (at x=640 m) is 106 m. The other topographies, explicit functions provided in Table 3.1, are modulated forms of the Hill topography. The 'Canyon' topography introduces a mirror of the hill in the upwind direction. This results in a canyon that is perpendicular to the background wind direction with an inlet height of 103 m. The upward canyon topography, 'Upcan', modifies the topography by increasing the height of the hill symmetrically with distance from the centerline while leaving the centerline profile unmodified. The elevation of the Upcan case rises to 211 m at the y edges of the domain. For the 'Ridge' topography the modification that is added to the base topography to generate the Upcan case is instead subtracted from the base topography. This generates downward slopes in the lateral directions where elevations drop to 1 m at the y edges of the domain.

To generate background winds like those used in [21], similar boundary conditions on the x and y boundaries need to be enforced in QUIC-Fire. The wind fields used in [21] are ramped up over 12 s of simulation time from no wind to 6 or 12 ms^{-1} while nudging the winds at the boundaries to the background values. This results in an inlet with a wind profile with similar values of the specified wind speed in the x direction and and no flow through the y boundaries. To attain a similar background wind with QUIC-Fire, homogenous Neumann boundary conditions are enforced across the inlet interface, $x = 0$, and lateral interfaces, $y = 0$ and $y = 320$ m. This keeps the wind profile at the inlet interface static and velocities at the lateral interfaces in line with the boundary edges where slopes in the y-direction are zero (Hill and Canyon). In cases where slopes in the y-direction are not zero at the domain boundaries (Upcan and Ridge) the boundary condition does not require winds to be aligned with the x-direction. The wind solutions generated at the boundaries are easiest to understand by substituting the boundary conditions into the velocity update equations from [34], rearranging, and looking at the two limiting cases

$$\Delta v = \frac{-h_x h_y \Delta u}{\eta^2 + h_y^2,} \text{ at } z{=}0$$

and

$$\Delta v = 0, \quad \text{at top of domain,}$$

where $z = 0$ corresponds to the terrain surface, Δu and Δv are the adjustments made to the initial wind field for mass conservation, h_x and h_y are partial derivatives of the terrain elevation h, and

η is a weighting parameter that is one when generating background winds. Given that QUIC-Fire generates speed-up of winds as they are pushed up hill ($\Delta u > 0$ for inflow from $y = 0$ m), this boundary facilitates the channeling of winds from the boundary seen in the Upcan case background wind fields (Table 3.1). The outlet, x=640 m, is an open boundary.

The same naming convention for test cases is adopted from [21] to make comparison easier. For example, a case where a 6 ms^{-1} background wind is imposed in input to the Hill topography will be referred to as Hill6; this convention is used for the remainder of the dissertation.

3.5 Results and Discussion

Results from the QUIC-Fire and FIRETEC simulations are compared to determine what fire spread dynamics this version of QUIC-Fire captures and where it fallsl short. Downwind propagation rates, spread rates across a few select regions of the domain, and lateral spread are investigated.

3.5.1 Fire Spread Rates

Figures 3.5, 3.6, 3.7, 3.8, and 3.9 show fire shape of FIRETEC and QUIC-Fire for the 6 ms^{-1} and 12 ms^{-1} simulations. Propagation distances in the x-direction (ambient wind direction) are shown in Figure 3.10 where the distance is measured in the horizontal x direction instead of along the terrain surface to make comparison between cases easier. The extent of the fire is determined by finding the farthest downwind cell that had lost fuel for a given time. The computation of the fire propagation distance is stopped once the fire front is within 20 m of the edge of the domain to avoid any edge effects altering results. Hence, results refer to either 100 s or 150 s after ignition depending on the case. (see captions) Figure 3.10 compares the front propagation profiles between FIRETEC and QUIC-Fire and demonstrates similar grouping between cases with identical centerline profiles (Group 1: Hill, Upcan, and Ridge; Group 2: Flat and Canyon) for both the 6 and 12 ms^{-1} cases. The grouping is tighter in FIRETEC, but the similarity in the fire spread profiles can still be seen for QUIC-Fire results. Arrival times at the downwind edge of the domain are also similar between FIRETEC and QUIC-Fire although the ordering of which case arrived first is reversed between the two groups in the QUIC-Fire results. A trend that is clear between all of the QUIC-Fire terrain cases is the acceleration in fire spread once a propagation distance of $\sim$100 m is reached. The increase in spread rate is due to the fire front reaching the location where the terrain gradient in the downwind direction along the centerline increases substantially. This coincides with where background wind speeds begin increasing significantly in the QUIC-Fire generated wind fields. The

Table 3.1: Description of the five topographies used in the simulations. Vectors in the images are near surface background winds generated from the terrain-following version of QUIC-URB.

Name	Ground height (h) function	Topography
Flat	$h = 0$	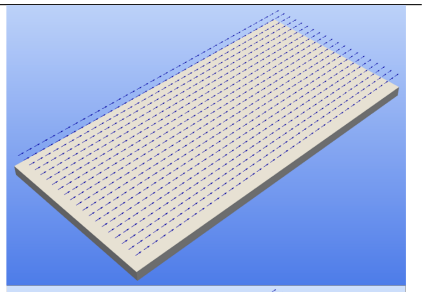
Hill	$h = base$	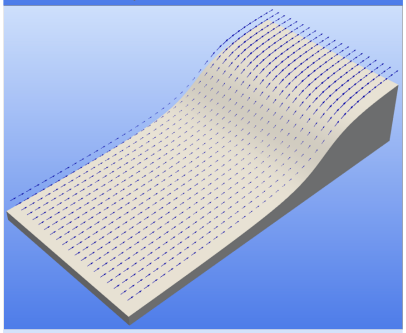
Canyon	$h = \left\{ \begin{array}{cc} 55 + 40\tan^{-1}\left(\frac{\lvert x-300\rvert-140}{60}\right) & \text{for } x < 300\text{m} \\ base & \text{for } x \geq 300\text{m} \end{array} \right\}$ Note: The elevation at the inlet wind (left) end of the topography is 103 m.	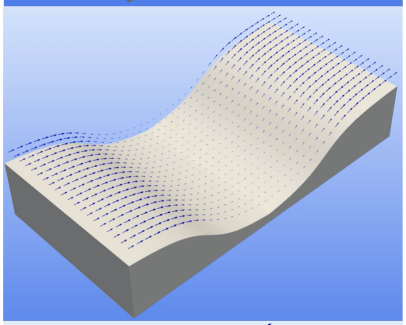
Upcan	$h = base + \left(\frac{\lvert y-160\rvert^{1.5}}{160^{1.5}}\right) \times base$ Note: The elevation at the outlet (right) end at the corners is 211 m, or roughly double the base topography elevation of 106 m at the centerline of the outlet.	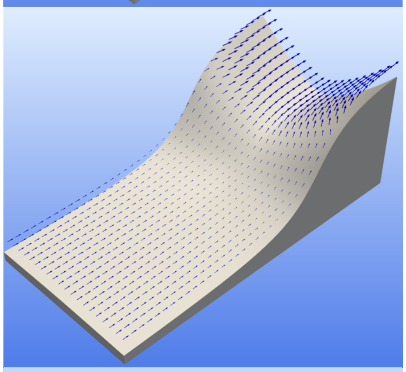
Ridge	$h = base - \left(\frac{\lvert y-160\rvert^{1.5}}{160^{1.5}}\right) \times base$ Note: The elevation at the outlet (right) end at the corners is 1 m, or 105 m below the base topography elevation of 106 m at the centerline of the outlet.	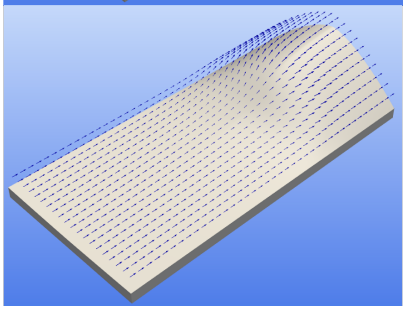

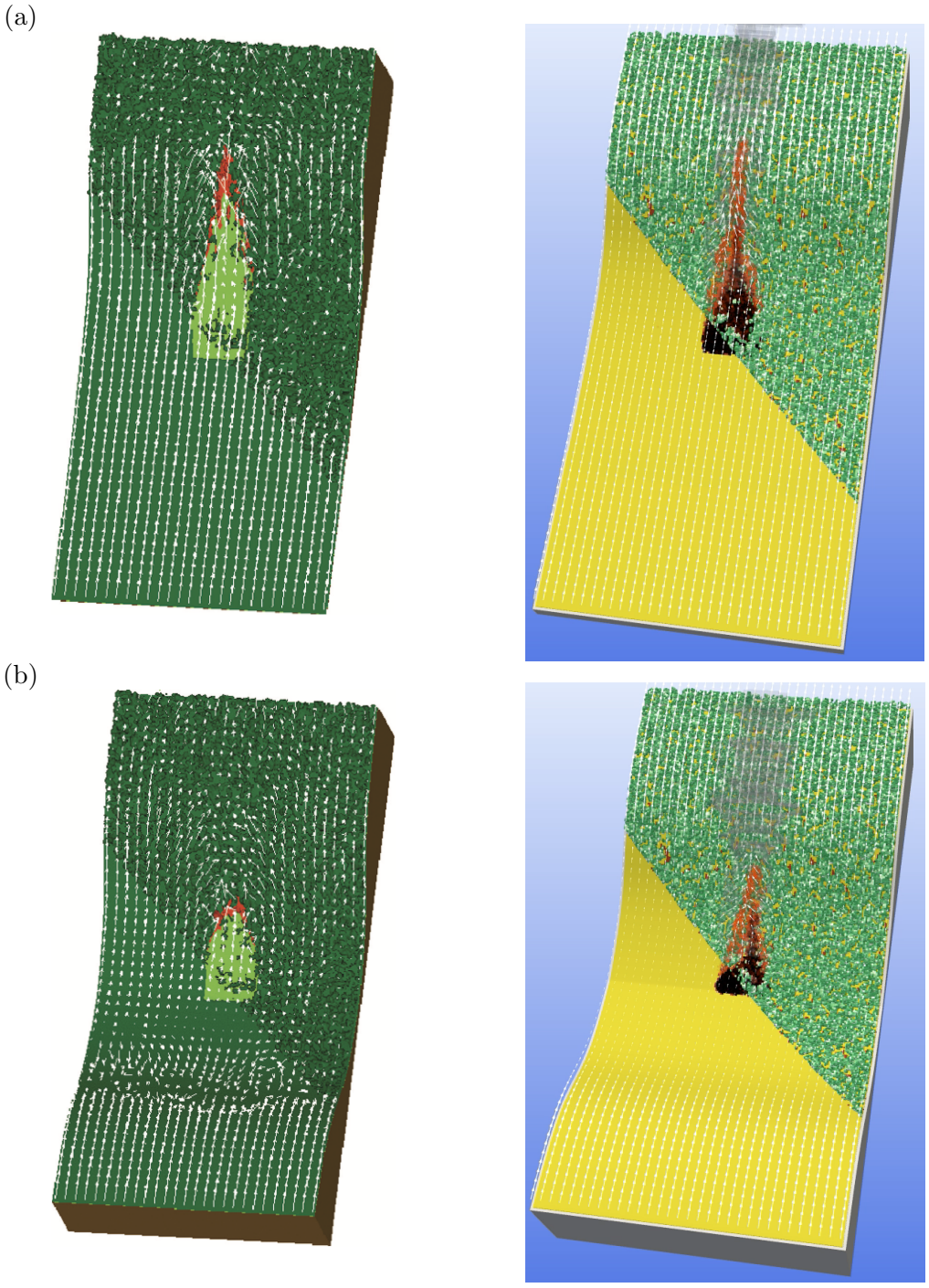

Figure 3.5: Snapshots of fire simulation states from FIRETEC (left) and QUIC-Fire (right). The top row (a) shows results from the Hill6 case and the bottom row (b) shows results from the Canyon6 case 150s after ignition. The FIRETEC snapshots are taken from [21]. Red isosurfaces in the left images indicate hot gases and red/orange in the right images are accumulated EPs in fuel cells that are landing in open air and generate buoyant updrafts. Dark, medium, and light green colors indicate locations of canopy fuel, tall grass, and depleted fuel in the left images whereas green, yellow and black indicate the same in the right images. White vectors represent winds near the top of the canopy fuel.

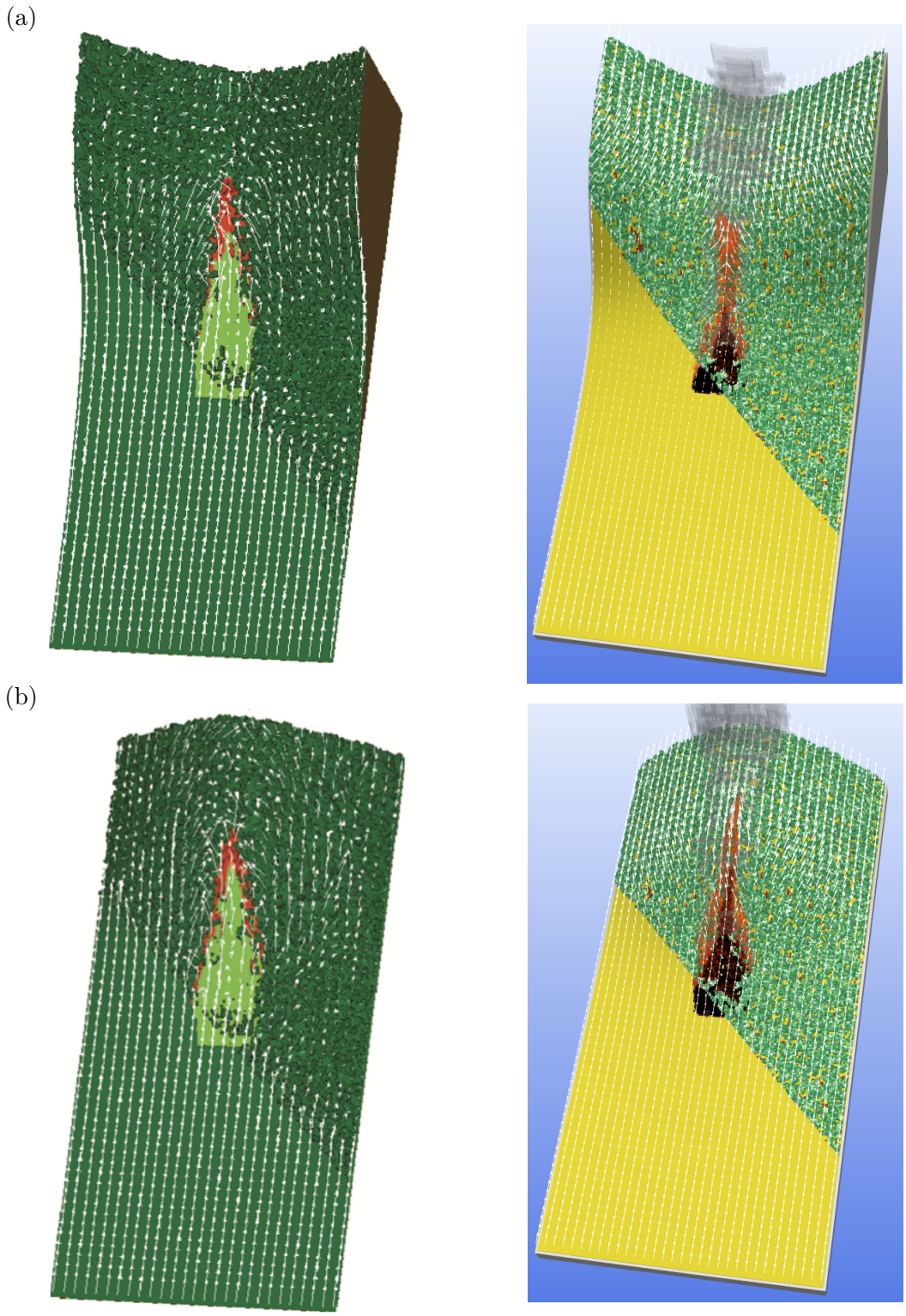

Figure 3.6: The same as Figure 3.5 but for the Upcan6 (top row (a)) and Ridge6 (bottom row (b)) cases. Results are shown at 150 s after ignition.

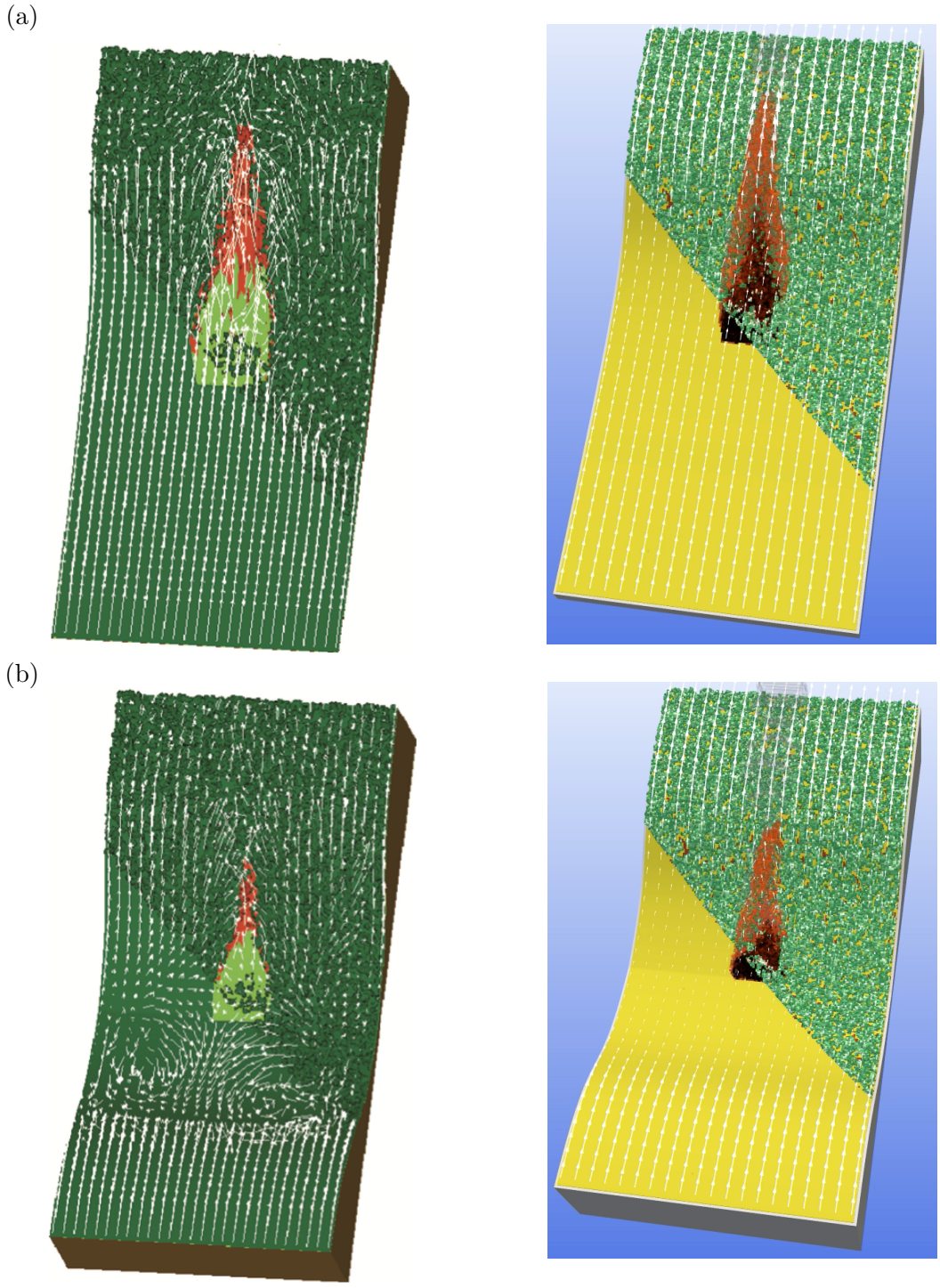

Figure 3.7: The same as Figure 3.5 but for the Hill12 (top row (a)) and Canyon12 (bottom row (b)) cases. Results are shown at 100 s after ignition.

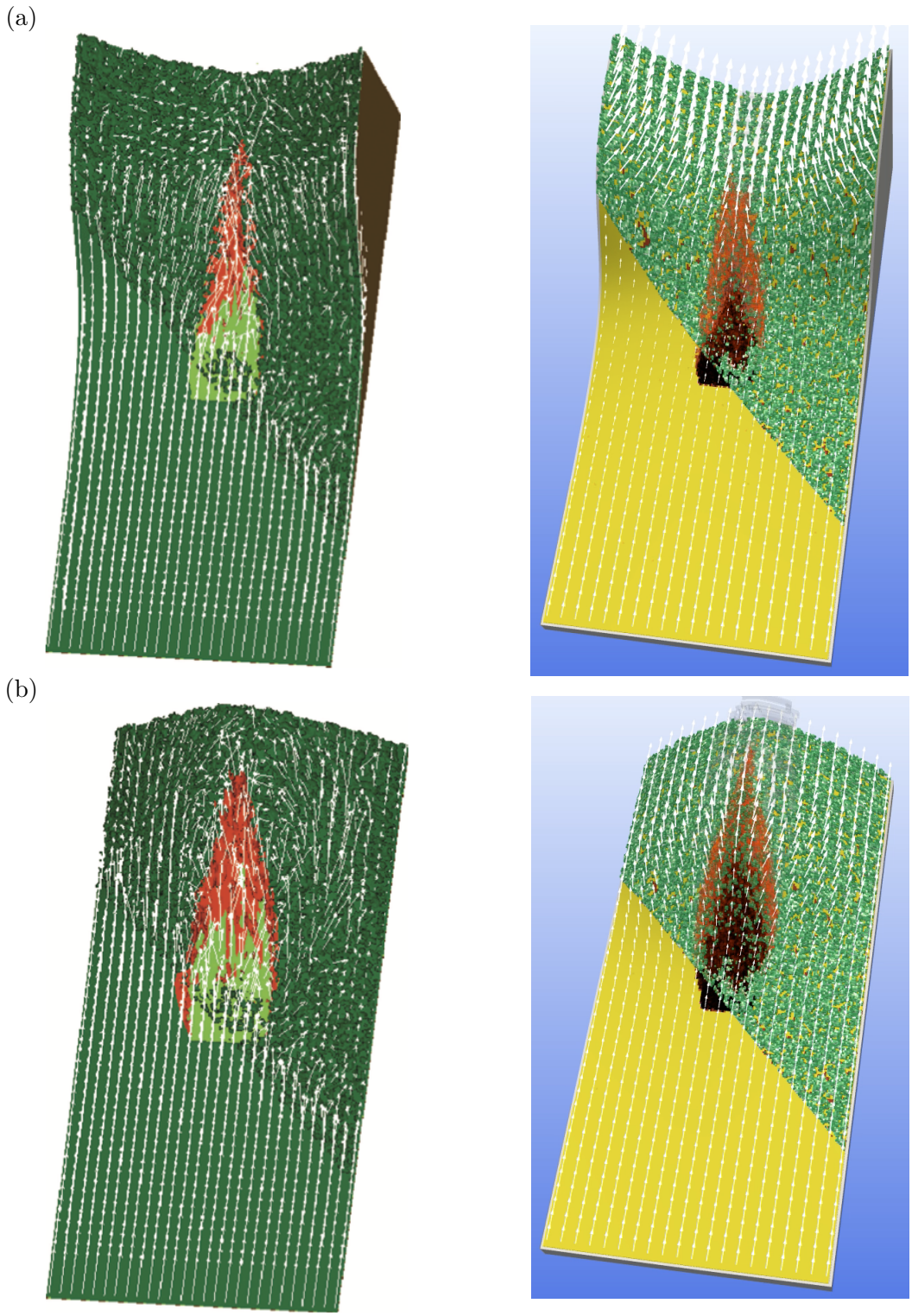

Figure 3.8: The same as Figure 3.5 but for the Upcan12 (top row (a)) and Ridge12 (bottom row (b)) cases. Results are shown at 100 s after ignition.

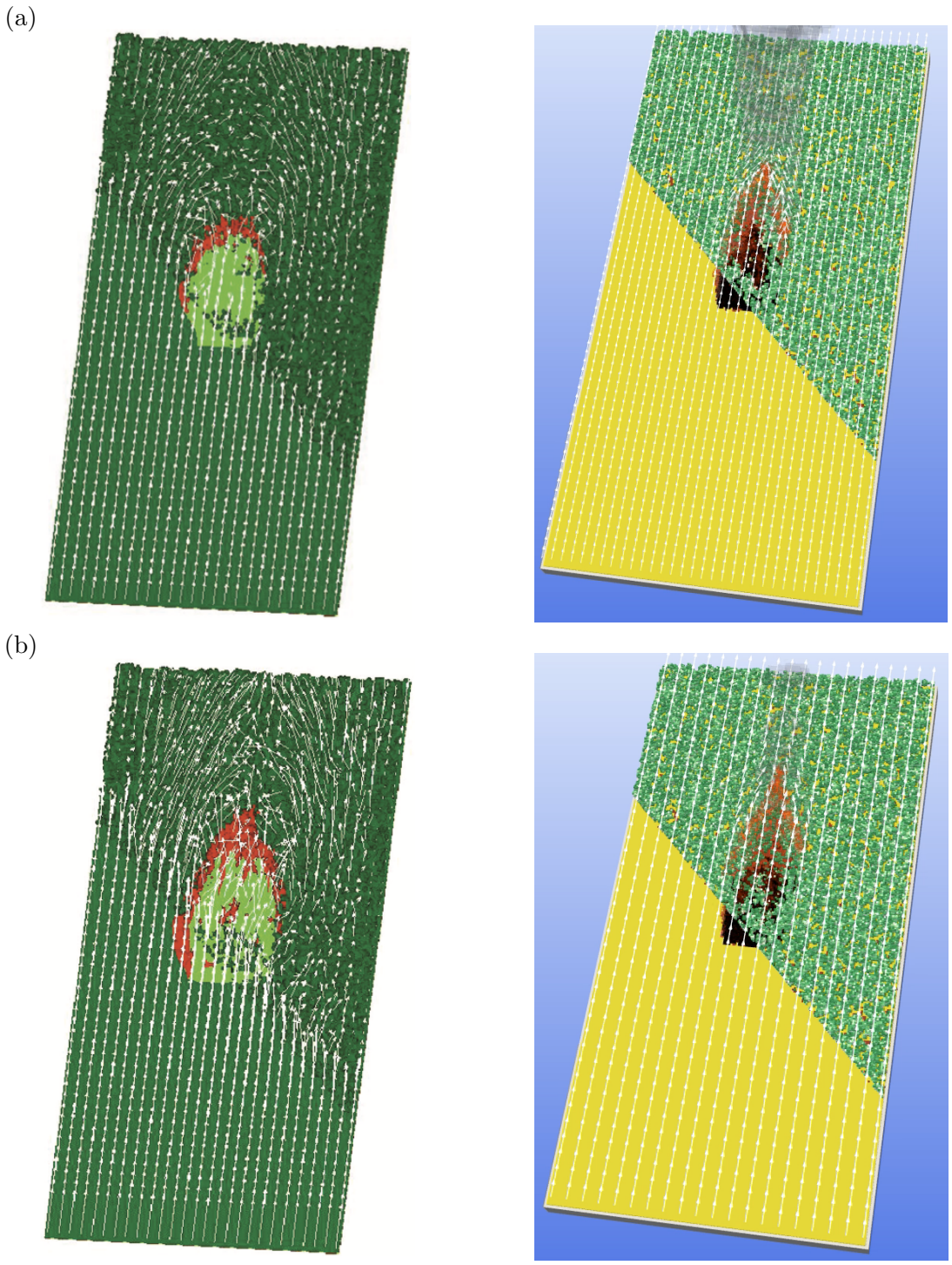

Figure 3.9: The same as Figure 3.5 but for the Flat6 (top row (a)) at 150 s after ignition and the Flat12 (bottom row (b)) case at 100 s after ignition.

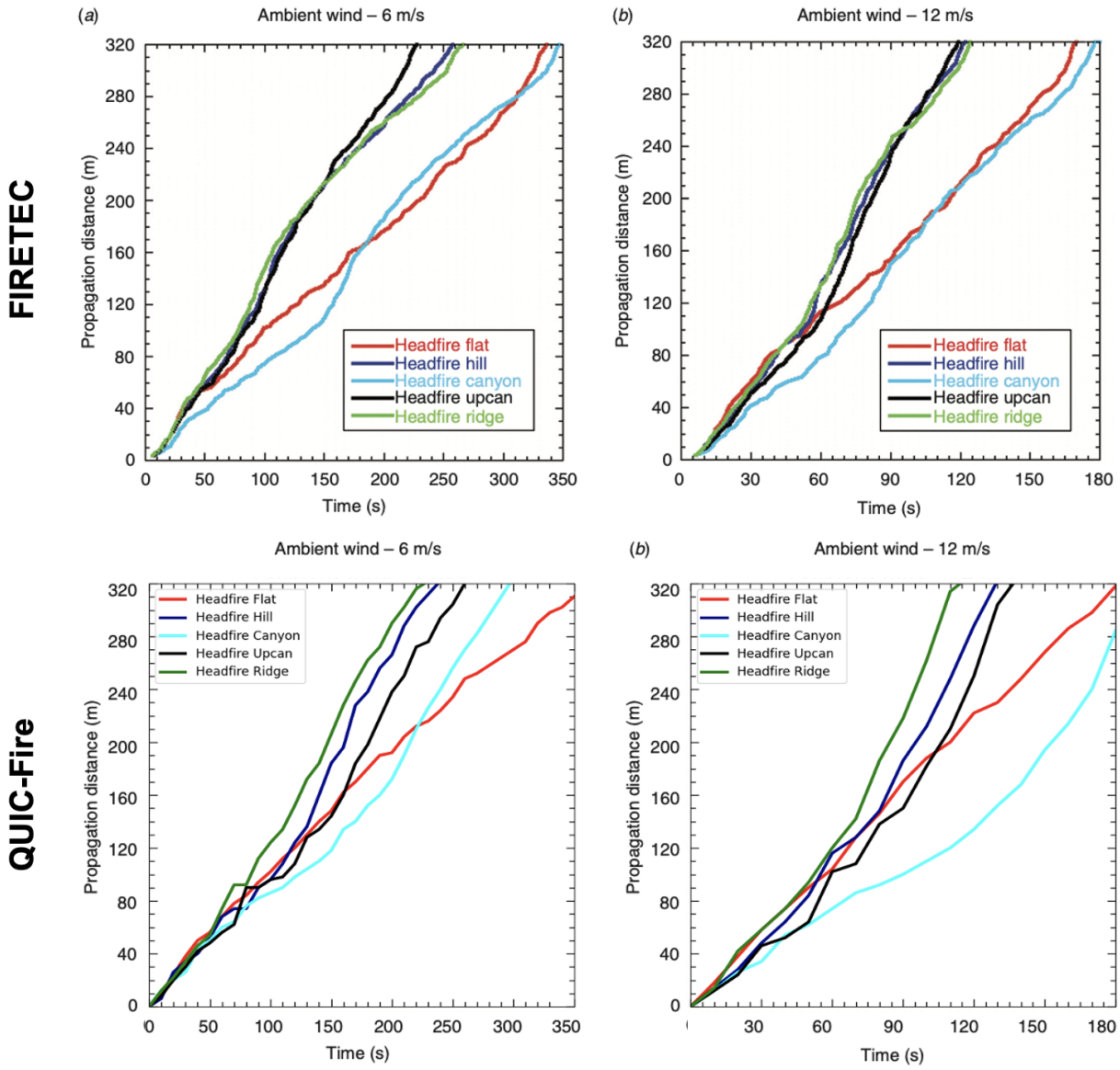

Figure 3.10: A comparison of fire propagation distances between FIRETEC (top, from [21]) and QUIC-Fire (bottom).

Table 3.2: Fire spread rates in selected regions of the computational domain for both FIRETEC and QUIC-Fire. Spread rate differences across Region 1 are characterized by slower rates from QUIC-Fire in the Hill12, Upcan12, and Ridge12 simulations. QUIC-Fire shows under-predicted spread rates across Region 2 and over-predicted rates across Region 3 when comparing with FIRETEC in non-flat cases.

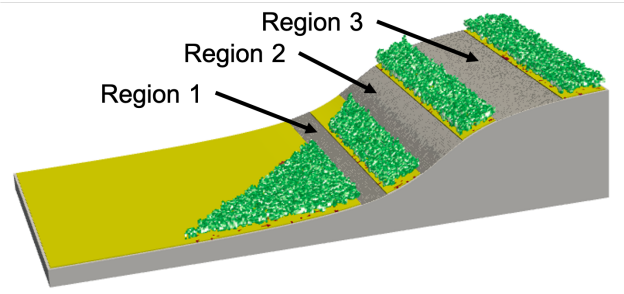

Spread rate within selected regions (ms^{-1})						
	Region 1		Region 2		Region 3	
	$40 \leq x \leq 70$ m		$110 \leq x \leq 160$ m		$200 \leq x \leq 280$ m	
Cases	FIRETEC	QUIC-Fire	FIRETEC	QUIC-Fire	FIRETEC	QUIC-Fire
Flat6	0.7	1.0	0.8	1.0	0.9	0.7
Hill6	1.1	1.3	2.1	1.7	1.0	1.8
Canyon6	0.7	0.8	1.9	1.0	0.8	1.5
Upcan6	1.0	0.9	2.1	1.3	1.3	1.6
Ridge6	1.3	1.3	2.3	1.4	0.9	1.7
Flat12	2.1	1.8	1.4	2.1	1.9	1.7
Hill12	2.3	1.8	3.8	2.0	2.9	3.5
Canyon12	1.1	1.3	2.8	1.4	1.6	3.1
Upcan12	1.8	1.2	4.0	2.2	3.4	4.2
Ridge12	2.3	1.6	3.4	2.8	2.1	4.2

Flat6 and Flat12 cases propagate at a fairly constant rate after the initial forming of the fire front after ignition. An interesting feature to point out that is seen in Figures 3.5-3.9 is the similar canopy fuel consumption pattern seen at the fuel interface. Just downwind of the ignition line in both FIRETEC and QUIC-Fire there is a lack of canopy consumption which is followed by substantial canopy consumption further downwind.

There are drastic differences between the propagation rates in the Hill and Canyon cases in QUIC-Fire even though they share identical downwind topographies. This shows that the effect of having an upwind topography feature is captured in the QUIC-Fire background wind field, seen by the slow spread rates at the beginning of the Canyon results. A similar slow starting spread is seen for Upcan in the QUIC-Fire results. This is due to the QUIC-Fire winds at the base of the hill being affected by the much larger elevation height of this case. The canyon sides work as a downwind obstruction that retards wind strengths more than in the hill case, reducing the strengths of winds where the ignition begins. Since there are no momentum effects in QUIC-Fire generated winds, there is no pulling effect generated from the channeled winds at the center of the Upcan case that would increase wind strengths along the centerline upwind of the canyon. This may be the cause of the earlier increase in spread rates in the FIRETEC results for the Upcan case but unfortunately it is impossible to confirm this as no wind data from the simulations are reported in [21].

Ridge6 and Ridge12 show the fastest spread rates in QUIC-Fire due to the reduced size of the downwind obstacle seen by QUIC-Fire. The cross-sectional area of the Ridge terrain, with respect to the background wind direction, is smallest when compared to the other nonzero terrains. This leads to stronger winds starting at the base of the ridge, as winds are stagnated less from not being obstructed, and increase in strength into the upslope region of the domain. These differences in wind can be seen by looking at the vectors overlaid on the topographies shown in Table 3.1.

Quantitative spread rates over three regions for each domain are in Table 3.2. The three spread rate observation regions are located at the base of the upslope portion (Region 1), across the steepest section of each topography (Region 2), and at the crest of the centerline where the slope levels off (Region 3). Two clear general and expected trends in the spread rates are that the Flat simulations are typically slower than all the other simulations and that spread rates increase between the 6 ms^{-1} and 12 ms^{-1} simulations. The propagation rates for Flat QUIC-Fire are similar to the FIRETEC results although there are variations in rates in both even though no terrain is present. This is not surprising since fire spread is a non-steady process. Average spread rates for

the two sets of results show an average spread rate of 0.8 ms^{-1} for FIRETEC and 0.9 ms^{-1} for QUIC-Fire in the Flat6 case and 1.8 ms^{-1} for FIRETEC and 1.9 ms^{-1} for QUIC-Fire in the Flat12 case. Averaging helps account for the stochasticity of QUIC-Fire and the fine-scale perturbations of FIRETEC. The similarity between rates shows a good basis point for comparing varying terrain driven behavior between the two codes.

3.5.2 Fire Spread Rates in Region 1

Region 1 is located 40-70 m downwind of the ignition line in an area at the base of the upslope region for all non-flat cases. Across the cases with topography, the Canyon and Upcan cases show the slowest spread rates in this region due to QUIC-Fire generating stagnant winds at the base of the slope. For the Canyon cases, this stagnation is driven by the upwind terrain acting as an obstacle while for the Upcan cases the stagnation is driven by the downwind feature being much larger than the other cases. In Region 1, QUIC-Fire spread rates are comparable with those from FIRETEC. The QUIC-Fire Upcan cases show slower spread rates than FIRETEC, likely because of flow channeling in FIRETEC (as described before). The Hill and Ridge cases show the fastest spread rates in this region for both QUIC-Fire and FIRETEC results.

3.5.3 Fire Spread Rates in Region 2

Region 2 is located 110-160 m downwind of the ignition line where slopes are steepest for all non-flat cases. For all QUIC-Fire cases, an increase in spread rates is seen between the Region 1 and Region 2 results. This increase in spread rate is consistent with the FIRETEC results although these increases (and thus resulting Region 2 spread rates) are significantly lower for QUIC-Fire. One possible source of this difference is the fact that FIRE-CA does not currently capture the fine-scale slope influences on flame tilt forward heat transfer associated with local entrainment imbalances. Experiments show that in low to no wind cases the flame tilt angle from vertical increases with slope and is correlated with an increase in spread rate [14, 55]. In some cases the flame attaches to the sloped surface. Without accounting for this factor, which will be accomplished through modifications to FIRE-CA and will be described in subsequent works, the forward heat transfer to unburned fuel and thus the influences of steep slopes are underestimated. This is further supported by results shown in Figure 3.11 where Pearson correlation r and p values are calculated for distributions of downwind spread rates against centerline elevation and centerline slope. These results show a strong positive correlation between spread rate and centerline elevation which is

expected as winds generated from QUIC-URB in Chapter 2 were characterized by increased wind strengths with increasing elevation. There is a weak negative correlation ($\mathcal{O}(\mathrm{p}) > 10^{-1}$) which show a lack of slope driven fire spread acceleration. If slope driven acceleration was captured, a strong positive correlation is expected. These results suggest the current implementation of FIRE-CA is not capturing the interaction between a flame at the surface and the sloped terrain, which is by design for this exploration, and that fire spread can be characterized as wind driven for these simulations. In this region, for both the 6 and 12 ms^{-1} winds, QUIC-Fire shows the fastest spread rate for the Ridge cases and the slowest for the Canyon cases. The Ridge cases show the fastest spread in this region as QUIC-Fire generates faster winds when compared to the other terrains due to the reduced profile of the Ridge terrain (and thus less blocking effect) at the y-extents of the domain.

3.5.4 Fire Spread Rates in Region 3

Region 3 is located 200-280 m downwind of the ignition line where the centerline slopes approach zero. This region shows an overall trend in non-flat cases where QUIC-Fire has greater spread rates than FIRETEC spread rates. The FIRETEC rates decrease from Region 2 to Region 3 which is believed to be caused by momentum driven effects creating turbulence and separations in the flow from the surface at the crest of the hill. This creates eddies and can even reverse flow near the surface that can stagnate fire spread [44]. QUIC-Fire currently cannot generate these flow separation features (this is a focus of future publications) in its wind field as there is no conservation of momentum in the solver. Instead the solver tends to generate increased wind speeds as elevations increase. This tendency is evidenced by all non-flat QUIC-Fire rates from Region 3 being greater than their Region 2 counterparts.

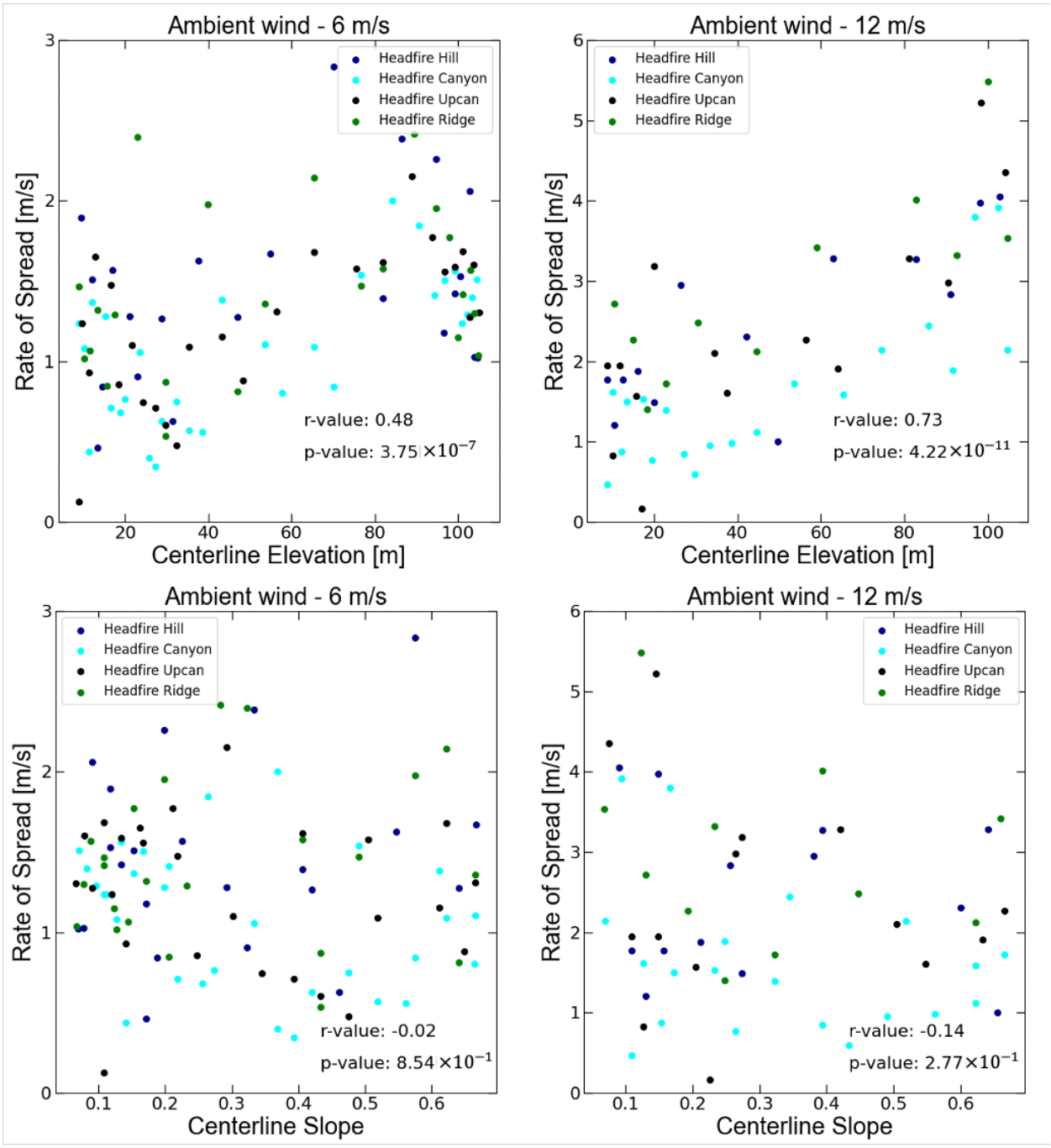

Figure 3.11: Distributions of downwind fire spread rates against centerline elevation (top) and centerline slope (bottom) for the 6 ms^{-1} (left) and 12 ms^{-1} (right) non-flat simulations. Pearson correlation r and p values are calculated and displayed in each corresponding plot. Correlation results show a strong positive correlation between rate of spread and elevation and a weak negative correlation between rate of spread and slope.

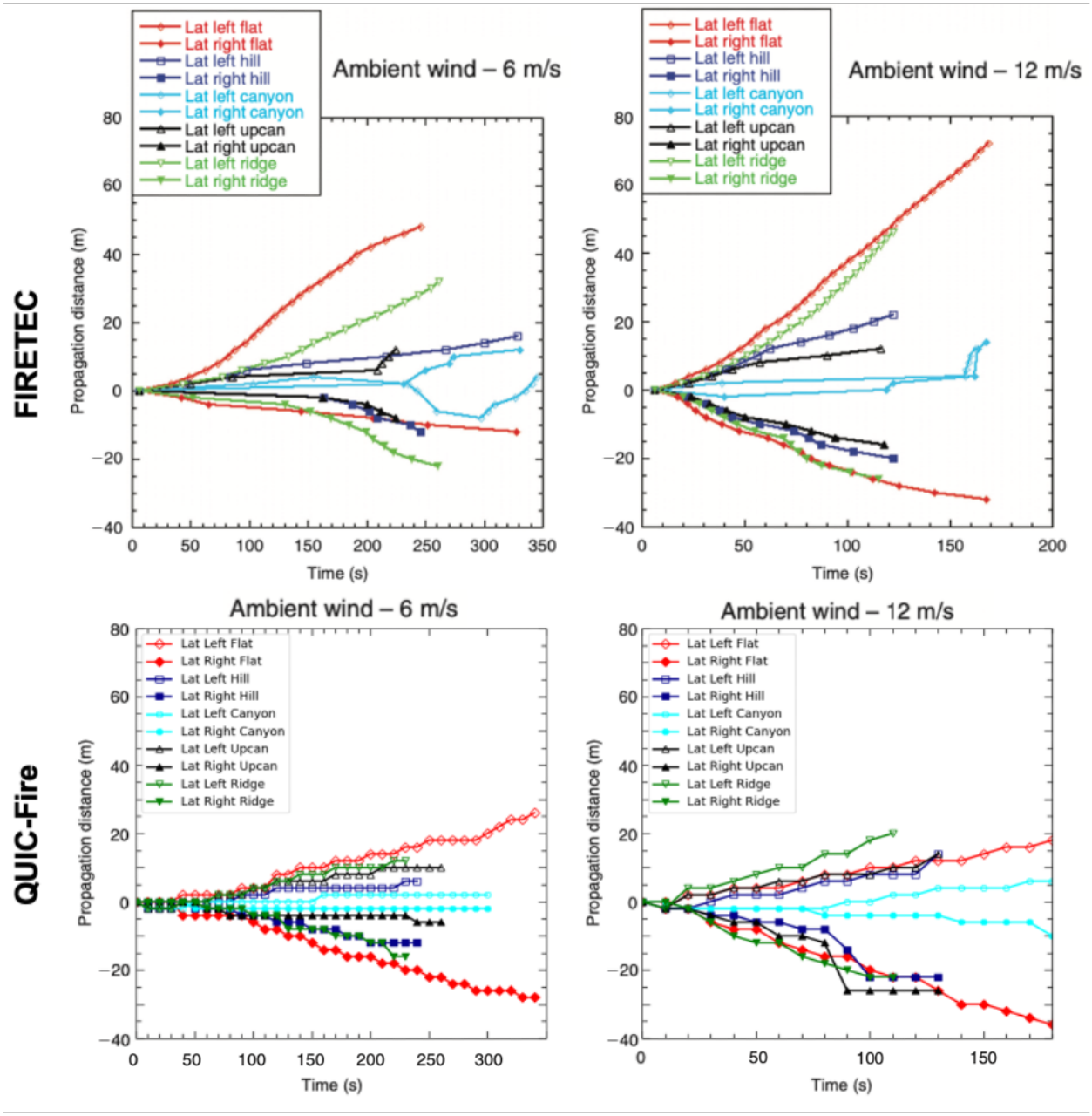

Figure 3.12: The fire lateral spread of FIRETEC and QUIC-Fire. The top two figures are taken from [21] and the figures below are generated using results from QUIC-Fire. Points on the FIRETEC plots are equispaced along the y-axis, i.e. points are only plotted if propagation distance is above a threshold, whereas points on the QUIC-Fire plots are equispaced in time.

3.5.5 Lateral Fire Spread

Figure 3.12 shows the lateral spread extent to the left and right of the initial ignition line of both FIRETEC and QUIC-Fire for the 6 and 12 ms^{-1} simulations. The left and right directions are in reference to the ambient wind direction where left is in the positive y-direction and right is in the negative y-direction. The left distance is calculated by the difference between the burning cell with the greatest y position and the top most cell position of the initial ignition line and the right distance is calculated using the burning cell with the lowest y position and the bottom most cell y position of the initial ignition. For example, positive values for the 'left' spread represent lateral growth along the left flank of the headfire whereas negative 'right' values show growth along the right flank. The two curves for each case in Figure 3.12 show how the width of the burning region is evolving through a simulation. Lateral spread results show a couple of general trends when comparing QUIC-Fire results to FIRETEC results. One obvious trend is that FIRETEC shows much greater lateral spread, about a factor of two, but almost exclusively on the left side. One contributing factor to the larger lateral spread in FIRETEC, is that it resolves a more significant effect of the asymmetrical diagonal fuel interface (between the flat grass and forested regions) on the wind field where winds at the interface align with the fuel interface. This alignment of the winds causes the portion of the initial ignition line to immediately spread laterally in the left direction in FIRETEC, while it does not in QUIC-Fire. Also, due to the fire consuming the majority of the canopy in these fuels, the fire at the left flank is mostly being fed by winds coming from the open grass region unlike the right flank of the fire, which always has a forested section obstructing winds upwind of the fire. The simplified drag model in QUIC-Fire, which is also a topic of ongoing improvement, is only a local approximation where winds are sped up as fuel is consumed, but no effects from downwind or upwind vegetation are realized in the flow fields. Due to this current way of handling the attenuation of winds by vegetation in QUIC-Fire, the winds at the interface are not as strongly diverted leftward. Moreover, in QUIC-Fire the turbulence approximation is based on a local wind shear calculation that is increased in cells where nearby fuel cells contain consumed and unconsumed canopy fuels. This is due to the way winds are linearly interpolated between the Cionco profile and background winds as fuels are depleted [8, 20]. This causes the stochastic component of EP travel to be a larger factor in the direction realized, leading to more flanking spread occurring on the right side in the QUIC-Fire simulations.

When looking past the effects of the diagonal leading edge of the vegetation, the overall trend in lateral spread behavior is similar between QUIC-Fire and FIRETEC. In the 6 ms^{-1} results, the Flat6 and Ridge6 have the greatest lateral spread while the Canyon6 case show minimal lateral spread. Hill6 and Upcan6 fall in between. The lack of lateral spread in the Canyon6 case is due to the indrafts generated by the buoyant plumes dominating the slower low elevation wind velocities at the base of the canyon, drawing in the flanks of the fire and restricting outward spread. These plume-dominated winds degrade as the fire propagates up the canyon and begins to experience stronger winds, where it then broadens slightly. This effect can also be seen in the Canyon12 results. The Hill6 and Upcan6 cases show less lateral spread in the left direction than the Ridge6 and Flat6 cases where stronger background winds lessen the indraft dominance seen in the Canyon6 case but still appears present. Slightly less spread than the Ridge6 case in the right direction is seen for the Hill6 and Upcan6 cases and the similarity of results is due to the turbulence/drag model interaction described above.

The 12 ms^{-1} results for QUIC-Fire show a few outliers from the FIRETEC simulations. The Flat12 lateral spread on the left side is not greater than the Ridge12 spread and is also a third of the lateral spread seen in the FIRETEC results. However, the right spread is similar in extent and profile to the Ridge12 right spread. This shows that flanking behavior under strong winds is underrepresented by the code and is seen in a majority of the lateral spread results seen for QUIC-Fire compared with results from FIRETEC. One contributing factor to this systemically lower lateral spread in QUIC-Fire compared to the FIRETEC simulations is that FIRETEC explicitly represents the interaction between the winds and the forest canopy. The lateral components of the variations or turbulence in the wind fields contribute significantly to the lateral spread in FIRETEC simulations. However, the current canopy representation served to suppress the wind and turbulence, and does not induce as significant of lateral components that drive the lateral spread. The sudden growth seen in the right spread of the Hill12 and Upcan12 simulations happens when the fire is traversing Region 2. This increase may be due to a sudden intensity increase driven by winds strengthening and pushing strong buoyant plumes ahead of the fire promoting rapid fire spread. The Upcan case also has the added factor that slope gradients tend to the y boundaries, promoting fire spread in those directions. The Canyon12 case shows similar behavior to the Canyon6 case where lateral spread restricted by indrafts, although some lateral spread occurs at 70 s into the simulation. This time coincides with the slowdown in spread rate seen in Figure 3.10 which suggests that lower wind speeds are present where the fire is burning at this time. Lower local wind speeds

Table 3.3: Lateral spread rates measured from the extents of the initial ignition line edges for simulations ran by both FIRETEC and QUIC-Fire.

	Left extent lateral spread rate (ms $^{-1}$)		Right extent lateral spread rate (ms $^{-1}$)	
Simulation	FIRETEC	QUIC-Fire	FIRETEC	QUIC-Fire
Flat6	0.22	0.076	-0.036	-0.082
Hill6	0.058	0.025	-0.013	-0.05
Canyon6	0.026	0.007	0.001	-0.007
Upcan6	0.039	0.023	-0.013	-0.038
Ridge6	0.086	0.052	-0.037	-0.070
Flat12	0.46	0.10	-0.29	-0.20
Hill12	0.23	0.107	-0.18	-0.169
Canyon12	0.024	0.032	0.027	-0.053
Upcan12	0.14	0.108	-0.15	-0.20
Ridge12	0.47	0.182	-0.25	-0.20

promote flanking spread as turbulent contributions to EP travel direction become comparable to the ambient wind's directional influence.

Table 3.5.5 shows average rates of lateral spreads for both FIRETEC and QUIC-Fire results. The rates shown in this table show the trend discussed above where lateral spread in the left direction is much less in the QUIC-Fire results when compared to the FIRETEC results. With the spread in the right direction being more comparable to the FIRETEC results shows that the solution for the lacking left lateral spread is not a simple scaling of the turbulence. A more sophisticated drag model is more likely the remedy for the lacking growth of flanks at the fuel interface.

3.6 Conclusions

A total of 10 simulations using QUIC-Fire are compared to FIRETEC simulation results over identical inhomogenous topography, which had sections of steep slopes, and 3D fuels with the same landscape-level fuel characteristics. These cases are aimed at investigating the influences of topography on fire behavior while also keeping similarities between topographies to separate different terrain effects on fire behavior. An idealised hill formed the base topography that the other topographies are derived from. The other topographies consisted of the base hill where lateral gradients are increased and results in a downwind canyon-like feature parallel to the ambient wind direction, the base hill with decreased lateral gradients resulting in a ridge, and the base hill with an identical base hill reflected about the ignition line creating a canyon oriented perpendicular to the ambient wind direction. The modifications made to the base hill kept the centerline profile of

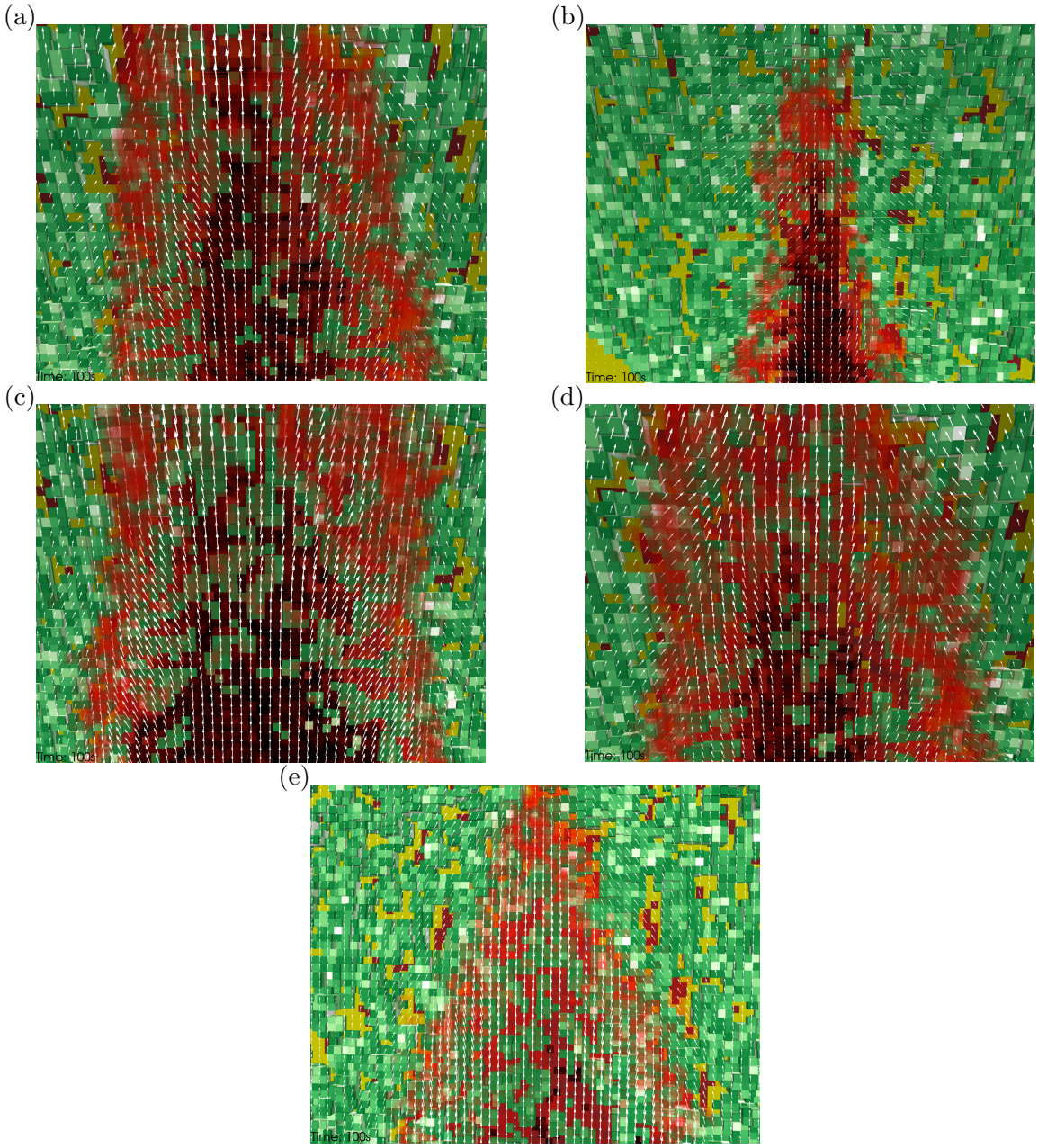

Figure 3.13: Snapshots of fire simulation states of QUIC-Fire simulations showing near-surface wind-vectors for the (a) Hill12, (b) Canyon12, (c) Ridge12, (d) Upcan12, and (e) Flat12 cases. Camera positions are roughly in the same position for (a), (b), (c), and (d) above the Region 2 section and the camera position for (e) is slightly downwind to show wind vectors nearer to the head of the fire. These figures show the 2 m resolution winds in their entirety. Quivers are scaled to 45% of their actual length.

the terrains downwind of the ignition identical. These topographies form a variety of topographic features to evaluate the validity of the QUIC-Fire wind solver coupled with the FIRE-CA fire spread algorithm. Two ambient wind speeds, 6 and 12 ms^{-1}, are used to generate background wind fields that show the influence of terrain on these fields. Results from these simulations are compared with results reported from the more detailed CFD-based FIRETEC code by computing the same metrics and looking at effects these topographies had on fire shapes and their growth. QUIC-Fire shows similar overall fire behavior when compared to FIRETEC results in regard to the narrowing of fire shape in the Canyon, Hill, and Upcanyon cases and the overall trends in spread rates across all topographies simulated. The comparison is seen as a success as QUIC-Fire is competing with a code that is fully physical and taking timesteps that are one-hundredth the size. Further work is needed, but QUIC-Fire is a needed contribution for simulating wildland fire behavior using readily available computational resources.

Results between QUIC-Fire and FIRETEC highlight three places where the QUIC-Fire code could use attention. From results shown in Figure 3.10 and Table 3.2, it can be seen that QUIC-Fire has similar average spread rates to FIRETEC but does not capture some of the nuances seen in the FIRETEC results. Specifically, spread rates in QUIC-Fire results tend to show less sensitivity to the position on the topography compared to the FIRETEC results, which show more obvious increases and decreases to spread rates depending on the local slope and the non-local wind effects. QUIC-Fire shows slower spread rates, compared to FIRETEC results, in the region of these topographies with the strongest terrain gradients which could be helped by making modifications to the flame-angle portion of the FIRE-CA algorithm. Improving the way QUIC-Fire accounts for flame tilting due to local topography-influenced wind conditions and its orientation with respect to the terrain surface can have substantial effects on fire behavior on varying slopes and wind conditions [47, 55]. Fire-CA does account for tilt angle but bifurcates the behavior between lofting and travelling along the surface. The purpose of this comparison to FIRETEC is to examine the influence of the TF wind on QUIC-Fires fire spread, so flame tilt modifications to FIRE-CA are not implemented but are planned for subsequent publications. Another shortcoming observed in the results is the continued fast fire spread as the slopes reduced near the top of the hill compared with the retardation of fire spread seen in FIRETEC near the top of the hill when the slopes diminished and the flow began to separate. This is mostly driven by momentum effects in the wind field as the flow separates from the surface and creates eddies and recirculations that tend to stagnate fire behavior as winds in these regions can reverse direction from the ambient wind. QUIC-Fire has

no incorporation of momentum in its wind field solutions so in its current state it is impossible to capture these dynamics. Work is planned to map the wake-eddy parameterizations from [33] designed for urban environments to the QUIC-Fire solver to capture this behavior. The last place where QUIC-Fire does not capture fire dynamics ideally is in flanking fire behavior. The FIRETEC results showed that winds near the fuel interface between grass and forested regions aligned with the interface, promoting fire growth at the left flank of the fire. The current drag model implemented in QUIC-Fire is a local approximation and includes no information from the upwind and downwind directions. Updating the drag model to incorporate this nonlocal information would help FIRE-CA fire behavior at these fuel interfaces and also change dynamics when fuel upwind of a burning cell has already been consumed, increasing incoming wind speeds and increasing fire intensity. These changes require careful thought in implementation due to the desire to retain the computational speed of QUIC-Fire and may require novel solutions.

Acknowledgements

Images from [21] shown in Figures 3.5 through 3.12 are used with permission of CSIRO Publishing, from "Coupled influences of topography and wind on wildland fire behaviour", Rodman Linn et al., International Journal of Wildland Fire 16.2 (2007); permission conveyed through Copyright Clearance Center, Inc.

CHAPTER 4

ANALYSIS OF SAVING LAGRANGE MULTIPLIERS

4.1 Modified SOR Effects on Fire Phenomenology

The objective of the change described in section 1.4 is to improve fire-fire interaction. With the original SOR algorithm the convective pull that separate fires exert on each other will be missing. This fire-fire interaction is an essential part of prescribed fire strategy [30] so it is essential that QUIC-FIRE captures these dynamics. Qualitative comparison will be done in this section of what changes in fire behavior are observed in the model when using the modified SOR algorithm.

4.1.1 Head Fires

A head fire is canonical fire phenomenology that any fire model should be able to capture. A head fire is produced when background wind blows perpendicular to a flame front. An acceleration in fire spread is initially seen following the direction of the wind. As the fire intensifies in this direction so do the buoyant plumes generated, intensifying the indrafts. The wind strength becomes strongest at the center of the affected fireline and the center begins spreading faster than the rest of the line. This greater itensity at the center also orients the windfield as though a strong sink is located at the center. This orients the wind field at the extents of the line, the 'flanks', along the direction of the line and restricts the outward growth of the line at the flanks. The result of all of this is a parabolic shape that holds its shape as it continues to spread in the direction of the background wind [7].

A comparison between the original and modified version of the SOR and its effects on a head fire simulation is conducted. This is to ensure that this fire behavior is preserved when using the new initial guess for SOR. The fire scenario for these cases is a 100 m long fireline is ignited at x=50 m and is centered in the y-direction. A 3 ms^{-1} background wind blows in the positive x-direction, perpendicular to the fireline. From the results in Figure 4.1 it is clear to see that no significant change in fire behavior is observed and the head fire develops in the same manner in both simulations. Both versions develop the expected parabolic shape and spread the same distances. Also, no discernable differences in backing fire spread rate is observed.

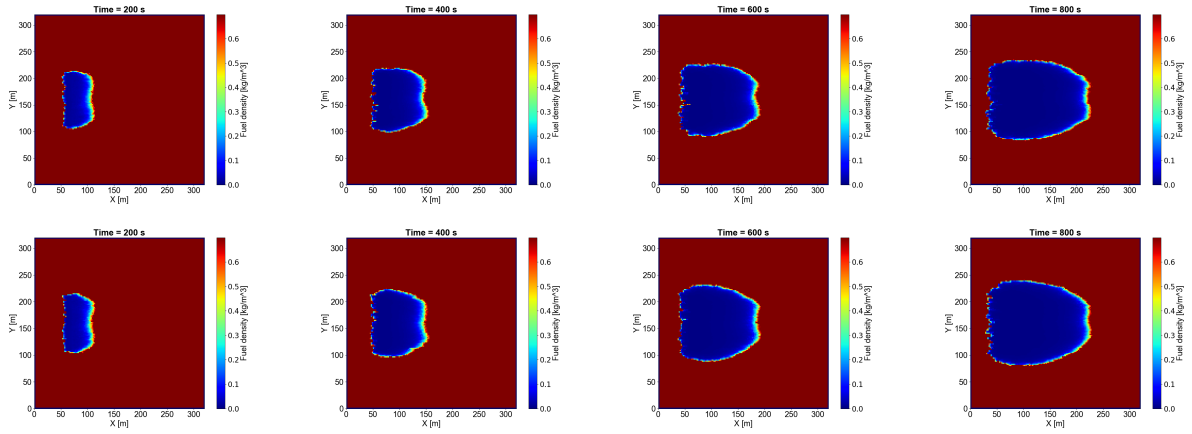

Figure 4.1: Snapshots of two simulations showing the development of a head fire for both versions of the SOR algorithm. The top row shows results from the original SOR algorithm and the bottom row shows results from the modified version.

4.1.2 Testing Fire-Fire Interaction

Four tests are explored in this section to explore whether the range of fire-fire interactions is extended by using λ_{prev} as the initial guess for the SOR algorithm. Not only is it important that fires can influence the development of other fires but the resulting phenomenology produced must also agree with what practitioners observe in the field. The initial ignitions of the four tests are shown in Figure 4.4. Tests (a), (b), and (d) are not only constructed to demonstrate the increased fire-fire interaction but are also typical occurrences in prescribed fire situations. In (a) two 200 meter long, 10 meters thick, line fires are initialized with no background wind and a gap of 40 meters between the two lines. Test case (a) examines how two firelines interact with each other in a no wind scenario between the two algorithms. In case (b) two 100 meter long line fires are generated near the bottom of the domain with a background wind of 3 ms^{-1} in the positive y-direction. Test case (b) is to test how two line fires will draw together with a background wind alligned with the long side of the two line fires. Test case (c) consists of four 40 meter diameter spot fires centered on the corners of a 100 meter square. This test is to clearly illustrate the fire-fire interaction introduced by the change discussed in Section 1.4. In case (d) two 200 meter long firelines are initialized on the left side of the domain with a background wind of 3 ms^{-1} in the positive x-direction. This configurations tests if having plume structures upwind of a headfire, generated by the upwind fireline, will restrain the growth of the downwind headfire with the new initial guess for λ.

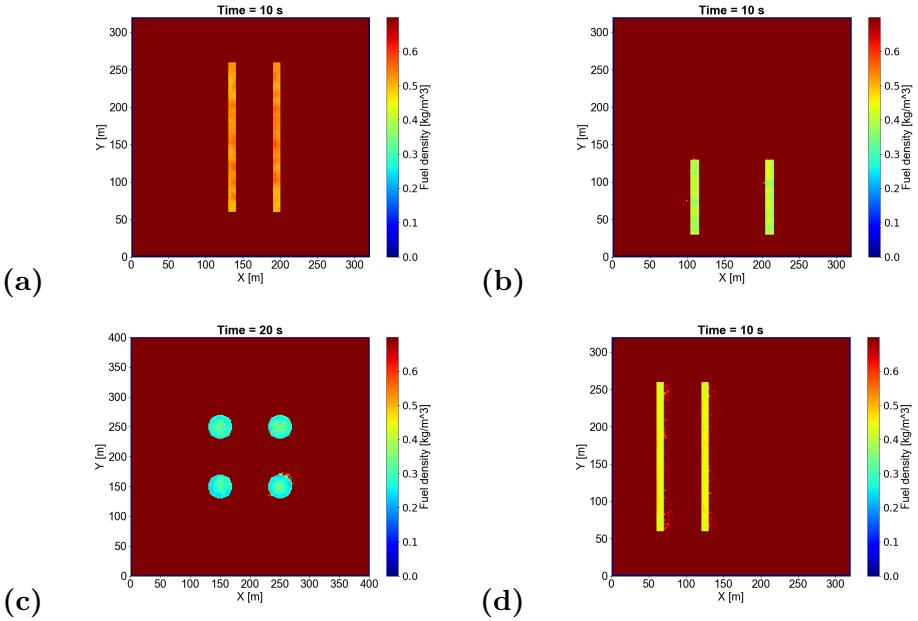

Figure 4.2: Initial conditions of fire simulations described in Section 4.1.2 used for investigating differences in fire behavior driven by the different initial guesses of λ.

The results from test (a) are shown in Figure 4.3 and show the increased interaction between the two fire lines resulting from using λ_{prev}. The two fire lines 'pull' on each other and have increased spread in the direction of the other fire. The run using the initial guess of $\lambda = 0$ shows mostly uniform creeping fire growth in all directions. There is noticeably more asymmetrical growth in each individual fireline produced from the modified version 150 seconds into the simulation. The second row of Figure 4.3 shows different resulting fire propagation in the region between the two lines. The two fire perimeters in the simulation that uses λ_{prev} draw closer together by 300 seconds. The same mutual draw seen in test (a) is further demonstrated in the results from test (b) in Figure 4.4. The line fires in test (b) with wind fields generated using λ_{prev} (second row of Figure 4.4) draw together as they spread in the positive y-direction. As the two lines come together at an angle they transition into a 'jump fire' which results in a zippering effect shown experimentally in [51] and computationally in [48]. At 250 seconds into the simulation using the modified SOR windfields the two firelines are drawn together whereas the original version spreads almost exclusively in the y-direction. The two firelines from the modified SOR merge at a much earlier time, about 200 s earlier, than the unmodified version. In the unmodified version the two firelines grow steadily towards eachother along the entire length of the firelines. This leads to a large collapse between the two firelines at 730 seconds into the simulation which results in two very different evolutions of

the fire but a similar final fire boundary seen at 1,000 seconds. As predicted the firelines using the original SOR show almost no fire-fire interaction until the two lines spread within 20 cells of each other and collapse.

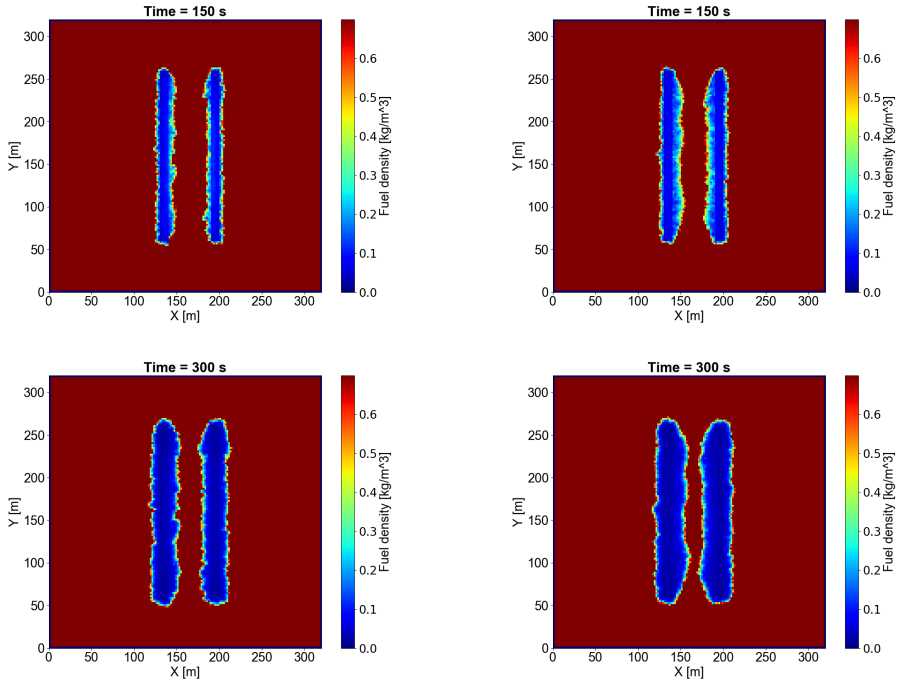

Figure 4.3: Snapshots of fuel density from test case (a) in Figure 4.4 at 150 seconds and 300 seconds into the simulations. The left column is the original algorithm and the right column is using the modified SOR algorithm.

Results from test (c), shown in Figure 4.5, show the starkest difference in fire dynamics between the two SOR wind fields. The original SOR results show only creeping spread in the spot fires, showing no atmosphere effects from the other fires. The original algorithm results only show creeping spread with the spots grow evenly in the radial direction, evidenced by the rough fire boundary that develops. However, when using λ_{prev} the spot fires interact and pull together toward the center of the domain. This draw to the center is caused by the large indrafts generated by the large 40 meter diameter fires. The modified version results show that these indrafts extend to the other spot fires and resulting in a net spread towards the center. The difference between the two sets of results show that fire-fire interactions can occur over much greater distances when using the modified SOR solver. This is an extreme example but certainly shows the what using λ_{prev} as the initial guess achieves over the original.

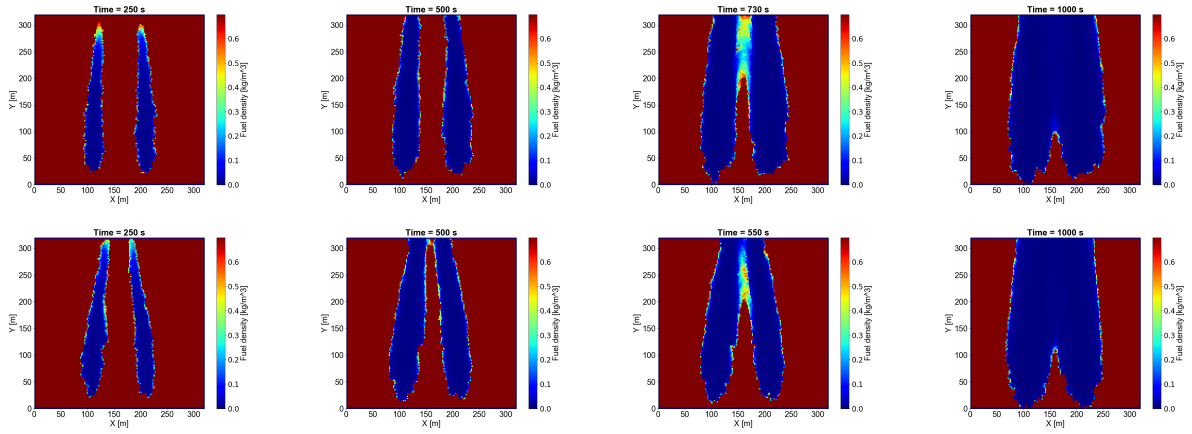

Figure 4.4: Results for test case (b) with initial configuration shown in Figure . The top row shows of snapshots of fuel density from the original SOR algorithm and the bottom row showing snapshots from the modified version. It is important to notice that the third column are snapshots at different times showing the transition to a 'jump' fire occurs at different times.

The results shown for test (d) in Figure 4.6 show a less drastic difference than test (c) did but still have significance. In the modified SOR results 50 seconds into the simulation the upwind fireline spreads slightly farther than the downwind line whereas the results from the original algorithm show near identical spread patterns between the two lines. Comparing snapshots 100 seconds into the simulations it can be seen that the spread of the downwind fireline near the flank edges is restrained when using the modified SOR wind field. In the unmodified version two head fires develop near both flank edges on the downwind fireline like the results seen in Figure 4.1. This would be expected in an actual fire as the upwind plume structure would obstruct wind flow, reducing the wind speeds at the location of the downwind fire line. The last snapshot shown 300 seconds into the simulation shows no major difference between the two methods although a slightly flatter fire front is seen in the modified version. The final spread distance between the two methods is nearly identical.

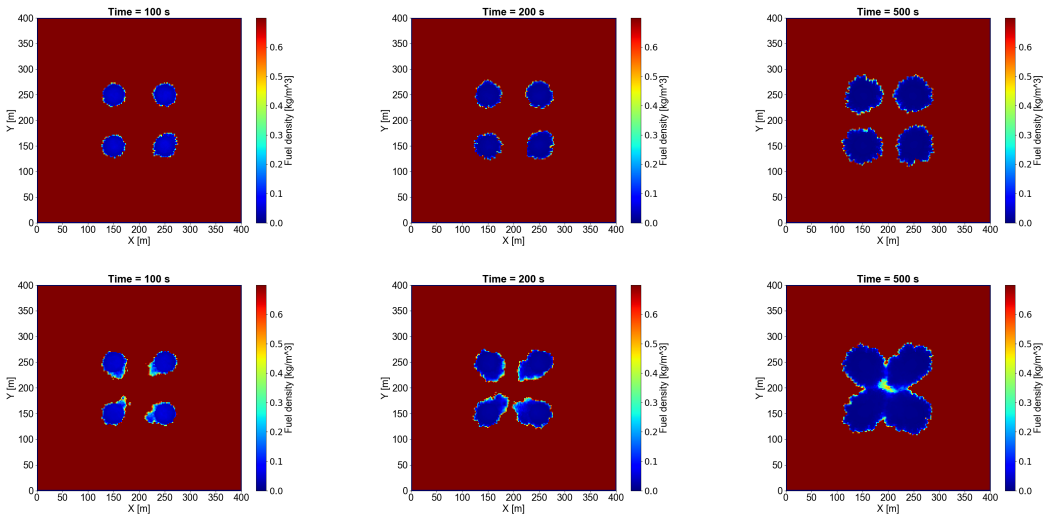

Figure 4.5: Snapshots of fuel density from test case (c). The top row shows results from the original SOR version and the bottom row showing results from the modified version.

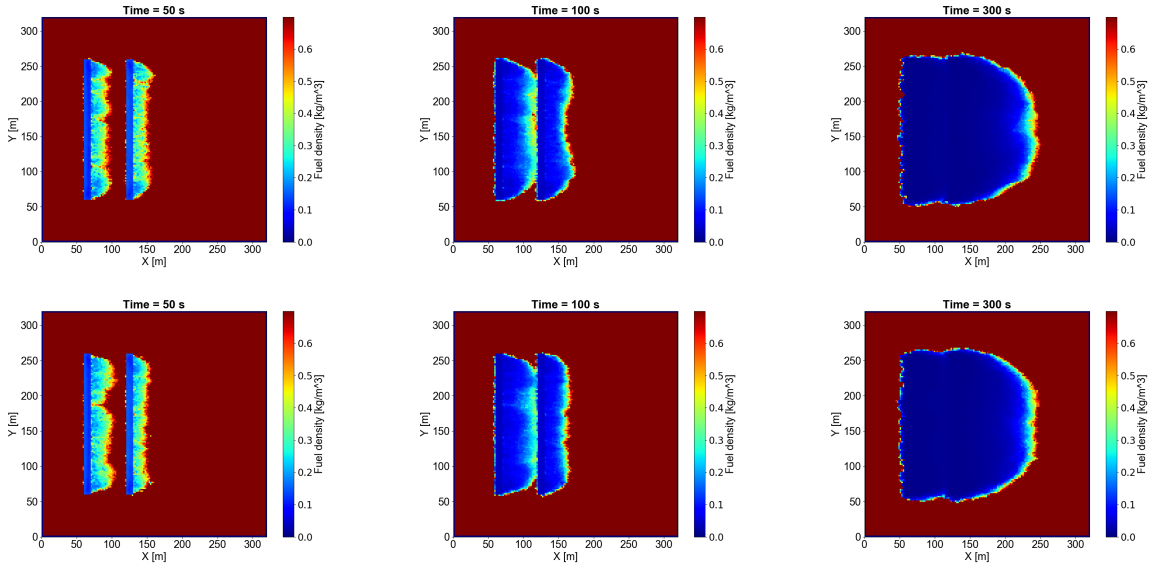

Figure 4.6: Snapshots of fuel density from test case (d). The top row shows results from the original algorithm and the bottom row shows results from the modified SOR algorithm.

4.1.3 Ring Fires

Ring fires, similar to the center fire shown in Figure 1.5, are fire geometries that are utilized only in very specific fire scenarios. They are characterized in [30] as generating 'high intensity,

rapid burnout' fires that generate a strong indraft that 'draws fire away from surrounding fuels.' In this section the effects from using λ_{prev} as the initial guess in ring fire scenarios with no background wind is explored. As seen from the tests in Section 4.1.2 fire-fire interactions are strengthened by this change and much more non-local effects are captured. Simulation runs for three different ring fires of different diameters for both SOR initial guesses are compared. The ignition patterns and sizes are described in Figure 4.7.

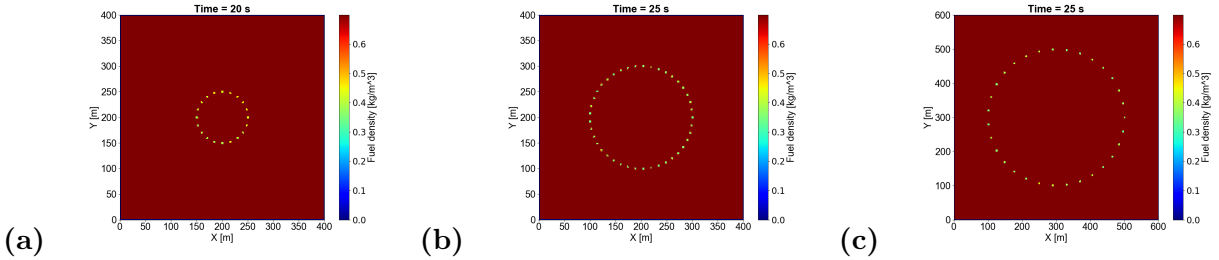

Figure 4.7: Initial conditions for three different ring fire tests. The diameters for the rings are 100, 200, and 400 meters for (a), (b), and (c) respectively. The ignition spots in (a) and (b) are spaced 20 meters apart with a diameter of 4 meters. The ignition spots in ring (c) are spaced 45 meters apart and have a diameter of 6 meters. Notice the domain for (c) is 50 percent larger than (a) and (b). All ring fire simulations have a background wind speed of 0 ms^{-1}.

Results from the simulations show dramatic differences between the original SOR results and the modified version(Figures 4.8 and 4.9 respectively). Results from the original solver show very little acceleration in the spread at all scales and all of the original solver simulations can be characterized as creeping spread. Using λ_{prev} as the initial guess shows dramatic changes in the simulation results as the ring fires collapse rapidly inward as described in [30]. For the large ring simulation the acceleration of inward spread is not seen until the inner diameter is about 250 meters. This agrees with [51] that spread increases can be a curvature driven phenomenon. Since there is so little curvature in the large ring the fire behaves similarly to a line fire with no wind. As the inner ring grows smaller in radius the curvature of the fireline increases and acceleration in the spread rate is seen. Quantitative measures of spread rates for ring fires are not readily available which limits this analysis to qualitative analysis, although, there seems to be a relationship between the diameter of the ring fire and the inward rate of spread. The outward rate of spread between the two SOR routines appears to be identical. Fire acceleration is seen in all of the modified SOR runs although

at different times between cases. It is clear that the ring fire acceleration described in [30] is seen in cases (a) and (b).

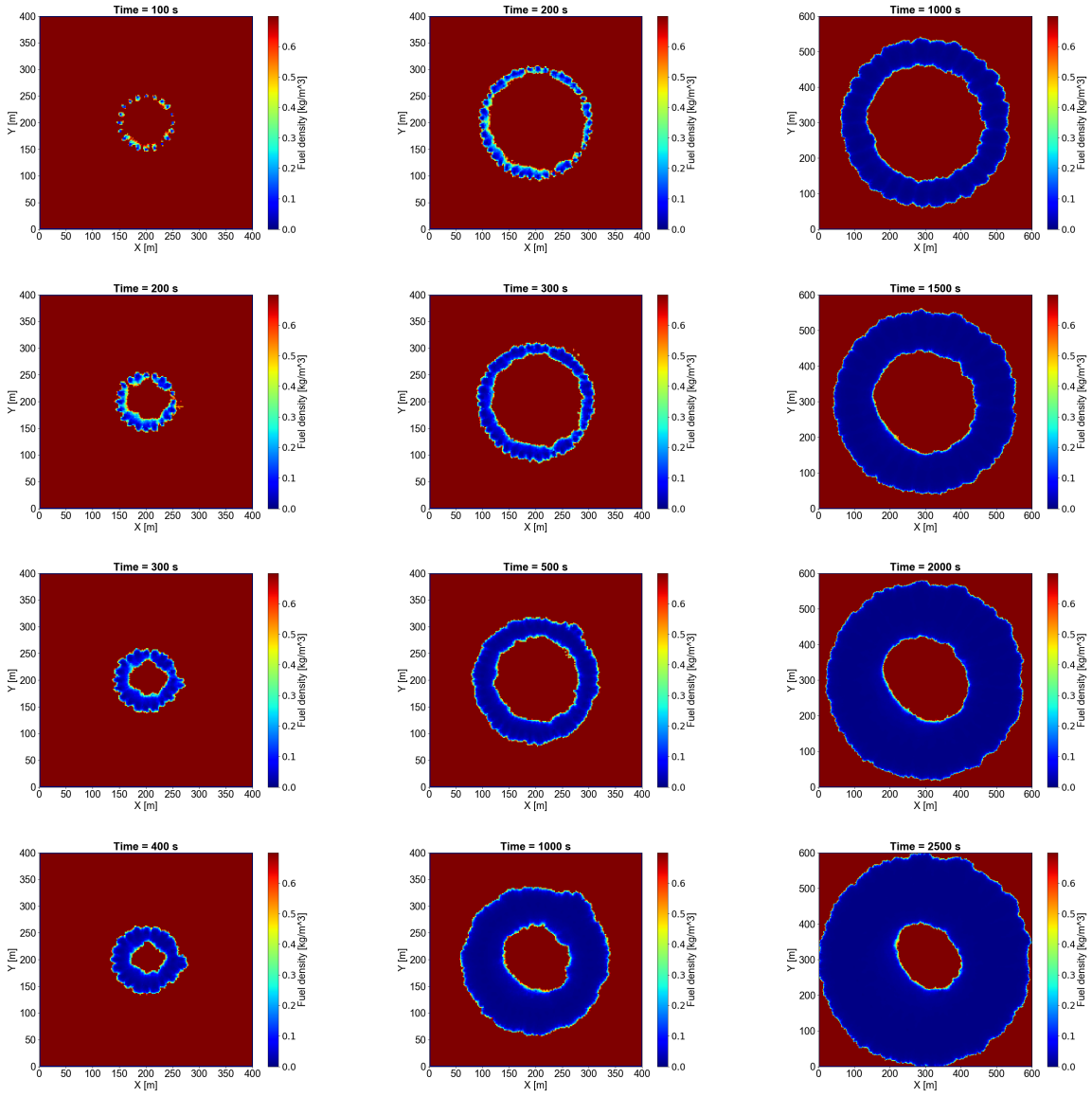

Figure 4.8: Snapshots of simulations using the initial conditions in Figure 4.7 ran with wind fields generated by the original SOR routine. The snapshots are oriented columnwise in order of (a), (b), and (c). Almost no fire acceleration is seen except for in the small ring fire, case (a), in the $t = 100s$ and $t = 200s$ snapshots.

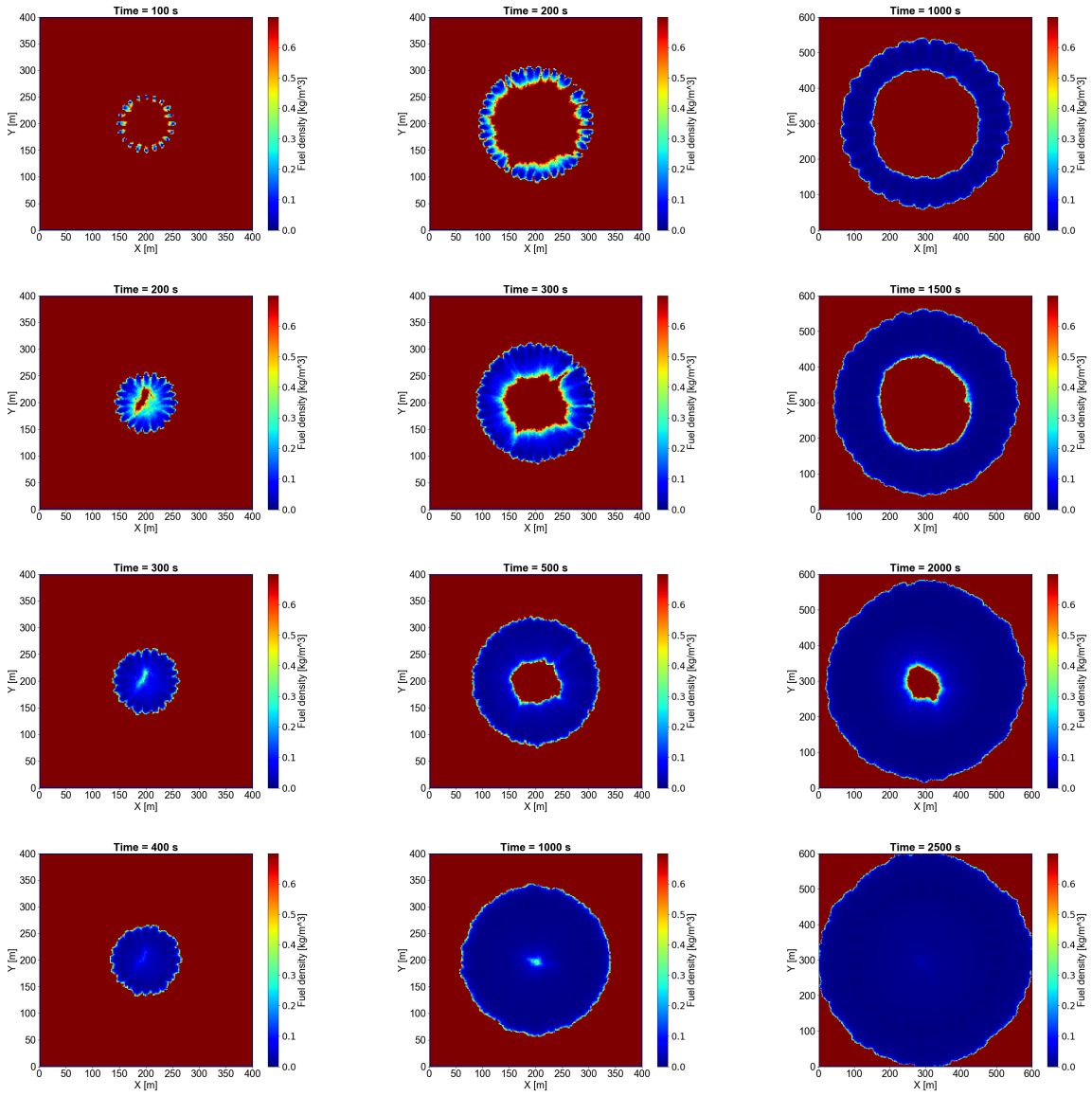

Figure 4.9: Snapshots of simulations using the initial conditions in Figure 4.7 ran with wind fields generated by the modified SOR routine. For comparison the time of the snapshots are the same as those in Figure 4.8 and are oriented in the same columnwise manner.

4.2 Performance of SOR Change

Even though fire-fire interaction is greatly improved by using λ_{prev} it is necessary to test and ensure no strange and persistent wind fields are produced. For longer simulations where a fire may pass by a previously burnt area and indrafts from the previous fire are still present the result could be a very nonphysical evolution of the fire. This section is to test that no such situation would arise and the memory of wind fields in the λ_{prev} matrix decay as expected. Three major concerns are tested in this section given the change:

1. Once all burning regions have extinguished and plumes have dissipated ($R_{i,j,k} = 0$) the induced velocity field must relax back to background velocities. A concern with using λ_{prev} is that wind 'artifacts' will persist even though divergence is zero in the observed wind field.

2. Does the analyzed wind field now suffer from boundary effects? The QUIC-URB domain was originally defined at the extent of where the SOR routine would give non-zero values. Using λ_{prev} extends the region of non-zero values so the Lagrange multipliers will interact with the boundary conditions.

   (a) Does the SOR domain need to be extended for better accuracy?

3. Will using λ_{prev} be a poor initial guess when there are drastic changes in the observed wind field between time steps? This could be an issue under high wind scenarios which result in plume locations moving multiple cells and high fire spread rates each time step.

4.2.1 Relaxation of Error and Generated Wind Artifacts

For the following tests the FIRE-CA algorithm is disabled and plumes are generated by inputting a constant heat flux in specific cells at the surface layer. The code detects this heat flux and generates plumes based on the energy. This simulates combusting fuel but removes the variable intensity caused by the random nature of the FIRE-CA algorithm. Two tests are chosen to test the first concern listed at the beginning of this section. Both tests domain consisted of 160 cells in the x and y directions and 20 vertically stretched cells resulting in a domain extent of [320 m, 320 m, 90 m]. In the first test from 0 to 75 seconds a heat source of 1,000 kW is input at (80 m, 80 m, 0 m). At 75 seconds the first heat source is shut off and a new heat source of 1,000 kW is placed at (240 m, 240 m, 0 m) and the simulation is ran for another 150 seconds. This first test is to see if any wind structures persisted from the first heat source input site and plume. There is no background wind for this test and a solution with λ initialized to zero and 1,000 SOR iterations each time step is used as the ground truth to form the error.

For a second test the same domain is used and a total of 5 plumes are generated in an 'X' configuration. The plume sources in this test are placed closer to each other than in the previous test. Three plumes are started at 0 seconds in a line with heat sources of 1,000 kW at (120 m, 120 m, 0 m), (160 m, 160 m, 0 m), and (200 m, 200 m, 0 m). At 75 seconds two heat sources of 1,000 kW are placed at (120 m, 200 m, 0 m) and (200 m, 120 m, 0 m), forming the 'X', and the initial three heat sources are shut off. Putting the heat sources closer together and in this shape ensures a strong interaction between the winds produced by the new heat sources and the left over wind structure still stored in λ_{prev}. The two later heat sources are turned off at 150 seconds and the simulation is run 100 seconds further to observe the decay of the error when using λ_{prev}.

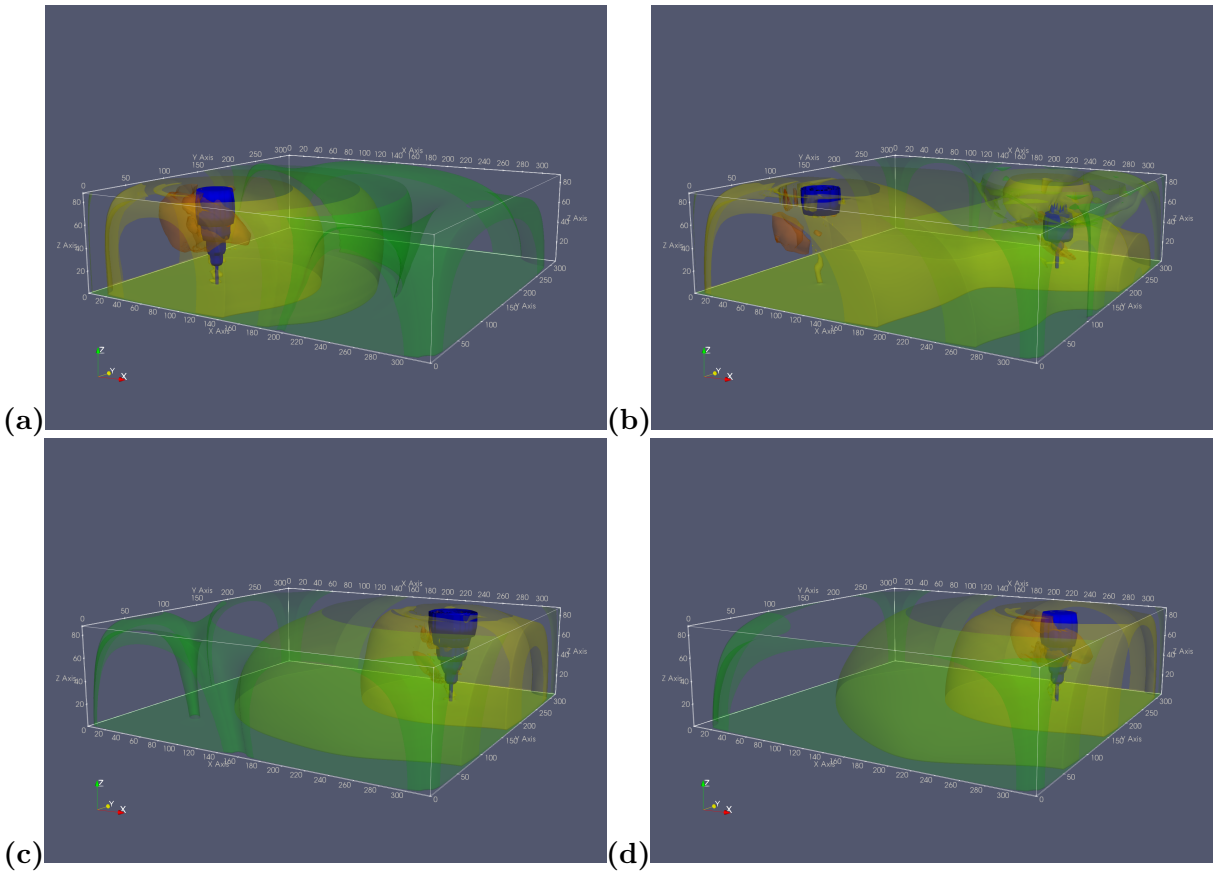

Figure 4.10: Error isosurfaces from the simulation described in the beginning of Section 4.2.1. The blue surface is an isosurface of the plume model generated winds, showing the structure of the plumes. The orange, yellow, light green, and dark green surfaces are isosurfaces for wind speed error thresholds of 1E-1, 1E-2, 1E-3, and 1E-4 respectively. The snapshots (a)-(d) are taken 25, 80, 125, and 150 seconds into the simulation. The decay of the wind field generated from the first plume is evident by the similarity in the error surfaces between (a) and (d).

Results from the first test are shown in Figure 4.10. The first test did not produce any persistent wind artifacts and once the first plume dissipated the error continued to decay where the first plume is located. A promising result from the first test is the symmetry seen in the error between snapshots (a) and (d) in Figure 4.10. The similarity in the error contours surrounding each isolated plume demonstrates that the memory from the initial plume has dissipated significantly. These results are promising but not adequate for ensuring that the modified SOR solver would not find a stationary state once all source terms had shut off.

Visualizations of the second test at various times can be seen in Figure 4.11. Looking at the error isosurfaces in images (c) and (d) there are no obvious residual wind structures left at the points on the 'X' that are turned off at 75 seconds. As all the plume structures leave the domain (images (d), (e), and (f)) the solver continues to iterate and no persistent wind structures remain in the domain. Convergence towards the ground truth solution is visually seen as the lowest value isosurface, where wind errors are on the order of 1E-4, reduces in size and eventually vanishes. By 250 seconds, image (f), velocity errors are on the order of mms^{-1}.

These tests solve the wind field over the entire domain so boundary effects due to the adaptive domain defined by σ still need to be explored. Exploration of the effects of boundary extents on the wind field solution error can be seen in Section 4.2.2.

4.2.2 Investigating Boundary Effects and Convergence

As discussed in Section 1.4 using λ_{prev} as the initial guess extends the influence of the plumes on the wind field beyond the 10 cell limit of the original algorithm. In this section the aim is to show whether the buffer used in the QUIC-URB algorithm, σ, needs to be increased to attain reasonable results. The concern with the boundary is that with the previous version of the SOR algorithm there is never an interaction with the boundary (This is discussed at the beginning of Section 1.4). A variety of scenarios are performed in this section where the L_1 and L_{inf} error norms between the previous SOR algorithm and the modified version discussed previously are compared. To explore the effects of the boundary on the solution the index buffer σ is adjusted to increase the domain extents that the wind field is solved over (σ's role is discussed in Section 1.4). The code is modified for the following tests to only allow the QUIC-URB domain bounds to increase but not decrease. The domain the L_1 and L_{inf} errors will be calculated over will be the maximum domain reached in

the simulation, which is dependent on σ. The error norms are defined as follows:

$$L_1 = \frac{1}{N} \sum_{i=i_{Start}}^{i_{End}} \sum_{j=j_{Start}}^{j_{End}} \sum_{k=k_{Start}}^{k_{End}} \left|u_{i,j,k} - u_{i,j,k}^{True}\right| + \left|v_{i,j,k} - v_{i,j,k}^{True}\right| + \left|w_{i,j,k} - w_{i,j,k}^{True}\right|$$

$$\text{and } L_{\text{inf}} = \max\left(\left|u_{i,j,k} - u_{i,j,k}^{True}\right| + \left|v_{i,j,k} - v_{i,j,k}^{True}\right| + \left|w_{i,j,k} - w_{i,j,k}^{True}\right|\right)_{i,j,k}$$

where N is the total number of (i, j, k) points used in the sum. The true solution for these scenarios is calculated over the entire domain using 1,000 SOR iterations with λ being initialized to zero at each time step.

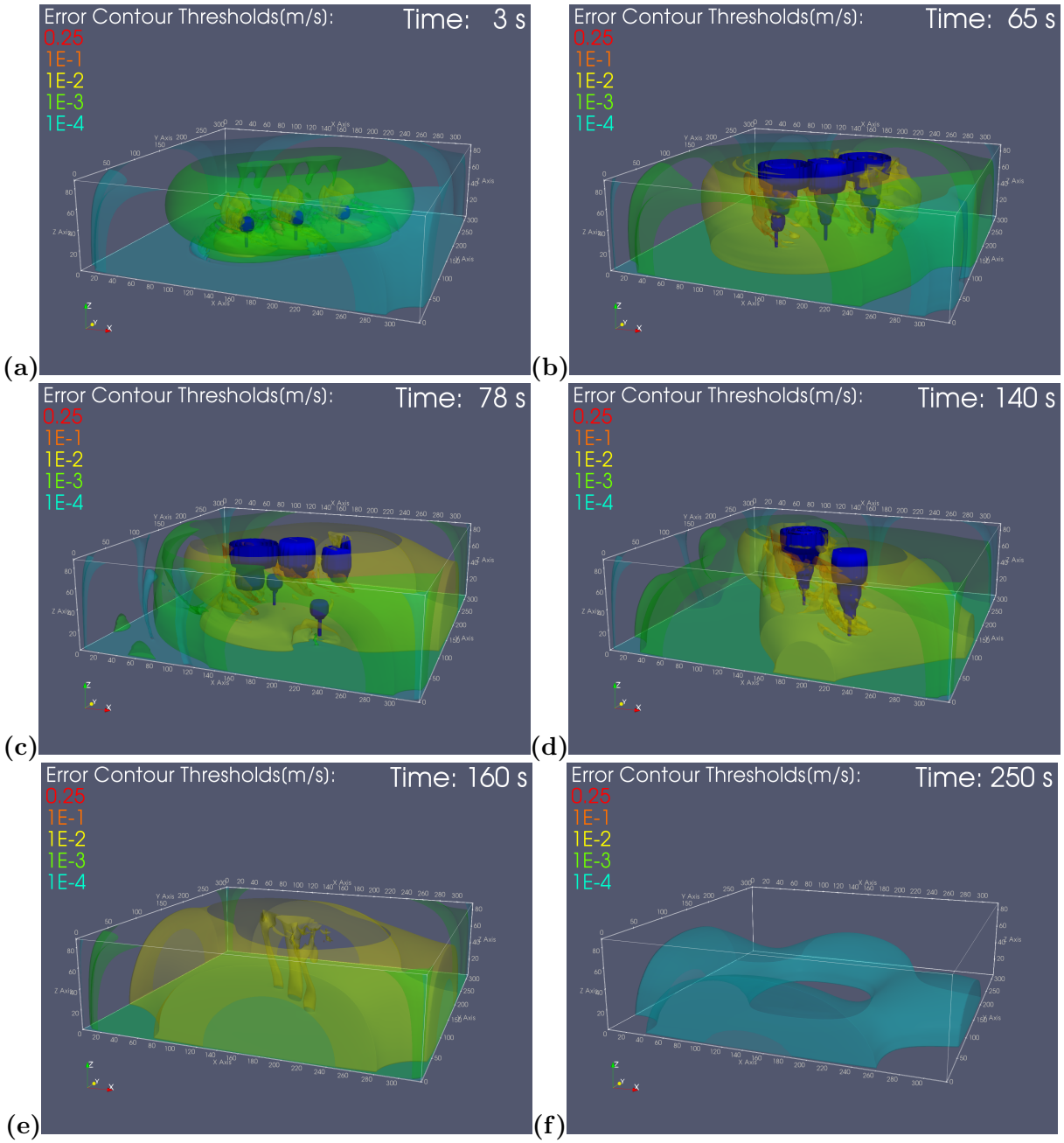

Figure 4.11: Snapshots of the second simulation described in Section 4.2.1 showing error isosurfaces. The blue surfaces are isosurfaces of the plume model generated vertical winds, showing the structure of the plumes. The opaque colored surfaces are isosurfaces for wind speed error thresholds calculated from the 1,000 iteration solution at each time step. Snapshot (c) shows the transition of shutting off the initial line of heat sources to the two heat sources at the points of the 'X' being turned on.

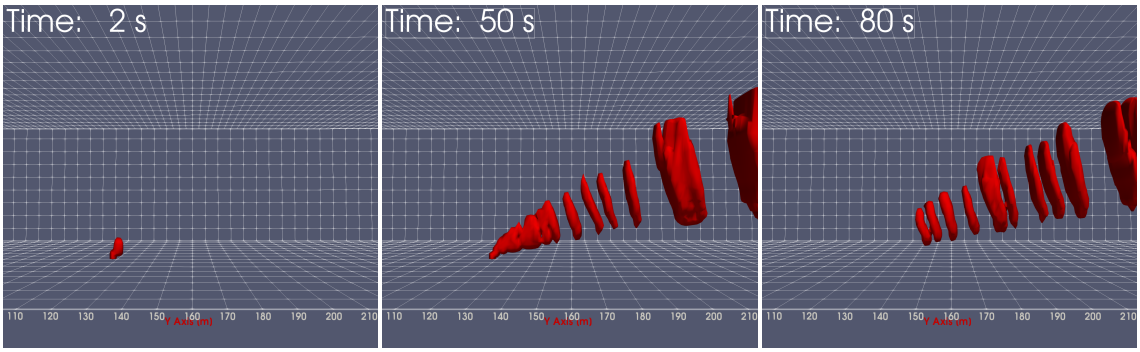

Figure 4.12: Isosurfaces of the vertical velocities generated by the modified QUIC-URB plume model. The plume pictured is generated with a heat source of 1,000 kW located at ground level and a background wind of 3 ms^{-1} in the y-direction. This is the simulation used to generate the error plots in Figure 4.14.

Plume Tests. For the simulations explored in this section the buffer value will be varied by increments of 10 ($\sigma = 10, 20, 30, 40, 50$) to see if a larger domain causes boundary effects, if present, to be reduced and the error improved. For the first two scenarios a plume is generated at the center of the domain at $t = 0s$ using the same methodology as described in Section 4.2.1. The same domain and heat source of 1,000 kW is also used. As with the second test of Section 4.2.1 the heat source is turned off 75 seconds in and the simulation is run until 250 seconds has elapsed. Running the simulation past the point plumes are present in the domain is to analyze whether the analyzed wind field relaxes to background wind values when there is no divergence in the observed wind field. In the second scenario all initial conditions are the same except for a background wind speed in the y-direction of 3 ms^{-1}.

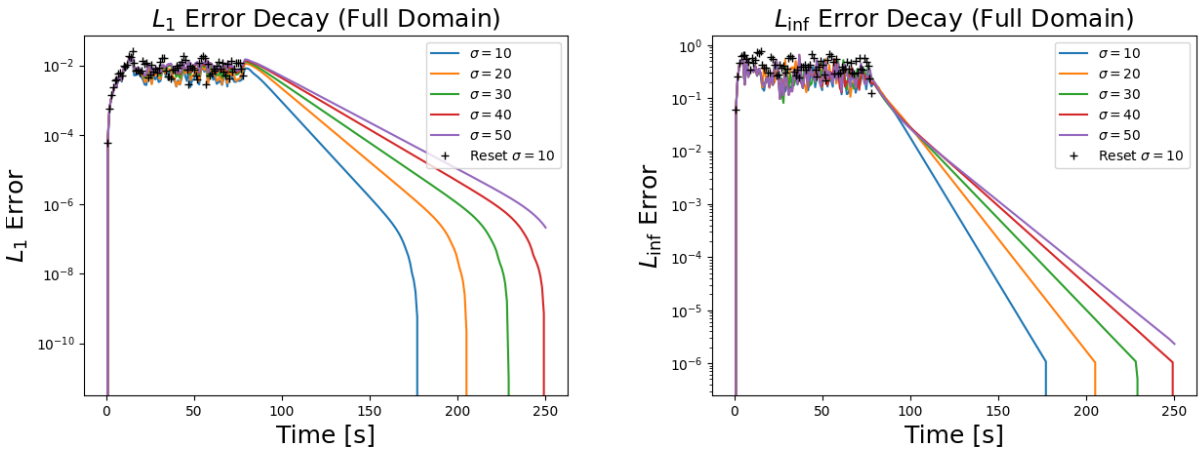

Figure 4.13: Graphs of the L_1 and L_{inf} errors for the single plume with no wind case.

The results in Figure 4.13 for a single plume with no wind show that using λ_{prev} has almost identical errors as that of the original algorithm. The sudden drop in error of the original algorithm, black crosses, occurs because once all of the plumes dissipate $\lambda = 0$ instantaneously becomes the exact solution that satisfies (1.3). All error curves using the new algorithm converge to the exact solution although they do so at different rates. There are no boundary effects seen on the solution as there is no significant change in the error measures between different σ values. The only effect seen from increasing the domain size is that convergence to the $\lambda = 0$ solution is slowed. This is expected since with a larger domain the λ matrix has many more non-zero values that need to be relaxed to zero. The results for the wind case in Figure 4.14 are similar in performance when looking at the L_1 error but show larger maximum errors. This is due to the separation of the plume segments that can be seen at greater heights. Since these structures translate with background wind gaps can form between plume sections. The SOR algorithm using λ_{prev} will have errors when adjusting to the moving gaps with just 10 iterations done per time step. To test this hypothesis the error is also calculated for the bottom 10 layers of the domain instead of all 20 (shown in the bottom row of Figure 4.14). These plots show a slight decrease in the L_{inf} error and the error in the L_1 error aligning with the 'Reset' results supporting this hypothesis. Again in these results, similar to the no wind case, no improvement is seen in the error with larger σ, only slower convergence to the exact solution once the plume has dissipated. This case demonstrates that a new error is introduced by using λ_{prev} when background winds cause the plume model segments to separate leaving gaps of zero vertical velocities between. Fortunately the larger errors are higher up in the

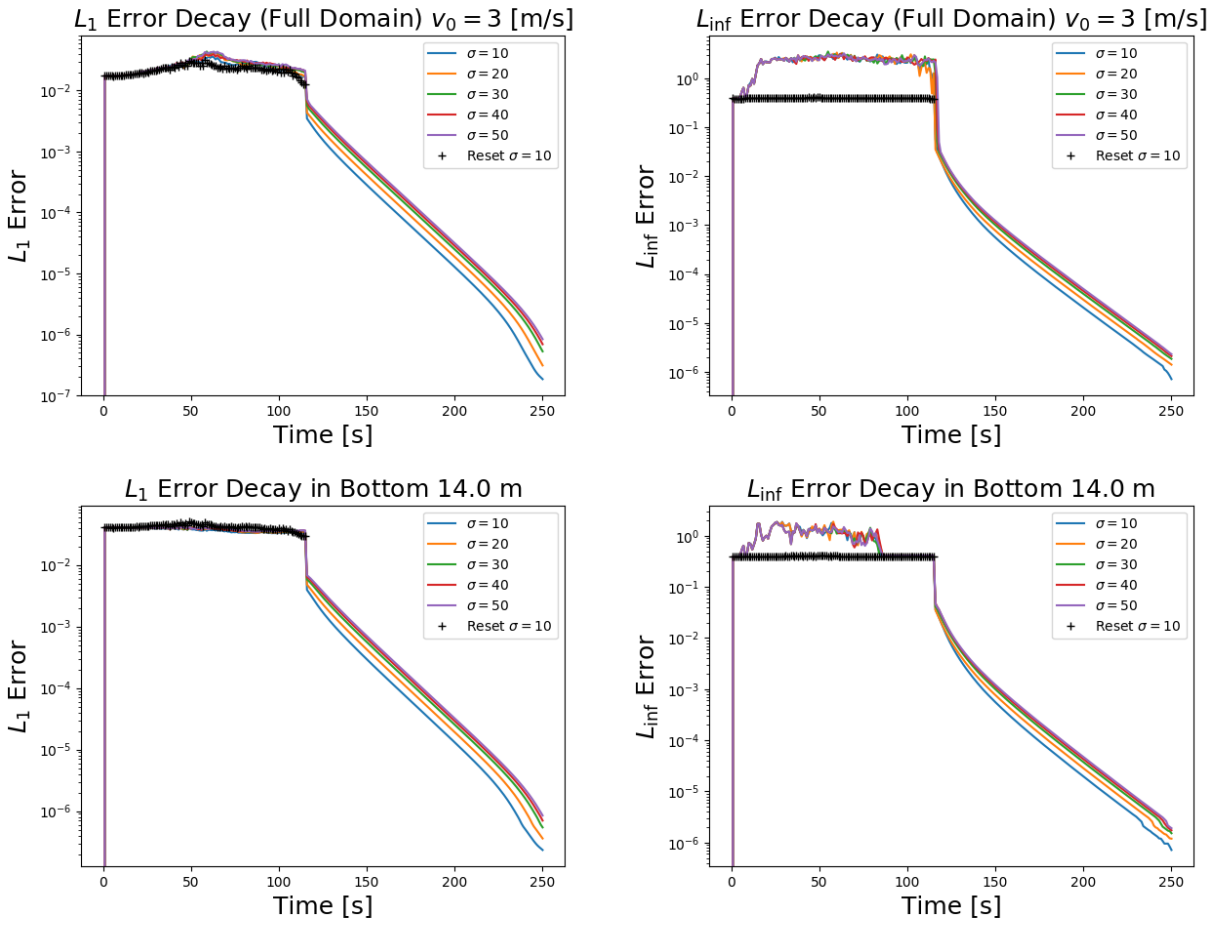

Figure 4.14: Graphs of the L_1 and L_{inf} errors for the single plume with $v_0 = 3$ ms^{-1}. The top row plots are errors calculated using the entire domain defined by σ and the bottom row shows errors that are calculated using the bottom 14.0 meters of the domain (bottom 10 cells).

domain meaning these errors don't contribute directly to the fire spread routine as plumes near the surface don't tend to have separations between plume segments.

Fire Simulation Tests. For the following tests the same wind field comparisons done in 4.2.2 are carried out for two fire simulations. The aim of these tests is to see if the modified SOR algorithm is generating reasonable wind fields with fire generated plumes. The first simulation is like the head fire simulation shown in Figure 4.6. A background wind of 3 ms^{-1} in the x-direction forms a parabolic shape as the fire develops. The second simulation consists of six spot fires in three pairs of increasing radius (See Figure 4.15). The pairs are in line of the direction of the wind in the y-direction of 3 ms^{-1}. These tests are to show whether using λ_{prev} will not generate

significantly large errors in the wind field or divergent behavior in the solver. The head fire test will demonstrate this for an individual fire shape and the spot fire test aims to demonstrate this for fire-fire interactions.

In both simulations the wind field generated from the original SOR algorithm is used in FIRE-CA to evolve the fire. Again, a 1,000 iteration solution starting with $\lambda = 0$ and iterating over the entire domain is used for the ground truth solution for forming the errors. The L_1 and L_{inf} errors used in the plume tests will also be used here.

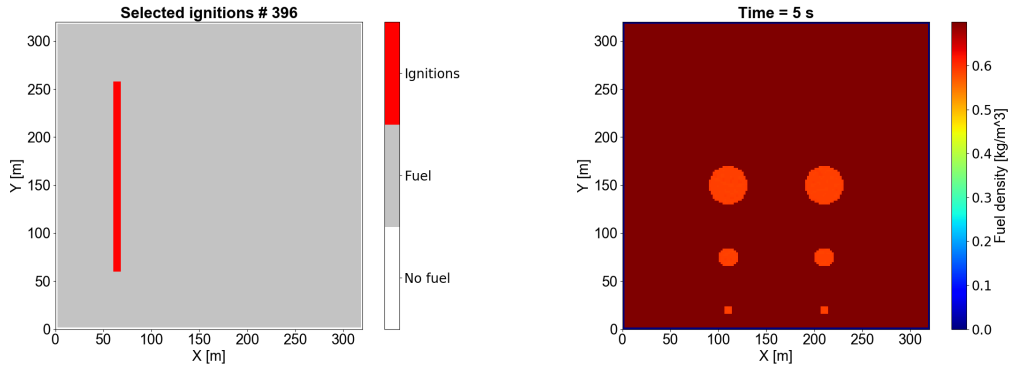

Figure 4.15: Shown are the initial ignition patterns for the tests described in Section 4.2.2. The spot fire ignition pattern uses a custom ignition pattern routine that is unable to produce the same initial ignition plot as the left side. Due to this the fuel density at 5 seconds into the simulation is shown to show the initial ignition pattern.

The results shown in Figure 4.16 show that the wind field determined using the modified SOR algorithm performs on-par or better than the original algorithm for $\sigma = 10$ in most measures. In the L_1 measures the $\sigma = 10$ error curves show similar or lower errors than the 'Reset' results. When looking at the L_{inf} measures there are higher errors for all of the solutions using λ_{prev}. This is expected as discussed in Section 4.2.2 due to the combination of using λ_{prev} and plume segments having gaps between them. The indrafts calculated during the previous time step to satisfy (1.3) are still represented in the λ matrix and 10 iterations aren't enough to completely overwrite the memory of those. This is the reason the $\sigma = 10$ error is lowest in the L_1 measures due to it's faster convergence to zero, seen in Figure 4.13, than all other simulations with larger σ values. The L_{inf} results show that for both simulations using λ_{prev} gives larger maximum errors in most cases. However, in the spot fire case a σ value of 10 has maximum errors on the same order as setting λ

to zero each timestep. This suggests that the errors are mostly coming from the domain extents as all other buffer sizes show a larger maximum error.

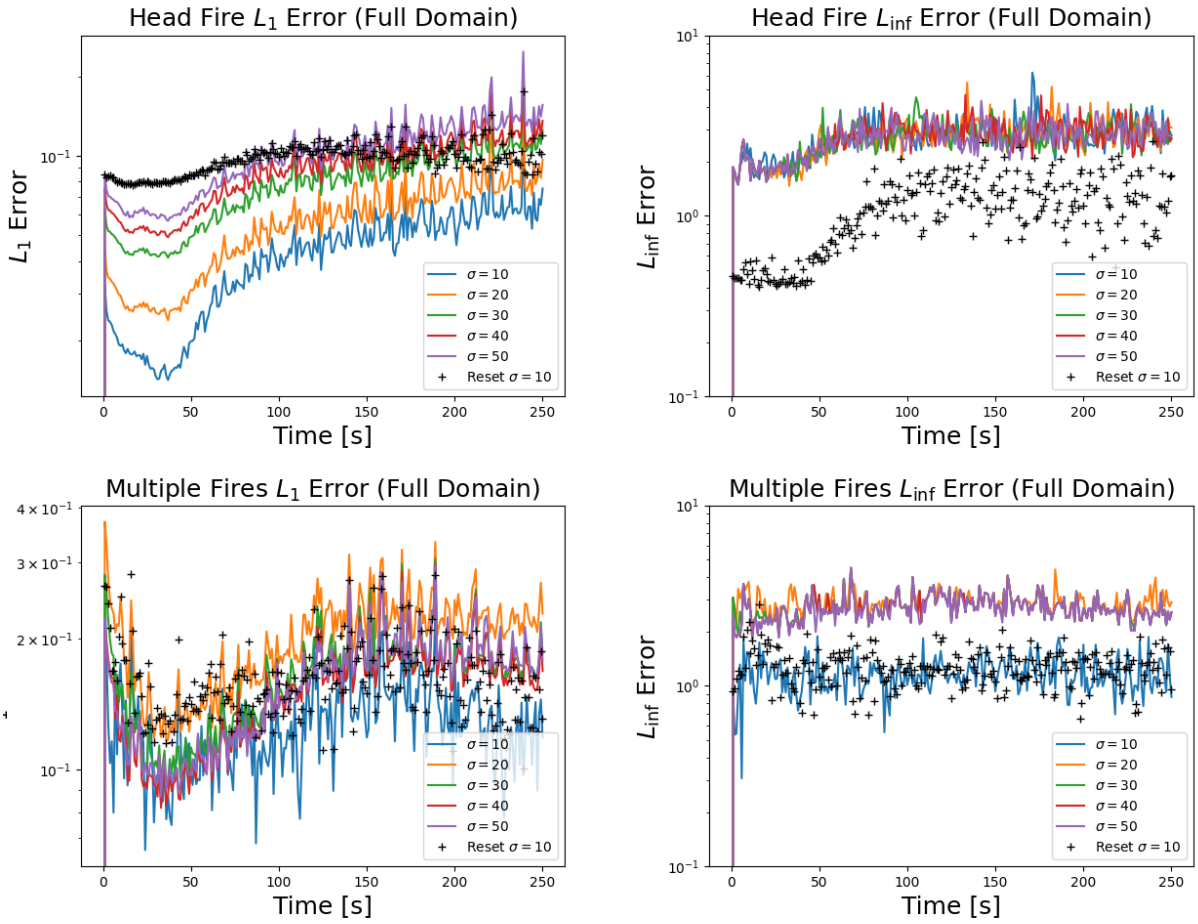

Figure 4.16: Graphs of the L_1 and L_{inf} errors for the head fire and spot fire tests with a background wind speed of 3ms^{-1}. The errors are calculated using the entire domain defined by σ with the top row showing errors from the head fire case and the bottom row showing results from the spot fires case.

4.3 Conclusions

From results seen in Figures 4.3 – 4.6, 4.8, and 4.9 using λ_{prev} as the initial guess for the SOR algorithm greatly improves fire-fire interactions in simulations. These interactions are crucial to capture in QUIC-Fire for it to be useful to prescribed fire managers. Many burn plans implemented by managers utilize fire-fire interactions to predictably control fire spread and minimize risks [2, 30]. The most drastic change observed from the change is the ability to capture the collapse of a center fire in which using $\lambda = 0$ as the initial guess showed no collapse. The large discrepancy

in fire arrival time, seen in Figures 4.8 and 4.9, highlight the importance of the change as being able to capture these significant increases in spread rates is important for keeping practitioners safe when planning prescribed burns.

The concerns mentioned at the beginning of Section 4.2 over the use of λ_{prev} are almost entirely satisfied. From tests in Sections 4.2.1 and 4.2.2 it is shown that no persistent artifacts remain after all plumes leave the computational domain. The wind field relaxes to background wind values with and without the interaction of multiple plumes taking place in the simulation. In the plume tests increasing the buffer size, σ, did not effect error metrics when comparing to the original algorithm. It is observed that with nonzero background winds the translation of plume segments did cause added error when using λ_{prev} as the initial guess. However, this error mainly occurs higher in the domain where fire behavior would not be affected. In the cases where errors are calculated using winds from a simulation containing fire spread, Section 4.2.2, errors with the new algorithm are comparable to the original version and in some cases performed better when compared to the 1,000 iteration solution. Results showed that increasing the buffer size actually increases error in the solution and the optimal buffer value is 10 when using λ_{prev}. In summary using λ_{prev} as the initial guess greatly improved the interactions between fires which was previously not present in QUIC-Fire unless fires are very near to each other. The error introduced by this change pales in comparison to the increase in fire phenomenology it allows QUIC-Fire to capture.

CHAPTER 5

FUTURE DIRECTIONS

This dissertation outlines improvements made to the QUIC-URB and QUIC-Fire algorithm in terms of expanding the domains that they are useful for. However, the work in this dissertation also highlighted places where improvements can be made to both QUIC-URB and QUIC-Fire. The following are planned directions where research will be conducted to further improve the two algorithms.

Wake Parameterizations for Terrain. One of the key components to the usefulness of the QUIC-URB algorithm is the wake-eddy parameterizations it uses to produce wind fields in urban environments. Mass conservation is simply not enough to generate the complex flow seen around buildings. To generate flows seen in the real-world while keeping the algorithm fast-running, the creators of QUIC-URB use parameterizations for momentum driven effects like eddys, recirculations, and flow separations (Figures 5.1 and 5.3). These parameterizations are used to inject different flows into a background wind field and then mass-conservation is enforced resulting in a mass consistent wind field that contains different forms of complex flows (Figure 5.2). Flow separations are absent from the solutions generated from the TF version of QUIC-URB described in Chapter 2 and leads to over-predictions in fire spread rates at the top of hills in Chapter 3. Future work is planned to apply these building wake parameterizations to terrain features in a domain where they would apply. For example, applying the 'Rooftop recirculation' seen in Figure 5.3 near the tops of hills where separations are expected. HIGRAD/FIRETEC simulations will be used to determine how parameterizations should be adjusted to apply to terrain features and establish metrics for detecting where these features should occur. Once adjusted parameterizations are determined the next hurdle will be developing a methodology for quickly detecting across a domain where these parameterizations apply. It may be useful to train a machine learning algorithm using a combination of parameterization maps for a variety of terrains, the terrain maps, and startup wind fields from the TF QUIC as a training set. Quickly applying these parameterizations to any terrain/wind-field combination using minimal computational resources is required to keep QUIC-Fire viable for fire practitioners.

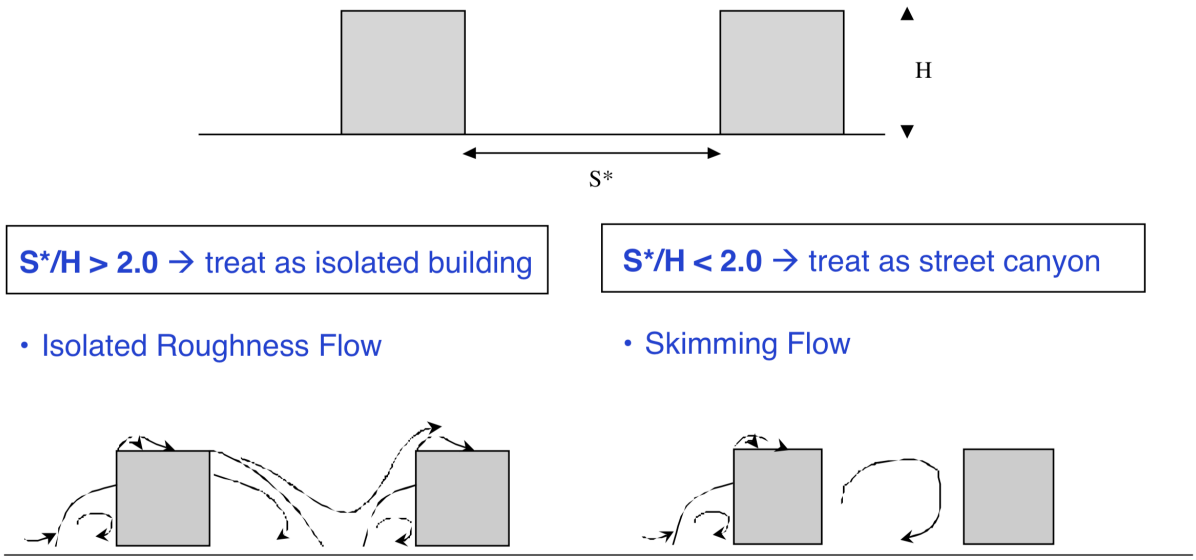

Figure 5.1: Diagram from [33] showing how QUIC-URB determines whether street canyon parameterizations or isolated flow parameterizations should be injected around a building.

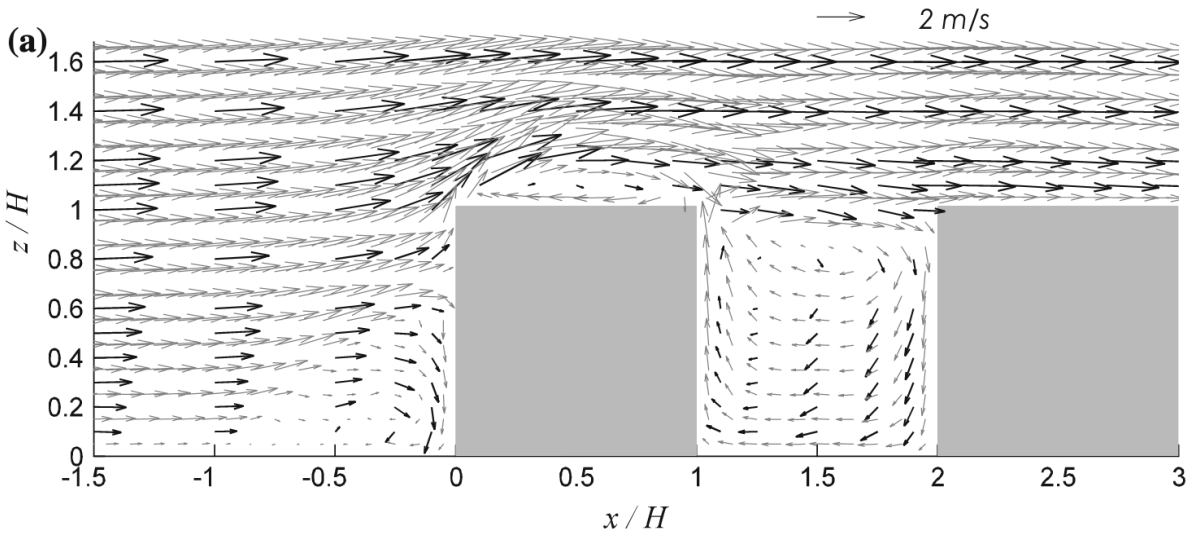

Figure 5.2: Diagram from [33] showing the wind field resulting from enforcing mass conservation after flow parameterizations have been injected into the background wind field.

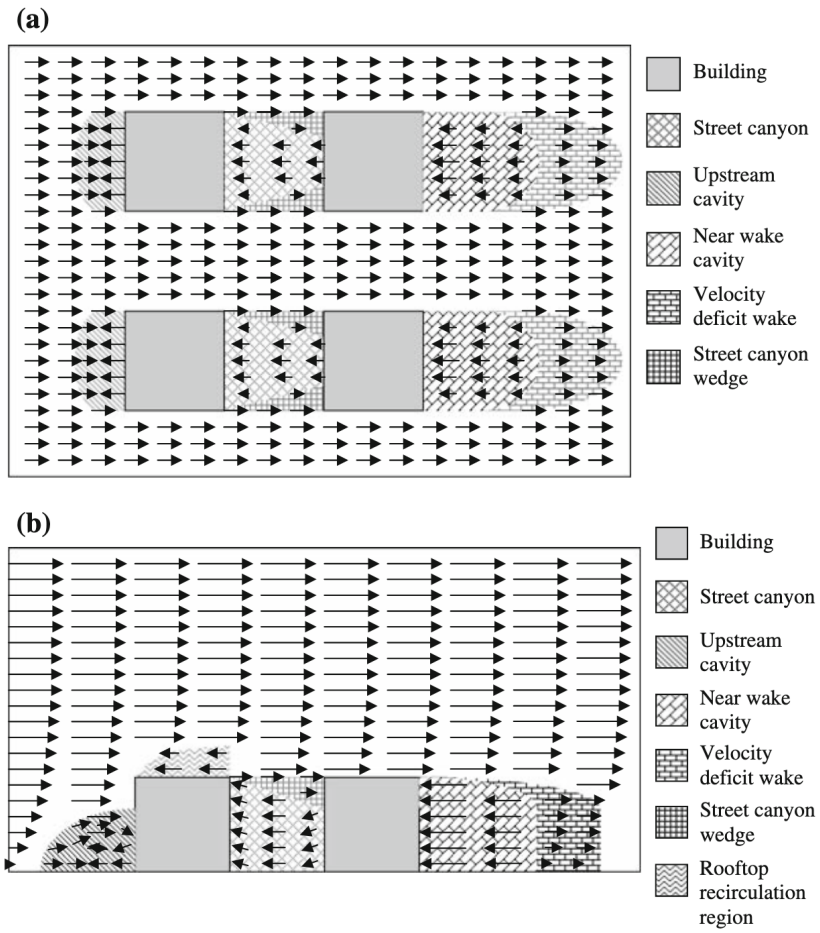

Figure 5.3: Diagram from [33] showing how different flow parameterizations are used together to generate complex flows around four buildings as seen from the top (a) and side (b).

FIRE-CA Improvements. The current implementation of the FIRE-CA algorithm accounts for the flame-tilt angle by using a comparison between local horizontal and vertical winds within a burning fuel cell. The tilt of a flame affects its relative angle with the terrain surface which has been shown to be a key driver in fire spread on slopes [47, 55]. Work is planned to modify subgrid calculations to capture the interaction between a tilting flame and the local surface, especially in low wind conditions. In low wind laboratory conditions, flame-tilt has been observed to be significantly affected by slope [14]. Accounting for the local entrainment imbalance due to the buoyant updraft interacting with the sloped terrain surface will be key to correctly model the tilt of the flame. This can be done by using the subgrid quantities tracked in QUIC-Fire to approximate the fire-induced buoyancy near the surface and the geometry associated with the subgrid fire. Modifications to

how flame tilting is captured in FIRE-CA is expected to bring spread behavior more in line with FIRETEC results seen in Chapter 3.

Another subject for future work is the way drag from vegetation is calculated and updated in FIRE-CA. Currently drag is realized in QUIC-Fire as a linear interpolation from a wind profile derived in [8] to background wind values as fuel is depleted in a cell [20]. This implementation works well in simulations with dense forest and grass fires but falls short where different fuel structures interface with each other, i.e. where grasslands meet forested regions, as evidenced by results in Section 3.5.5. In these regions a local drag approximation cannot account for stronger wind channeling in the subcanopy, in the case of a grassland to forest transition, as it does not account for higher near surface velocities upwind. Likewise, the model will underpredict the effect of drag in forest clearings as it is unaware of the surrounding fuel acting as barriers to the wind. Work is planned to incorporate some nonlocal approximations to improve the drag model for these scenarios.

GPU Offloading for Terrain-Following SOR. Improvements to algorithms typically come with slow down to overall computational speed of the algorithm. A way of increasing the head room QUIC-Fire has to improve in other areas while retaining sub real-time simulation speeds are to use GPU offloading to greatly increase the speed of some of the routines in QUIC-Fire. The SOR routine makes a great candidate for use with a GPU due to solving linear systems of equations being a proven use case for GPU hardware [4, 39, 43]. Also, the original algorithm of QUIC-URB has already been implemented on a GPU showing speedup factor of 128 for a domain consisting of $\sim 145\times10^6$ cells [5]. This approach uses the same red-black coloring scheme to separate a single SOR iteration into two separate update steps to avoid cells that are being updated from being sampled in the same step by other cells [18, 19]. Adapting the TF version of QUIC-URB for use with GPUs requires careful consideration as the iterative stencil for each SOR iteration involves sampling 14 of the neighboring cells as compared with the 6 required for the original QUIC-URB algorithm. This means a red-black coloring scheme will not be sufficient as read-write race conditions are not alleviated by a two colored approach. Instead a multi-colored scheme is required which have been theoretically shown to share convergence rates with two colored approaches [1].

BIBLIOGRAPHY

[1] Loyce M. Adams and Harry F. Jordan. "Is SOR Color-Blind?" In: *SIAM Journal on Scientific and Statistical Computing* 7.2 (1986), pp. 490–506. DOI: 10.1137/0907033. URL: https://doi.org/10.1137/0907033.

[2] Matthew A Albrecht and Brian C McCarthy. "Effects of Prescribed Fire and Thinning on Tree Recruitment Patterns in Central Hardwood Forests." In: *Forest Ecology and Management* 226.1-3 (2006), pp. 88–103.

[3] Howard R Baum and BJ McCaffrey. "Fire Induced Flow Field-Theory and Experiment." In: *Fire Safety Science* 2 (1989), pp. 129–148.

[4] Peter Benner et al. "Matrix Inversion on CPU-GPU Platforms with Applications in Control Theory." In: *Concurrency Computation Practice and Experience* 25 (June 2013), pp. 1170–1182. DOI: 10.1002/cpe.2933.

[5] Behnam Bozorgmehr et al. "Utilizing Dynamic Parallelism in CUDA to Accelerate a 3D Red-Black Successive Over Relaxation Wind-Field Solver." In: *Environmental Modelling Software* 137 (2021), p. 104958. ISSN: 1364-8152. DOI: https://doi.org/10.1016/j.envsoft.2021.104958. URL: https://www.sciencedirect.com/science/article/pii/S1364815221000013.

[6] M. Brown et al. *An Overview of the EMRTC Complex-Terrain Dual-Tracer Experiment*. Tech. rep. Los Alamos National Lab.(LANL), Los Alamos, NM (United States), 2020.

[7] J.M. Canfield et al. "A Numerical Investigation of the Interplay between Fireline Length, Geometry, and Rate of Spread." In: *Agricultural and Forest Meteorology* 189-190 (2014), pp. 48–59. ISSN: 0168-1923. DOI: https://doi.org/10.1016/j.agrformet.2014.01.007. URL: https://www.sciencedirect.com/science/article/pii/S0168192314000082.

[8] Ronald M. Cionco. "A Mathematical Model for Air Flow in a Vegetative Canopy." In: *Journal of Applied Meteorology and Climatology* 4.4 (1965), pp. 517–522. DOI: https://doi.org/10.1175/1520-0450(1965)004<0517:AMMFAF>2.0.CO;2. URL: https://journals.ametsoc.org/view/journals/apme/4/4/1520-0450_1965_004_0517_ammfaf_2_0_co_2.xml.

[9] Kelly R Close. *Fire Behavior vs. Human Behavior: Why the Lessons from Cramer Matter*. Citeseer, 2005.

[10] Janice L Coen. "Modeling Wildland Fires: A Description of the Coupled Atmosphere Wildland Fire Environment Model (CAWFE)." In: (2013).

[11] Janice L Coen et al. "WRF-Fire: Coupled Weather–Wildland Fire Modeling with the Weather Research and Forecasting Model." In: *Journal of Applied Meteorology and Climatology* 52.1 (2013), pp. 16–38.

[12] GA Davidson. "Simultaneous Trajectory and Dilution Predictions from a Simple Integral Plume Model." In: *Atmospheric Environment (1967)* 23.2 (1989), pp. 341–349.

[13] GA Davidson. "Simultaneous Trajectory and Dilution Predictions from a Simple Integral Plume model." In: *Atmospheric Environment (1967)* 23.2 (1989), pp. 341–349.

[14] Jean-Luc Dupuy et al. "The Effects of Slope and Fuel Bed Width on Laboratory Fire Behavior." In: *International Journal of Wildland Fire* 20 (Jan. 2011), p. 272. DOI: 10.1071/WF09075.

[15] Mark A Finney and Sara S McAllister. "A Review of Fire Interactions and Mass Fires." In: *Journal of Combustion* 2011 (2011).

[16] Jason M Forthofer, Bret W Butler, and Natalie S Wagenbrenner. "A Comparison of Three Approaches for Simulating Fine-Scale Surface Winds in Support of Wildland Fire Management. Part I. Model Formulation and Comparison Against Measurements." In: *International Journal of Wildland Fire* 23.7 (2014), pp. 969–981.

[17] Scott L Goodrick et al. "Modelling Smoke Transport from Wildland Fires: A Review." In: *International Journal of Wildland Fire* 22.1 (2012), pp. 83–94.

[18] Linda Jo Hanes Hayes. "Comparative Analysis of Iterative Techniques for Solving Laplace's Equation on the Unit Square on a Parallel Processor." PhD thesis. University of Texas at Austin, 1974.

[19] Jules Joseph Lambiotte Jr. *The Solution of Linear Systems of Equations on a Vector Computer.* University of Virginia, 1975.

[20] R.R. Linn et al. "QUIC-Fire: A Fast-running Simulation Tool for Prescribed Fire planning." In: *Environmental Modelling & Software* 125 (Mar. 2020), p. 104616. DOI: 10.1016/j.envsoft.2019.104616. URL: https://doi.org/10.1016.

[21] Rodman Linn et al. "Coupled Influences of Topography and Wind on Wildland Fire Behaviour." In: *International Journal of Wildland Fire* 16.2 (2007), pp. 183–195. DOI: 0.1071/WF06078. URL: https://doi.org/10.1071/WF06078.

[22] Rodman Linn et al. "Incorporating field wind data into FIRETEC simulations of the International Crown Fire Modeling Experiment (ICFME): preliminary lessons learned." In: *Canadian Journal of Forest Research* 42.5 (May 2012), pp. 879–898. DOI: 10.1139/x2012-038. URL: https://doi.org/10.1139%5C%2Fx2012-038.

[23] Rodman Linn et al. "Modeling Interactions Between Fire and Atmosphere in Discrete Element Fuel Beds." In: *International Journal of Wildland Fire* 14.1 (2005), pp. 37–48. DOI: 10.1071/WF04043. URL: https://doi.org/10.1071/WF04043.

[24] Rodman R Linn and Philip Cunningham. "Numerical Simulations of Grass Fires Using a Coupled Atmosphere–Fire Model: Basic Fire Behavior and Dependence on Wind Speed." In: *Journal of Geophysical Research: Atmospheres* 110.D13 (2005).

[25] Rodman R Linn et al. "A Numerical Study of Slope and Fuel Structure Effects on Coupled Wildfire Behaviour." In: *International Journal of Wildland Fire* 19.2 (2010), pp. 179–201.

[26] Rodman R. Linn et al. "Modeling Low Intensity Fires: Lessons Learned from 2012 Rx-CADRE." In: *Atmosphere* 12.2 (Jan. 2021), p. 139. DOI: 10.3390/atmos12020139. URL: https://doi.org/10.3390%5C%2Fatmos12020139.

[27] Rodman Ray Linn et al. "QUIC-fire: A Fast-Running Simulation Tool for Prescribed Fire Planning." In: *Environmental Modelling & Software* 125 (2020), p. 104616.

[28] Jan Mandel, Jonathan D Beezley, and Adam K Kochanski. "Coupled Atmosphere-Wildland Fire Modeling with WRF 3.3 and SFIRE 2011." In: *Geoscientific Model Development* 4.3 (2011), pp. 591–610.

[29] R Markovinović and JD Jansen. "Accelerating Iterative Solution Methods using Reduced-Order Models as Solution Predictors." In: *International journal for numerical methods in engineering* 68.5 (2006), pp. 525–541.

[30] Robert E Martin and John D Dell. "Planning for Prescribed Burning in the Inland Northwest." In: *Gen. Tech. Rep. PNW-GTR-076. Portland, OR: US Department of Agriculture, Forest Service, Pacific Northwest Research Station: 1-67* 76 (1978).

[31] William Mell et al. "Numerical Simulations of Grassland Fire Behavior from the LANL-FIRETEC and NIST-WFDS Models." In: *Remote Sensing and Modeling Applications to Wildland Fires*. Springer, 2013, pp. 209–225.

[32] N Moussiopoulos and Th Flassak. "Two Vectorized Algorithms for the Effective Calculation of Mass-Consistent Flow Fields." In: *Journal of Applied Meteorology and Climatology* 25.6 (1986), pp. 847–857.

[33] Eric R Pardyjak and Michael Brown. "QUIC-URB v. 1.1: Theory and User's Guide." In: *Los Alamos National Laboratory, Los Alamos, NM* (2003).

[34] David Robinson et al. "QUIC-URB and QUIC-fire Extension to Complex Terrain: Development of a Terrain-Following Coordinate System." In: *Environmental Modelling & Software* 159 (2023), p. 105579. DOI: 10.1016/j.envsoft.2022.105579.

[35] R Rockle. *Bestimmung der Stomungsverhaltnisse im Bereich komplexer Bebauungsstrukturen." der Technischen Hochschule Darmstadt*. 1990.

[36] DG Ross et al. "Diagnostic Wind Field Modeling for Complex Terrain: Model Development and Testing." In: *Journal of Applied Meteorology (1988-2005)* (1988), pp. 785–796.

[37] Richard C Rothermel. "Fire Behavior Considerations of Aerial Ignition." In: *Mutch, RW (technical coordinator) Prescribed fire by aerial ignition, Proccedings of a workshop. Intermountain Fire Council, Missoula, Montana*. 1985.

[38] Stefano Serafin et al. "Exchange Processes in the Atmospheric Boundary Layer over Mountainous Terrain." In: *Atmosphere* 9.3 (2018), p. 102.

[39] Girish Sharma, Abhishek Agarwala, and Baidurya Bhattacharya. "A Fast Parallel Gauss Jordan Algorithm for Matrix Inversion using CUDA." In: *Computers Structures* 128 (2013), pp. 31–37. ISSN: 0045-7949. DOI: https://doi.org/10.1016/j.compstruc.2013.06.015. URL: https://www.sciencedirect.com/science/article/pii/S0045794913002095.

[40] Jason J Sharples, Richard HD McRae, and Stephen R Wilkes. "Wind–Terrain Effects on the Propagation of Wildfires in Rugged Terrain: Fire Channelling." In: *International Journal of Wildland Fire* 21.3 (2012), pp. 282–296.

[41] Andrew H Sherman. "On Newton-Iterative Methods for the Solution of Systems of Nonlinear Equations." In: *SIAM Journal on Numerical Analysis* 15.4 (1978), pp. 755–771.

[42] Christine A Sherman. "A Mass-Consistent Model for Wind Fields over Complex Terrain." In: *Journal of Applied Meteorology and Climatology* 17.3 (1978), pp. 312–319.

[43] Jungkyun Shin et al. "3D Laplace-domain Full Waveform Inversion Using a Single GPU Card." In: *Computers Geosciences* 67 (2014), pp. 1–13. ISSN: 0098-3004. DOI: https://doi.org/10.1016/j.cageo.2014.02.006. URL: https://www.sciencedirect.com/science/article/pii/S0098300414000466.

[44] Colin C Simpson et al. "Large Eddy Simulation of Atypical Wildland Fire Spread on Leeward Slopes." In: *International Journal of Wildland Fire* 22.5 (2013), pp. 599–614. URL: https://doi.org/10.1071/WF12072.

[45] Balwinder Singh et al. "Evaluation of the QUIC-URB Fast Response Urban Wind Model for a Cubical Building Array and Wide Building Street Canyon." In: *Environmental fluid mechanics* 8.4 (2008), pp. 281–312.

[46] PA Taylor and HW Teunissen. "The Askervein Hill Project: Overview and Background Data." In: *Boundary-layer meteorology* 39.1 (1987), pp. 15–39.

[47] "The Contribution of Radiant Heat Transfer to Laboratory-scale Fire Spread Under the Influences of Wind and Slope." In: *Fire Safety Journal* 36.6 (2001), pp. 519–543. ISSN: 0379-7112. DOI: https://doi.org/10.1016/S0379-7112(00)00064-3. URL: https://www.sciencedirect.com/science/article/pii/S0379711200000643.

[48] CM Thomas, JJ Sharples, and JP Evans. "Pyroconvective Interaction of Two Merged Fire Lines: Curvature Effects and Dynamic Fire Spread. In 'MODSIM2015." In: *21st international congress on modelling and simulation*. Vol. 29. 2015, pp. 312–318.

[49] Javier Trelles and Patrick J Pagni. "Fire-Induced Winds in the 20 October 1991 Oakland Hills fire." In: *Fire Safety Science* 5 (1997), pp. 911–922.

[50] Takanori Uchida and Kenichiro Sugitani. "Numerical and Experimental Study of Topographic Speed-Up Effects in Complex Terrain." In: *Energies* 13.15 (2020), p. 3896.

[51] Domingos Viegas et al. "Study of the Jump Fire Produced by the Interaction of Two Oblique Fire Fronts. Part 1. Analytical Model and Validation with No-Slope Laboratory Experiments." In: *International Journal of Wildland Fire* 21 (Jan. 2012), pp. 843–856. DOI: 10.1071/WF10155.

[52] Natalie S Wagenbrenner et al. "Development and Evaluation of a Reynolds-Averaged Navier–Stokes Solver in WindNinja for Operational Wildland Fire Applications." In: *Atmosphere* 10.11 (2019), p. 672.

[53] John L Walmsley and Peter A Taylor. "Boundary-layer Flow Over Topography: Impacts of the Askervein Study." In: *Boundary-Layer Meteorology 25th Anniversary Volume, 1970–1995*. Springer, 1996, pp. 291–320.

[54] D Weihs and RD Small. *Interactions and Spreading of Adjacent Large Area Fires*. Tech. rep. PACIFIC-SIERRA RESEARCH CORP LOS ANGELES CA, 1986.

[55] David R Weise and Gregory S Biging. "Effects of Wind Velocity and Slope on Flame Properties." In: *Canadian Journal of Forest Research* 26.10 (1996), pp. 1849–1858.

[56] David E Womble. "A Time-Stepping Algorithm for Parallel Computers." In: *SIAM journal on scientific and statistical computing* 11.5 (1990), pp. 824–837.

BIOGRAPHICAL SKETCH

David Robinson was born November 15, 1990 in Modesto, California. He transferred from Merced Community College (MCC) to San Francisco State University (SFSU) and received a BS in Astrophysics. After graduating from SFSU he enrolled in graduate school to pursue a PhD in Computational Science at the Scientific Computing (SC) Department at Florida State University (FSU) located in Tallahassee, Florida. Later shifted to a new joint program between the Geophysical Fluid Dynamics Institute (GFDI) and SC Departments at FSU focused on Fire Dynamics. He relocated to Los Alamos, New Mexico to pursue his doctoral research at the Earth and Environmental Sciences Division at the Los Alamos National Laboratory (LANL). He is co-advised by Rodman Linn at LANL and Bryan Quaife at FSU.